

# Transverse Momentum in Nucleons

David M. Riser

May 2019



# Contents

<b>1</b>	<b>Introduction</b>	<b>7</b>
1.1	Deeply Inelastic Scattering and Structure Functions . . . . .	7
1.2	The Parton Model and Parton Distribution Functions . . . . .	8
1.3	HERA . . . . .	8
1.4	Semi-Inclusive Deeply Inelastic Scattering . . . . .	10
1.5	Transverse Momentum Dependent Functions . . . . .	10
<b>2</b>	<b>Experiment</b>	<b>17</b>
2.1	CEBAF . . . . .	17
2.1.1	Electron Injection & Polarization . . . . .	17
2.1.2	Acceleration of Electrons . . . . .	19
2.2	CLAS in Jefferson Lab Experimental Hall B . . . . .	21
2.2.1	CLAS Torus and Drift Chambers . . . . .	22
2.2.2	CLAS Cherenkov Counter . . . . .	23
2.2.3	CLAS Time of Flight Scintillator . . . . .	23
2.2.4	CLAS Electromagnetic Calorimeter . . . . .	24
<b>3</b>	<b>Basic Analysis &amp; Corrections</b>	<b>27</b>
3.1	Introduction . . . . .	27
3.2	Luminosity Calculation . . . . .	27
3.3	Determination of Good Run List . . . . .	30
3.4	Helicity Determination . . . . .	30
3.5	Vertex Corrections . . . . .	30
3.6	Timing Corrections . . . . .	32
3.7	Kinematic Corrections . . . . .	33
<b>4</b>	<b>Particle Identification</b>	<b>39</b>
4.1	Introduction . . . . .	39

---

4.2	Electron Identification . . . . .	39
4.2.1	Electron ID Cuts . . . . .	39
4.3	Hadron Identification . . . . .	51
4.3.1	Hadron ID Cuts . . . . .	51
<b>5</b>	<b>Beam Spin Asymmetry Analysis</b>	<b>63</b>
5.1	Introduction . . . . .	63
5.2	Event Selection and Binning . . . . .	63
5.3	Measured $\phi_h$ Distributions . . . . .	67
5.4	Extraction of Modulations . . . . .	76
<b>6</b>	<b>Inclusive Cross Section</b>	<b>83</b>
6.1	Motivation . . . . .	83
6.2	Inelastic Scattering Model . . . . .	84
6.3	Analysis . . . . .	84
6.3.1	Event Selection . . . . .	84
6.3.2	Binning . . . . .	85
6.3.3	Simulation . . . . .	87
6.3.4	Radiative Corrections . . . . .	89
6.3.5	Bin Center Corrections . . . . .	89
6.3.6	Model Comparison . . . . .	95
<b>7</b>	<b>SIDIS Cross Section</b>	<b>97</b>
7.1	Introduction . . . . .	97
7.2	Hadron Identification . . . . .	98
7.3	Event Selection . . . . .	100
7.4	Binning . . . . .	100
7.5	MC Simulation . . . . .	100
7.5.1	Acceptance Corrections . . . . .	102
7.6	Radiative Corrections . . . . .	103
7.7	Parameter Estimation (Fitting) . . . . .	103
7.7.1	Minimal Coverage in $\phi_h$ for Fitting . . . . .	105
7.8	Systematic Uncertainties . . . . .	105
7.9	Results . . . . .	108
<b>References</b>		<b>117</b>

# List of Figures

1.1	A diagrammatic representation of deeply inelastic scattering . . . . .	9
1.2	$F_2(Q^2)$ results from HERA . . . . .	11
1.3	Leading order TMD table. . . . .	12
1.4	Diagrammatic representation of SIDIS with hadronic $\phi_h$ angle. . . . .	12
2.1	Diagrammatic representation of CEBAF. . . . .	18
2.2	This aerial photograph contains annotations that show the accelerator path and the three experimental halls. . . . .	20
2.3	In this diagrammatic representation of CLAS, several important detector sub-systems are labeled. . . . .	21
2.4	Diagrams of the CLAS torus field. This figure reproduced from [? ] . . . . .	22
2.5	Illustration of a charged particle interacting with cells in the drift chamber. This figure was reproduced from [? ] . . . . .	23
2.6	The CLAS Cherenkov Counter. . . . .	24
2.7	The U, V, W structure of CLAS electromagnetic calorimeter is shown above. . . . .	25
2.8	GEANT simulation of an electron showering in the EC. This figure originally appeared in [? ] . . . . .	26
3.1	Entries per scalar reading for run 38222. . . . .	29
3.2	Charge per scalar reading for run 38222. . . . .	29
3.3	Inclusive electrons per file normalized by the total charge accumulated for the file. This quantity is used to make a good run list. . . . .	31
3.4	The waveplate position is determined and corrected by plotting the BSA for $\pi^+$ mesons as a function of the run. The top panel shows the corrected results, the bottom shows the results before changing the helicity. . . . .	31

3.5 The z-vertex $v_z$ position shown for different values of $\phi$ the azimuthal angle in the hall. The left figure shows the distribution before corrections are applied, the right after. The vertical red lines bound the region which we define as acceptable for electrons in our analysis. . . . .	32
3.6 Timing corrections are shown for paddle 24 of sector 1. The left image shows the $\Delta\beta$ distribution before corrections. On the right the same is shown after correction of the timing for this paddle. We assume the mass of the track to be the pion, these show up as the green band. Heavier protons are visible below the pion band. . . . .	33
3.7 This figure shows the deviation from $M_p$ of the $W$ spectrum peak for elastic $ep \rightarrow ep$ events (before corrections). . . . .	35
3.8 This figure shows the deviation from $M_p$ of the $W$ spectrum peak for elastic $ep \rightarrow ep$ events (after $\phi$ -dependent corrections). . . . .	36
3.9 Elastic events shown in the spectrum of $W$ before and after momentum corrections are applied. . . . .	37
 4.1 Tracks shown in color remain after the application of drift chamber region 1 fiducial cuts to all cuts, shown here as black points. . . . .	42
4.2 The selection criteria shown in red is applied to drift chamber region 3. . . . .	43
4.3 All negative tracks are shown here in black. In color, the tracks which pass the EC fiducial cut are shown. . . . .	44
4.4 Each panel shown above contains events from one sector, increasing from 1-6 from top left to bottom right. The value selected of 60 MeV is applied to all sectors and separates the negatively charged pions (left) from the electrons (right). . . . .	45
4.5 The sampling fraction selection boundary is shown here for the nominal value of $N_{sigma} = 4$ . . . . .	47
4.6 The track vertex cut is shown above. All negative tracks are shown in white, while the tracks passing all other criteria are shown in black hatch. The cut boundary is displayed as red lines. For E1-F the target center was located at -25 cm. . . . .	48
4.7 The angle $\phi_{rel}$ is the azimuthal angle between the central line of the detector and the track. .	49
4.8 Correlation between $\theta_{CC}$ and the CC segment is shown above, with our selection boundaries overlaid in red. . . . .	50
4.9 Shown above: Positive track hits on the region 1 drift chamber, events falling between the red lines are kept for analysis. . . . .	52
4.10 Shown above: The difference between the z-vertex position between detected electrons and positive tracks. . . . .	53

4.11	Shown above: The distribution of confidence level for all positive tracks after being classified by the likelihood ratio. . . . .	54
4.12	Shown above: All positive tracks overlaid with our determination of $\mu(p) \pm \sigma(p)$ for $\pi^+$ . .	55
4.13	Shown above: All positive tracks overlaid with our determination of $\mu(p) \pm \sigma(p)$ for $K^+$ . .	56
4.14	Shown above: All positive tracks overlaid with our determination of $\mu(p) \pm \sigma(p)$ for $p^+$ . .	56
4.15	Positive hadrons from the Monte Carlo simulation produce a $\beta$ vs. $p$ simulation that is very similar to data. . . . .	60
4.16	The efficiency and purity of our kaon sample are studied by using a Monte Carlo simulation. Here, the results are studied as a function of the confidence level, and of the track momentum. . . . .	60
5.1	Correlation between $z$ and $P_T^2$ ( $GeV^2/c^2$ ) for each event in our analysis sample. . . . .	64
5.2	The missing mass spectrum for the reaction $ep \rightarrow e'K^+X$ is shown after the application of all cuts used in the analyses except for the cut we apply on the missing mass. . . . .	65
5.3	Bins used for this analysis are displayed in two dimensions for the $z$ axis. . . . .	66
5.4	The analysis is run for variations in the input parameters $\theta_i$ to calculate the dependence of the result $\mathcal{O}$ on each parameter, as described in this section. . . . .	69
5.5	Boundaries and associated uncertainties for the $EC$ coordinate cuts. . . . .	71
5.6	The magnitude of each systematic error source considered is shown above in a heat-map for the $x$ axis. The vertical scale maximum corresponds to half of a percent. . . . .	72
5.7	The magnitude of each systematic error source considered is shown above in a heat-map for the $P_T$ axis. The vertical scale maximum corresponds to half of a percent. . . . .	73
5.8	The magnitude of each systematic error source considered is shown above in a heat-map for the $z$ axis. The vertical scale maximum corresponds to half of a percent. . . . .	74
5.9	The relative contribution of each systematic uncertainty to the total is shown above averaged over the bins of the $x$ axis. . . . .	75
5.10	The relative contribution of each systematic uncertainty to the total is shown above averaged over the bins of the $z$ axis. . . . .	76
5.11	Counts for different helicity states are superimposed for different bins of $z$ . . . . .	79
5.12	Our extraction of $A_{LU}^{\sin\phi}$ for the kinematic bins described above. The black error bars represent uncertainty in the extraction of the parameter value. Red error bars are systematic uncertainties. . . . .	80
5.13	In this figure the results of this study for positively charged kaons are compared with previous results from the same dataset produced by [? ] for positively charged pions. This figure shows the $x$ and $Q^2$ dependence of $A_{LU}^{\sin\phi_h}$ . . . . .	80

---

5.14 In this figure the results of this study for positively charged kaons are compared with previous results from the same dataset produced by [? ] for positively charged pions. This figure shows the $z$ and $P_T$ dependence of $A_{LU}^{\sin \phi_h}$ . . . . .	81
6.1 Inclusive data and simulation comparison. . . . .	85
6.2 Event distributions ( $\theta_e$ vs $p$ ) for data, simulated inelastic events, and simulated elastic events with radiation are shown. The red line indicates the momentum cut applied by restricting $y < 0.7$ . The band of events on the right side of the figure contains all un- radiated elastic events. The larger portion of events present on the left side are Bethe- Heitler events which we wish to avoid in our analysis. . . . .	86
6.3 Reconstructed Monte Carlo events displayed for different sectors (by panel) and different $Q^2$ bins represented by different colors. . . . .	90
6.4 Generated Monte Carlo events displayed for different sectors (by panel) and different $Q^2$ bins represented by different colors. These events were generated with radiative effects. .	91
6.5 Reconstructed events from data (black) and Monte Carlo (red) are superimposed to show that the simulation is a good approximation to the physics, a fact important for the accurate calculation of acceptance. . . . .	92
6.6 Acceptance corrections applied to the inclusive cross section are shown above in sixty panels that correspond to increasing $Q^2$ from left to right, and increasing sector number from top to bottom. . . . .	93
6.7 Radiative corrections applied to the inclusive cross section are shown above in sixty panels that correspond to increasing $Q^2$ from left to right, and increasing sector number from top to bottom. . . . .	94
6.8 The bin center correction applied to the inclusive cross section is shown for different values of $Q^2$ (indicated by color) as a function of $W$ on the horizontal axis. This correction is the same for all sectors. . . . .	95
6.9 Each panel above shows one of the six sectors of CLAS, the horizontal axis shows $W$ and superimposed on the figure are the cross sections for different bins of $Q^2$ . For simplicity of the visualization each reported value of $Q^2$ is the bin center. . . . .	96
7.1 PID for $\pi^+$ used for the SIDIS analysis . . . . .	99
7.2 Kinematic distributions and binning for electron variables. . . . .	101
7.3 Kinematic distributions and binning for hadron variables. . . . .	102
7.4 Acceptance corrections for SIDIS . . . . .	104
7.5 Radiative corrections for $\pi^+$ . . . . .	105
7.6 Corrected yield fits for $\pi^+$ . . . . .	106

7.7	Corrected yield fits for $\pi^-$	107
7.8	Systematic boundaries on region 1	109
7.9	Systematic boundaries on region 3	110
7.10	Systematic boundaries on sampling fraction	111
7.11	Systematic variations of electron z-vertex cuts.	112
7.12	Systematic variations of the CC fiducial cut for electrons.	112
7.13	Variation of EC U, V, and W cuts used to identify electrons.	113
7.14	$d^5\sigma$ for $\pi^+$	114



# Chapter 1

## Introduction

Research into the internal structure of protons and neutrons began in 1955 with the pioneering work of Hofstadter and McAllister. Working together at Standford, the pair measured the electron-proton scattering cross section with 188 MeV electrons that were incident on a hydrogen target. Their analysis demonstrated that at large angles the measured cross section was inconsistent with the cross section predicted for a point-like proton. Simultaneously, the Brookhaven Cosmotron produced an overwhelming number of new particles, creating what was dubbed a "particle zoo". Theoretical efforts by Gell-Mann and Zweig produced a system of categorizing the particles by their charge and strangeness, and eventually the basis for constructing these in terms of a new type of fractionally charged particle that Gell-Mann coined the quark.

### 1.1 Deeply Inelastic Scattering and Structure Functions

In contrast to elastic scattering, when kinetic energy of the scattered electron is not conserved the reaction is called inelastic scattering. As the incident energy of electrons in scattering experiments grows larger than the proton mass, the inelastic scattering cross section begins to become dominant. In a deeply inelastic scattering (DIS) event, an electron collides with the target particle and transfer sufficient energy to interrogate it on a distance scale much smaller than its radius, and is then detected. The DIS cross section can be decomposed in terms of two structure functions  $F_1$  and  $F_2$ .

$$\frac{d^2\sigma}{dxdQ^2} = \frac{4\pi\alpha^2}{Q^4} \left\{ \left( 1 - y - \frac{m_p^2 y^2}{Q^2} \right) \frac{F_2(x, Q^2)}{x} + y^2 F_1(x, Q^2) \right\} \quad (1.1)$$

The electron kinematics are described by the four momentum transfer  $q^\mu = k^\mu - k'^\mu$ , the negative

momentum transfer  $Q^2 = -q^\mu q_\mu$  and,

$$x = \frac{Q^2}{2P \cdot q} \quad y = \frac{P \cdot q}{P \cdot l} \quad (1.2)$$

where  $x$  is called the momentum fraction and  $y$  is the inelasticity. The variable  $x$  (which will appear throughout this thesis) is bounded between zero and one and describes the fraction of the total proton momentum carried by the quark struck in the scattering. For the case that  $Q^2 \gg m_p^2 y^2$  the cross section reduces further.

$$\frac{d^2\sigma}{dx dQ^2} \approx \frac{4\pi\alpha^2}{Q^4} \left\{ (1-y) \frac{F_2(x, Q^2)}{x} + y^2 F_1(x, Q^2) \right\} \quad (1.3)$$

## 1.2 The Parton Model and Parton Distribution Functions

Feynman's "parton model" (1969) stated that during high energy electron-proton collisions the electron enters with so much energy that the quarks which compose the proton are essentially stationary, and the electron simply scatters off of one part (quark or gluon) of the nucleus. This "parton" model assumed that the cross section for electron-proton scattering was the product of an elastic scattering between a charged electron and quark (calculable using techniques from quantum electrodynamics), and a function that describes the momentum of the quark in the proton prior to the collision, called the parton distribution function (PDF). Parton distribution functions are indexed with the variable  $x$  that represents the fractional proton momentum carried by the struck quark.

$$\frac{d^2\sigma}{dx dQ^2} = \frac{4\pi\alpha^2}{Q^4} \left\{ 1 - y + \frac{y^2}{2} \right\} \sum_i Q_i^2 q_i^p(x) \quad (1.4)$$

In the equation above  $q_i^p(x)$  is the proton PDF for quark flavor  $i$ . When equating 1.3 with 1.4 Bjorken scaling for  $ep$  DIS falls out.

$$F_2(x, Q^2) = 2xF_1(x, Q^2) = x \sum_i Q_i^2 q_i^p(x) \quad (1.5)$$

## 1.3 HERA

The HERA electron-proton collider, which operated from 1991-2007 at DESY studied DIS extensively at large  $Q^2 > 200 \text{ GeV}^2$  and small  $x < 0.0001$  by colliding 27.5 GeV electrons and 820/920 GeV protons. The H1 and ZEUS experiments at HERA mapped out the proton structure functions in great detail. The results (shown in figure) display a weak dependence on  $Q^2$ ; a feature which can be calculated using the DGLAP evolution equations, providing more support for the simple partonic picture. The PDFs

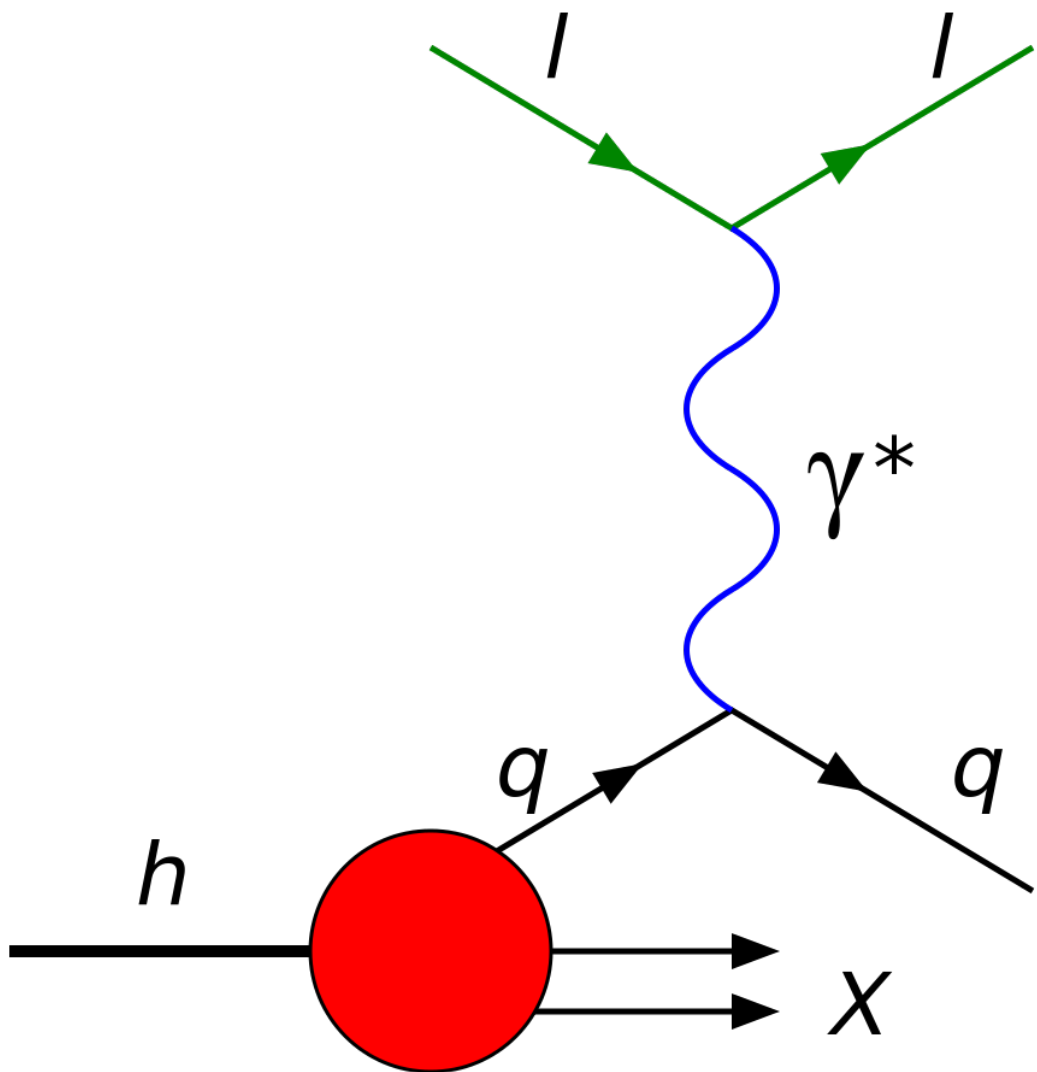


Figure 1.1: Deeply inelastic scattering (DIS) between a lepton and a hadron, in this thesis an electron and a proton.

extracted from these structure functions show that almost half of the proton momentum is carried by gluons (and quark/anti-quark pairs created by their splitting).

## 1.4 Semi-Inclusive Deeply Inelastic Scattering

In 1996 it was realized by Mulders that by detecting a hadron in the final state of an electron-proton deeply inelastic scattering event (a reaction known as semi-inclusive deeply inelastic scattering), one could learn about the quark momentum in the plane transverse to the hard scattering direction along which the momentum fraction  $x$  is defined. In an analogous manner to the DIS electron-proton cross section, the cross section for SIDIS can be decomposed into a set of 18 structure functions (depending on the polarization direction of the electron and proton).

## 1.5 Transverse Momentum Dependent Functions

In analogue with the simple co-linear case, parton model-like assumptions are made about the nature of the scattering and all 18 of these structure functions can be calculated in terms of TMD PDFs and TMD Fragmentation Functions (TMD FFs). The new assumption, known as factorization, is at the core of the applicability of the TMD interpretation to results of SIDIS (and other types such as Drell-Yan scattering) experiments. The hadronic matrix element that describes the transition from proton to all possible final states is decomposed using the operator product expansion (OPE) and factorization has been proven for the SIDIS process at leading order in the expansion (twist two) [reference here].

What results from this expansion is the set of non-perturbative TMD PDF and TMD FF functions, at twist two in the expansion there are 9 such functions, at twist three there are 16. By comparing kinematic dependence, these functions can be associated with structure functions in the cross section decomposition.

In this thesis I present two distinct measurements of SIDIS structure functions and their combinations. The first observable measured is the unpolarized cross section, which is presented as an extension of the analysis of Nathan Harrison who measured the unnormalized cross sections for charged pions in CLAS [reference to Nate]. Three structure functions appear in this cross section expansion, those which have the unpolarized beam and target subscripts "UU" in the cross section equation. The leading structure function is not modulated by the phi dependent angle of the outgoing hadron, and is expected to be dominant in size when compared with the two co-sinusoidal structure functions that remain. This novel measurement compliments the unnormalized work of Nathan Harrison as well as the measurements of multiplicities performed by the HERMES and COMPASS collaborations [reference both of those]. Without applying the TMD framework, this measurement still has value in that it provides the

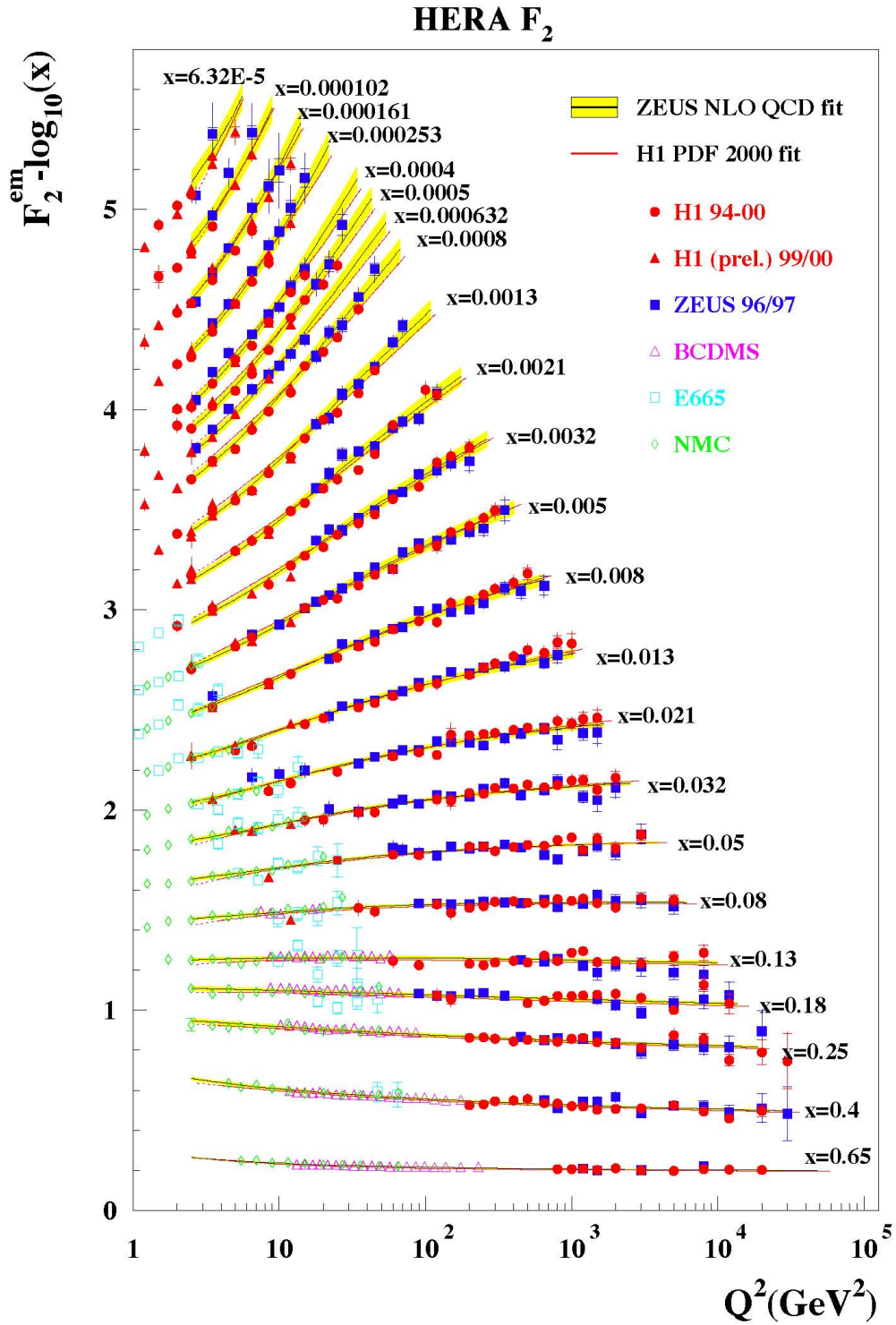


Figure 1.2: HERA experiments ZEUS and H1 mapped out the structure function  $F_2$ , which displayed the predicted Bjorken scaling for most values of  $x$ . The mild  $Q^2$  dependence of the PDFs can be calculated using the DGLAP evolution equations for the PDFs, providing an understanding for the observed dependence.

## “Leading-Twist” TMD Quark Distributions

Nucleon Quark	Unpol.	Long.	Trans.
Unpol.	$f_1 = \bullet$		$f_{1T}^\perp = \bullet \uparrow - \bullet \downarrow$
Long		$g_{1L} = \bullet \rightarrow - \bullet \rightarrow$	$g_{1T} = \bullet \uparrow - \bullet \uparrow$
Trans.	$h_1^\perp = \bullet \uparrow - \bullet \downarrow$	$h_{1L}^\perp = \bullet \rightarrow - \bullet \rightarrow$	$h_{1T}^\perp = \bullet \uparrow - \bullet \uparrow$ $h_{1T}^\parallel = \bullet \uparrow - \bullet \uparrow$

Figure 1.3: The twist two TMDs are tabulated in terms of their spin decomposition.

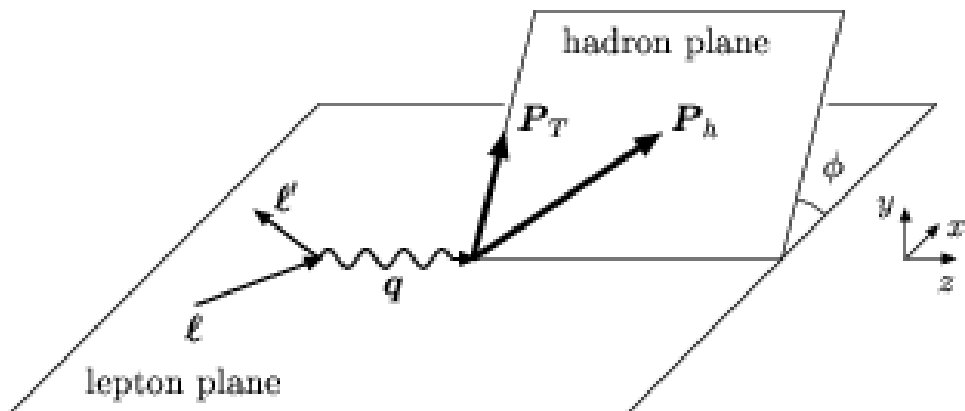


Figure 1.4: In a SIDIS event the scattered electron is detected as well as one final state hadron, allowing for the calculation of the angle  $\phi_h$  which appears frequently in the SIDIS cross section.

scale of the structure functions for the first time and can be used to predict SIDIS yields for future studies. Within the TMD framework, the leading order unpolarized structure function is composed of the unpolarized PDF and the unpolarized fragmentation function, both fairly well known from previous experiments. The phi modulated structure functions contain a TMD PDF known as the Boer-Mulders function, pursued for its possible connection to quark orbital angular momentum. I expect that the results of this measurement can be used as input, with results from other experiments, to extract the Boer-Mulders TMD using a phenomenological model.

I also present measurements of positively charged kaon beam spin asymmetries, which addresses several interesting areas of TMD physics. The beam spin asymmetry, defined as the difference in events observed for different electron helicity states (normalized by the total number of electrons), depends on the observable structure function ( $F_L U \sin \Phi$ ). Interestingly, if one assumes that twist three PDFs and FFs are zero, the beam spin asymmetry term vanishes because the structure function in question is composed of pure twist three products of PDFs and FFs.

Recently CLAS reported the non-zero BSA measurement of charged and neutral pion beam spin asymmetries, which implies that in the kinematics measured by CLAS, the twist three TMD terms cannot be neglected [reference to Wes Gohn thesis]. As a natural extension of this knowledge, I analyze the same observable for the heavier kaon channel to see if the same conclusion is realized.

I have reviewed the experimental hardware that enables this thesis work in chapter 2 and summarized analytical techniques used during chapter 3. I describe basic analysis procedures that are common to both measurements in chapter 4 before discussing particle identification in chapter 5. I present results for the inclusive scattering cross section in chapter 6, followed by the SIDIS cross section in chapter 7. I then present my findings for the positively charged kaon BSA measurement in chapter 8 before offering a brief summary and outlook in chapter 9.

$$e(l) + h(P) \rightarrow e'(l') + h(P_h) + X \quad (1.6)$$

In SIDIS it is customary to define the following kinematic variables (where  $q = l - l'$  and  $Q^2 = -q^2$ ).

$$x = \frac{Q^2}{2P \cdot q} \quad y = \frac{P \cdot q}{P \cdot l} \quad z = \frac{P \cdot P_h}{P \cdot q} \quad \gamma = \frac{2Mx}{Q} \quad (1.7)$$

Additionally, the ratio  $\varepsilon$  of the longitudinal and transverse photon flux is shown below.

$$\varepsilon = \frac{1 - y - \frac{1}{4}\gamma^2 y^2}{1 - y + \frac{1}{2}y^2 + \frac{1}{4}\gamma^2 y^2} \quad (1.8)$$

$$\begin{aligned}
\frac{d\sigma^{e^- P \rightarrow e^- hX}}{dx_B dy d\phi_s dz d\phi_h dp_{h\perp}^2} &= \frac{\alpha_{em}^2}{2x_B y Q^2} \frac{y^2}{1-\varepsilon} \left(1 + \frac{\gamma^2}{2x_B}\right) \Big\{ \\
&\quad F_{UU,T} + \varepsilon F_{UU,L} + \sqrt{2\varepsilon(1+\varepsilon)} \cos \phi_h F_{UU}^{\cos \phi_h} + \varepsilon \cos(2\phi_h) F_{UU}^{\cos 2\phi_h} \\
&+ \lambda_e \sqrt{2\varepsilon(1-\varepsilon)} \sin \phi_h F_{LU}^{\sin \phi_h} + \lambda \left[ \sqrt{2\varepsilon(1+\varepsilon)} \sin \phi_h F_{UL}^{\sin \phi_h} + \varepsilon \sin(2\phi_h) F_{UL}^{\sin 2\phi_h} \right] \\
&+ \lambda_e \lambda \left[ \sqrt{1-\varepsilon^2} F_{LL} + \sqrt{2\varepsilon(1-\varepsilon)} \cos \phi_h F_{LL}^{\cos \phi_h} \right] \\
&+ s_\perp \left[ \sin(\phi_h - \phi_S) (F_{UT,T}^{\sin(\phi_h - \phi_S)} + \varepsilon F_{UT,L}^{\sin(\phi_h - \phi_S)}) \right. \\
&\quad \left. + \varepsilon \sin(\phi_h + \phi_S) F_{UT}^{\sin(\phi_h + \phi_S)} + \varepsilon \sin(3\phi_h - \phi_S) F_{UT}^{\sin(3\phi_h - \phi_S)} \right. \\
&\quad \left. + \sqrt{2\varepsilon(1+\varepsilon)} \sin \phi_S F_{UT}^{\sin \phi_S} + \sqrt{2\varepsilon(1+\varepsilon)} \sin(2\phi_h - \phi_S) F_{UT}^{\sin(2\phi_h - \phi_S)} \right] \\
&+ \lambda_e s_\perp \left[ \sqrt{1-\varepsilon^2} \cos(\phi_h - \phi_S) F_{LT}^{\cos(\phi_h - \phi_S)} + \sqrt{2\varepsilon(1-\varepsilon)} \cos \phi_S F_{LT}^{\cos \phi_S} \right. \\
&\quad \left. + \sqrt{2\varepsilon(1-\varepsilon)} \cos(2\phi_h - \phi_S) F_{LT}^{\cos(2\phi_h - \phi_S)} \right] \Big\}, \tag{1.9}
\end{aligned}$$

Here  $\lambda_e$  refers to the helicity of the incoming lepton (beam electron in our case). If one decomposes the hadronic matrix element which is present in the hadronic tensor into different possible Dirac structures, a set of functions known as transverse momentum dependent parton distributions functions (TMD PDFs) and transverse momentum dependent fragmentation functions (TMD FFs) can be defined. The structure functions from above can then be calculated as a convolution of these more basic non-perturbative functions. The notation  $\mathcal{C}$  is shorthand presented in [? ] as a way to write structure functions in terms of the convolutions of PDF and FF objects.

$$\mathcal{C}[\omega f D] = x \sum_a e_a^2 \int d^2 \mathbf{p}_T d^2 \mathbf{k}_T \delta^{(2)}(z \mathbf{k}_T + \mathbf{p}_T - \mathbf{P}_{h\perp}) \omega(\mathbf{k}_T, \mathbf{p}_T) f^a(x, k_T^2) D^a(z, p_T^2) \tag{1.10}$$

where  $a$  is summed over quarks and anti-quarks. The five structure functions appearing in the cross section are,

$$F_{UU,T} = \mathcal{C}[f_1 D_1] = x \sum_a e_a^2 \int d^2 \mathbf{p}_T d^2 \mathbf{k}_T \delta^{(2)}(z \mathbf{k}_T + \mathbf{p}_T - \mathbf{P}_{h\perp}) f_1^a(x, k_T^2) D_1^a(z, p_T^2) \tag{1.11}$$

$$F_{UU,L} = 0 \tag{1.12}$$

$$F_{UU}^{\cos \phi_h} = \frac{2M}{Q} \mathcal{C} \left[ -\frac{\hat{\mathbf{h}} \cdot \mathbf{k}_T}{M_h} \left( x h H_1^\perp + \frac{M_h}{M} f_1 \frac{\tilde{D}^\perp}{z} \right) - \frac{\hat{\mathbf{h}} \cdot \mathbf{p}_T}{M} \left( x f^\perp D_1 + \frac{M_h}{M} h_1^\perp \frac{\tilde{H}}{z} \right) \right] \tag{1.13}$$

$$F_{UU}^{\cos 2\phi_h} = \mathcal{C} \left[ -\frac{2(\hat{\mathbf{h}} \cdot \mathbf{k}_T)(\hat{\mathbf{h}} \cdot \mathbf{p}_T) - \mathbf{k}_T \cdot \mathbf{p}_T}{MM_h} h_1^\perp H_1^\perp \right] \quad (1.14)$$

$$F_{LU}^{\sin \phi} = \frac{2M}{Q} \mathcal{C} \left[ -\frac{\hat{\mathbf{h}} \cdot \mathbf{k}_T}{M_h} \left( xeH_1^\perp + \frac{M_h}{M} f_1 \frac{\tilde{G}^\perp}{z} \right) + \frac{\hat{\mathbf{h}} \cdot \mathbf{p}_T}{M} \left( xg^\perp D_1 + \frac{M_h}{M} h_1^\perp \frac{\tilde{E}}{z} \right) \right] \quad (1.15)$$

$$BSA = \frac{d\sigma^+ - d\sigma^-}{d\sigma^+ + d\sigma^-} = \frac{A_{LU}^{\sin \phi} \sin \phi}{1 + A_{UU}^{\cos \phi} \cos \phi + A_{UU}^{\cos(2\phi)} \cos(2\phi)} \quad (1.16)$$

Where the coefficient  $A_{LU}^{\sin \phi}$  is defined as,

$$A_{LU}^{\sin \phi} = \sqrt{2\varepsilon(1-\varepsilon)} \frac{F_{LU}^{\sin \phi}}{F_{UU,T} + \varepsilon F_{UU,L}} \quad (1.17)$$



# Chapter 2

## Experiment

Jefferson National Lab houses the continuous electron beam accelerator facility (CEBAF) which is currently capable of providing 11 GeV electron beams to three experimental end stations, and 12 GeV to a fourth. The data that are analyzed in this study are from the run period E1-F, which occurred before the 12 GeV CEBAF upgrade, the details in this chapter describe the accelerator and CLAS detector at the time of the E1-F run period.

### 2.1 CEBAF

Proposed in 1982 and constructed between 1987-1997 the CEBAF accelerator at Jefferson lab was composed of a pair of linear accelerators and 9 recirculating arcs arranged in a racetrack shape [? ? ]. Originally designed to provide 4 GeV unpolarized electrons to three experimental halls, CEBAF was fitted with twin polarized electron guns, and upgraded to 6 GeV beam energy before the E1-F run period. CEBAF was built to provide an extremely high duty factor and an average beam current of up to 200  $\mu A$ .

#### 2.1.1 Electron Injection & Polarization

CEBAF's injector provided 45 MeV electrons with 70%-80% longitudinal polarization for the main accelerator. In order to provide an apparent continuous stream of events to the detectors, electron bunches were produced at a rate of  $f = 1497 \text{ Mhz}$ . To accommodate different requests for energy and beam current simultaneously, the injector produced three interspersed bunch trains at a frequency of 499  $\text{Mhz}$ . The output injector energy  $E = 45 \text{ MeV}$  was chosen so that injected electrons were *sufficiently relativistic*. In other words, when bunches of electrons at different energies simultaneously passed through the

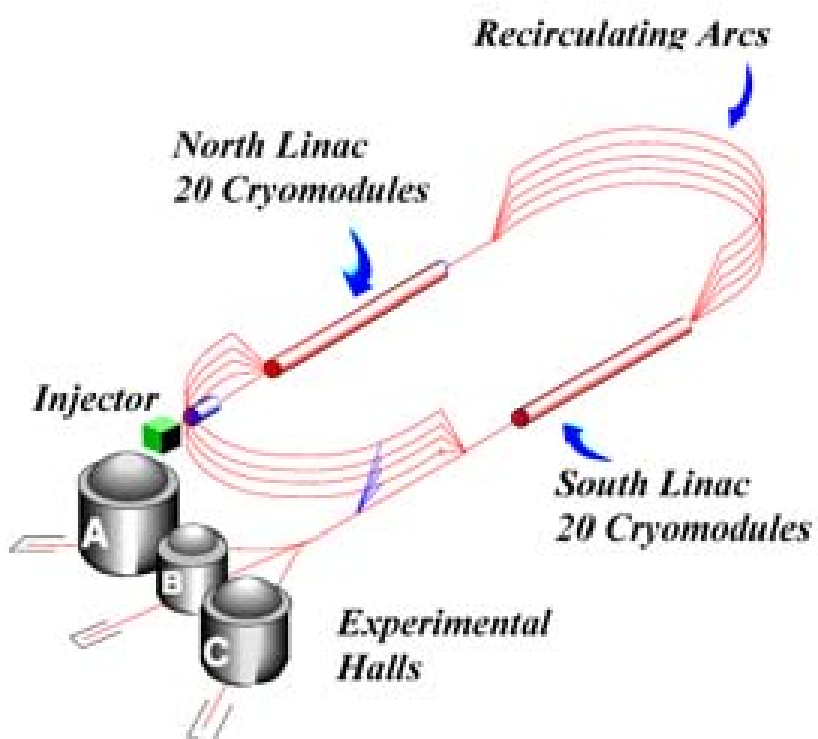


Figure 1: Layout of CEBAF.

Figure 2.1: Diagrammatic representation of CEBAF.

linear accelerators (LINACs), the relative phase difference (between different energy passes) accumulated over the distance remained less than  $1^\circ$ .

During early accelerator construction, the need for polarized electrons became apparent and the final polarized electron gun was produced in 2000. Production of polarized electrons was achieved by using twin polarized electron guns mounted at  $15^\circ$  with respect to the injector beam axis. Inside of each gun, electrons were liberated from gallium arsenide photo-cathodes by three independent diode lasers operated at a repetition rate of  $499\text{ Mhz}$ . During polarized production, the diodes operated at a central wavelength of  $850\text{ nm}$ . By manipulating the laser polarization using a Pockels cell, the electron beam spin is flipped at a rate of  $60\text{ Hz}$ . Throughout the run period, an overall phase difference could be introduced by rotation of a wave-plate. As will be discussed in some detail later, changes in beam helicity due to wave-plate settings must be removed from the recorded data. After acceleration to  $5\text{ MeV}$  the beam polarization was measured in the injector facility using a Mott polarimeter.

### 2.1.2 Acceleration of Electrons

The north and south LINACs were responsible for increasing the energy of the electrons from  $45\text{ MeV}$  up to an impressive  $\approx 5.7\text{ GeV}$  before delivery to the experimental halls A, B, and C. In order to achieve this each bunch of electrons was accelerated through ten stages, five passes through each LINAC. The strong electric field needed to accelerate electron bunches was confined inside of superconducting 5-cell elliptical cavities. These cavities were machined from niobium, and operated at a temperature of  $2.2^\circ\text{ K}$ . Developed at Cornell University, the cavities were operated at  $1,500\text{ Mhz}$  with a gradient greater than  $5\text{ MV/m}$  and a quality factor  $Q_0 \geq 3 \cdot 10^9$  (the Q factor describes the monochromaticity of the cavity and is defined  $Q_0 = f_0/\Delta f$ ). Each cavity was sealed inside of a cryo-unit, four such units were connected together to form an 8.5 meter cryo-module. Each LINAC was composed of 20 such cryo-modules connected together to increase electron energies by more than  $500\text{ MeV}$  per pass.

The radio frequency (RF) that powers each cavity was sourced by a water-cooled 5 kilowatt Klystron located in groups of eight above each cryo-module. Phase locking of each cavity with a master oscillator ensured that the difference in phase between all cavities was less than one degree. The important super conductivity was maintained by circulation of liquid helium at  $2.2^\circ\text{ K}$ . Production of liquid helium occurred on-site at the 5 kW helium liquefaction plant.

After re-circulation of five passes through each LINAC, full energy beams were delivered to the halls. Bunches were separated using an RF separator before entering their respective experimental



Figure 2.2: This aerial photograph contains annotations that show the accelerator path and the three experimental halls.

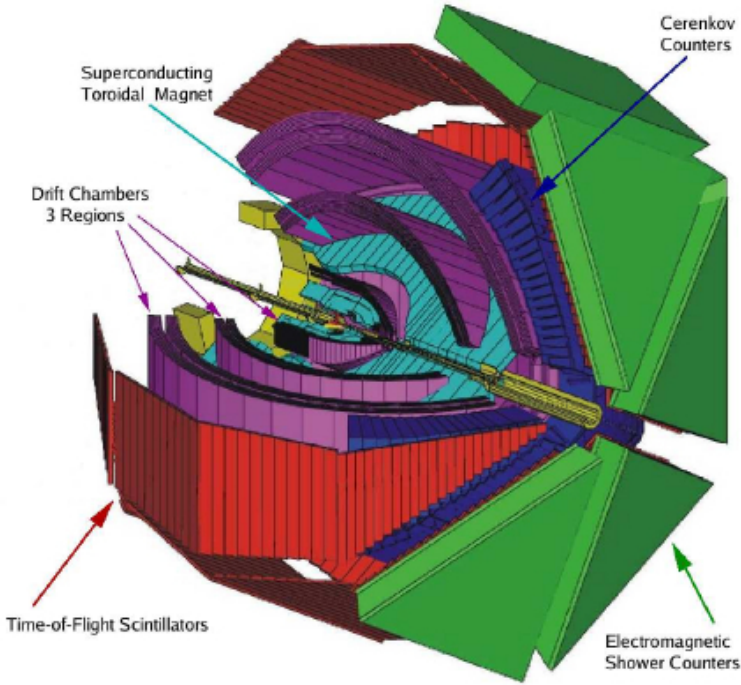


Figure 2.3: In this diagrammatic representation of CLAS, several important detector sub-systems are labeled.

halls. The beamline leading to the halls was also equipped with the ability to separate bunches before they completed five full passes delivering either three full energy beams, two full energy beams and one lower, or one full energy beam and two of lower energy. This capability, combined with the flexible beam polarization and beam current provided by the injector ensured that each hall could experiment at its desired settings simultaneously.

## 2.2 CLAS in Jefferson Lab Experimental Hall B

The CEBAF large acceptance spectrometer (CLAS), housed in Jefferson lab's Hall B, was used to record the E1-F dataset that is used in this study. Capable of detecting particles over a very large angular range, the CLAS detector covered almost the full  $4\pi$  solid angle around the target region. The detector was also designed to perform efficiently for particles with wide range of momenta between 0.5-6.0 GeV. Overall detector design consisted of a large superconducting magnet that produced a toroidal field (this magnet was referred to as the torus), and six ideally identical *sectors*. Each sector of CLAS contained an identical set of sub-systems. After combining information from all sub-systems and running the reconstruction algorithm, complete events are measured. This capability made CLAS unique in comparison with the arm style spectrometers of halls A and C. The major components of CLAS are listed below.

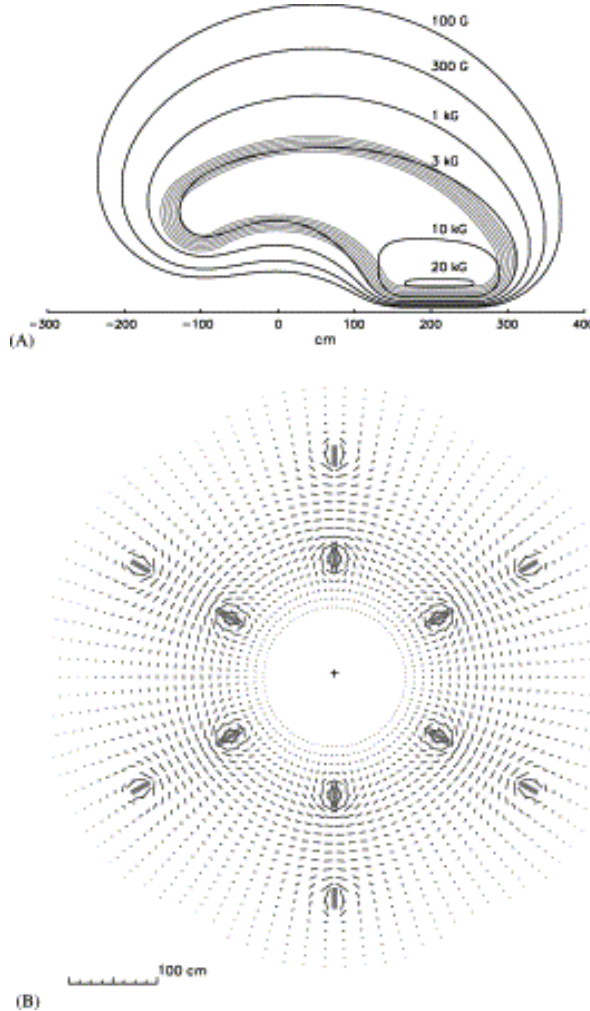


Figure 2.4: Diagrams of the CLAS torus field. This figure reproduced from [? ]

### 2.2.1 CLAS Torus and Drift Chambers

Measuring the momentum of charged particles with  $p > 200 \text{ MeV}/c$  was accomplished by measuring the curvature of the particle trajectory as it passed through the CLAS toroidal magnetic field. Six superconducting coils were arranged  $60^\circ$  apart azimuthally around the beamline to create a 2 Tesla. The field produced, which varied from two tesla at lower angles to half a tesla at angles greater than  $90^\circ$ , curved charged particle trajectories in the  $\theta$  direction without altering the azimuthal  $\phi$  direction. The geometry of the torus magnet guided the development of the entire spectrometer.

Spatially, the 18 drift chambers were divided with six in each sector. In order to perform tracking before, inside, and after the torus three radially distinct drift chambers were constructed for each sector (these were called regions 1, 2, and 3). Each drift chamber consisted of 12 superlayers of hexagonal drift chamber cells. Angular measurements in the azimuthal direction were accomplished by offsetting the first six and last six superlayers by  $6^\circ$ . In total 35,148 individual drift chambers cells were used for tracking [? ].

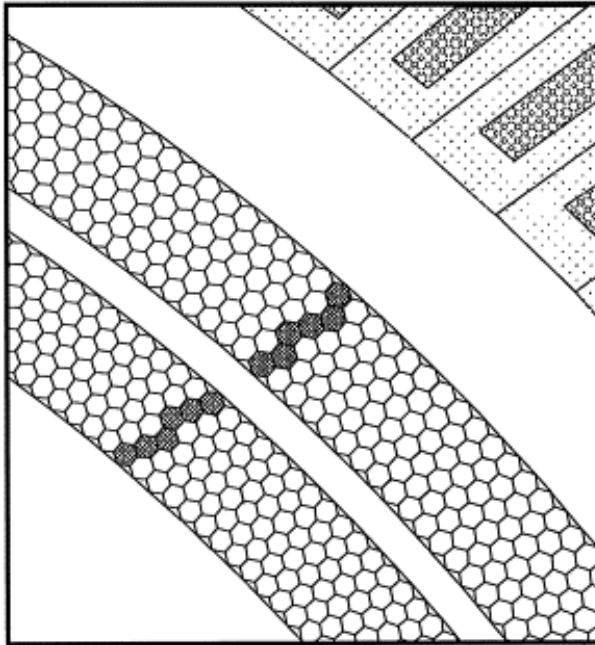


Figure 2.5: Illustration of a charged particle interacting with cells in the drift chamber. This figure was reproduced from [? ]

## 2.2.2 CLAS Cherenkov Counter

The Cherenkov counters (CC), located radially outside of the region 3 drift chambers, greatly assisted in the separation of electrons and negatively charged pions for tracks with momentum less than the pion momentum threshold  $p < p_\pi \approx 2.5 \text{ GeV}/c$  [? ]. The CLAS CCs were divided into 6 sectors, like most other detectors. Each sector was divided into 18 segments in the polar angle  $\theta$  away from the beamline. Furthermore, these segments were divided in half azimuthally to produce 12 half-sectors. Three mirrors, a light collecting Winston cone, a magnetic shield, and a 5 inch quartz face PMT were fitted to each of the 18 segments in all 12 half-sectors. During operation each CC was filled with  $6 \text{ m}^3$  of  $C_4F_{10}$  gas. The number of photo-electrons produced was recorded for tracks with polar angles between  $8^\circ < \theta < 45^\circ$ .

## 2.2.3 CLAS Time of Flight Scintillator

Measurements of average velocity can be made by simply knowing the distance some object has traveled in a given time period. Operating on this principle the CLAS time of flight (TOF) system allowed for the separation of  $\pi$  and  $K$  for momentum  $p \leq 2 \text{ GeV}/c$ . Constructed of 57 scintillating bars per sector, the TOF system covered an impressive area of  $206 \text{ m}^2$  and spanned the range of polar angles  $8^\circ \leq \theta \leq 142^\circ$ . Each of the scintillating bars measured 5.08 centimeters in thickness, 15 or 22 centimeters in width, and measured between 32 and 450 centimeters in length. Shorter bars, which covered the relatively higher rate low scattering angle, were built with an intrinsic timing resolution of 80 picoseconds.

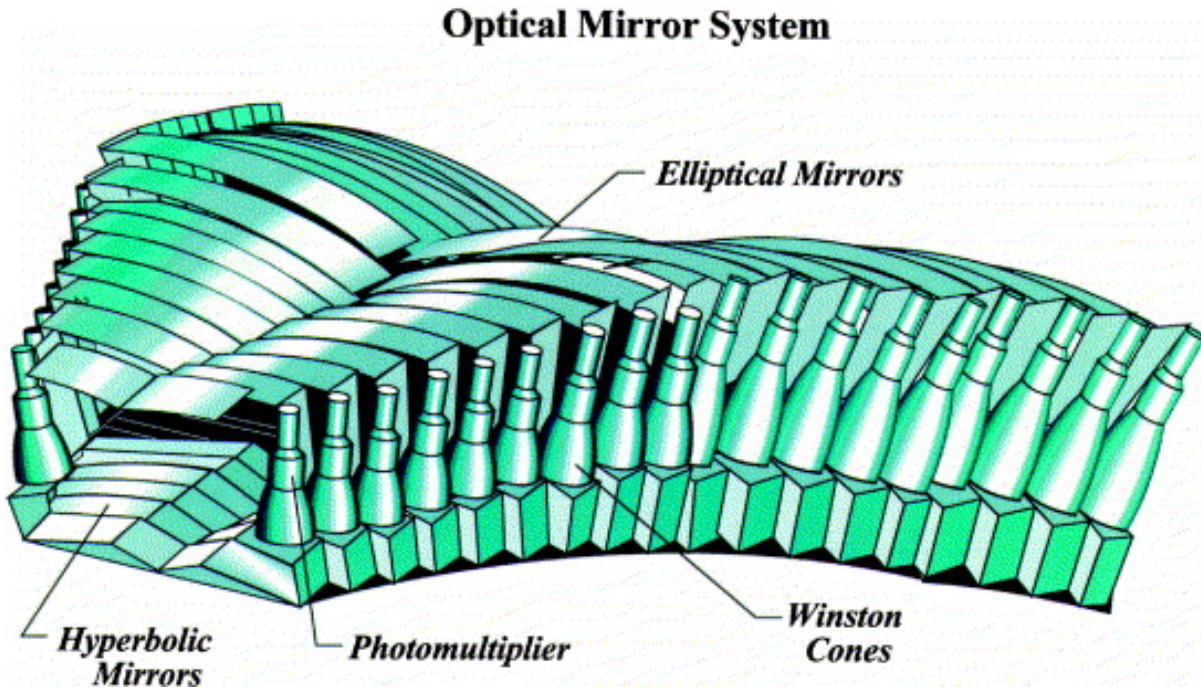


Figure 2.6: The CLAS Cherenkov Counter.

onds. The timing resolution for longer bars was designed to be 160 picoseconds, and measurements performed after the detector construction showed that the average timing resolution over the detector was 163 picoseconds [? ].

During experiments where the electron beam was used, the start time for each event could be determined by assigning  $\beta = 1$  to the fastest electron measured in the final state. However, once the tagger magnet was powered on and photon beam was delivered on target, start time information came from the start counter. Originally designed as six separate counters, the start counter was constructed with three counters spanning the full angular range of the detector. The target was surrounded by these three thin scintillators which had sufficient resolution to determine the difference between two sequentially arriving bunches ( $\sigma \approx 350 \text{ ps}$ ).

## 2.2.4 CLAS Electromagnetic Calorimeter

The outermost layer of the CLAS detector was the electromagnetic calorimeter (EC). This sampling calorimeter was a main component of the CLAS trigger and had several important roles. Foremost, the EC detected and triggered on electrons with  $E > 0.5 \text{ GeV}$ . Detecting neutral particles such as photons and neutrons was a secondary role. By detecting photons with energies higher than 200 MeV, and having sufficient granular resolution, strongly decaying ( $\pi^0$  or  $\eta$ )  $\rightarrow \gamma\gamma$  particles were measured. Separation of neutrons and photons was achieved by combining information from the EC with timing information from the CLAS time of light system [? ].

Structurally, the EC was composed in total of 1296 PMTs and 8424 scintillating strips in the six EC

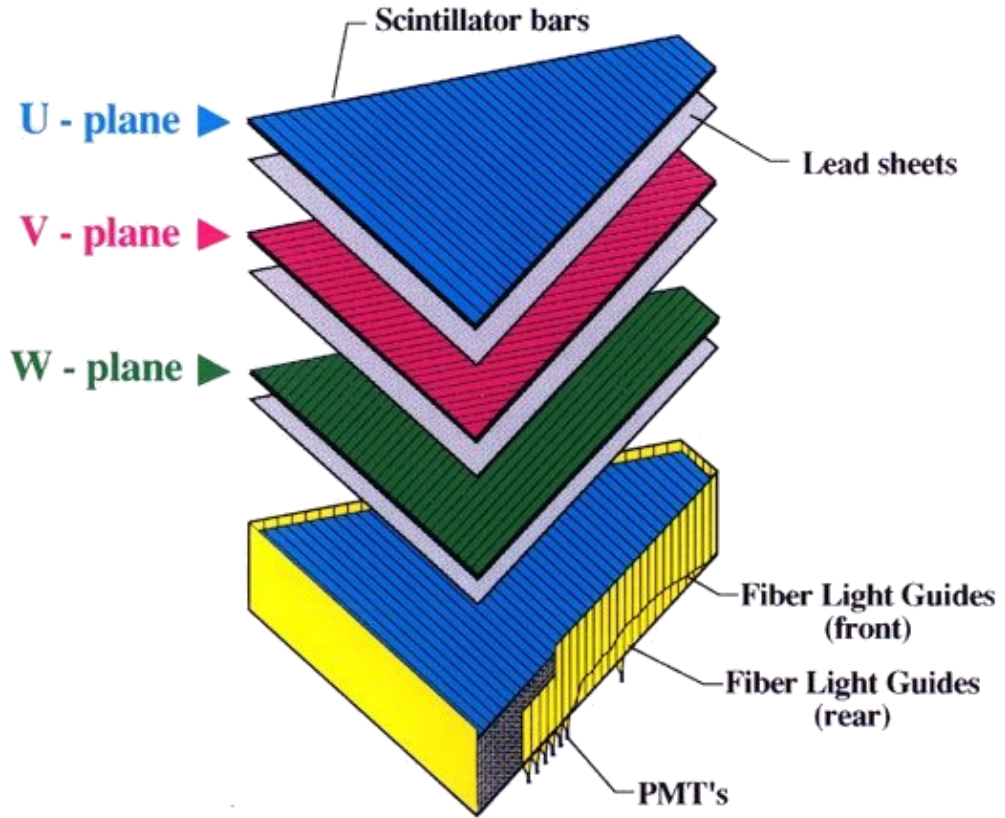


Figure 2.7: The U, V, W structure of CLAS electromagnetic calorimeter is shown above.

modules (one per sector). Alternating layers of lead and scintillator material were used to create a sampling fraction  $E_{dep}/p$  of approximately 0.3 for electrons. Measuring just 10 mm thick, and with a width of 10 cm (to balance cost of PMTs and granularity), the length of the scintillating strips depended on the angular location. Each EC module contained 3 sets of 13 layers offset by  $120^\circ$  to provide spatial information, these layers were referred to as U, V, and W.

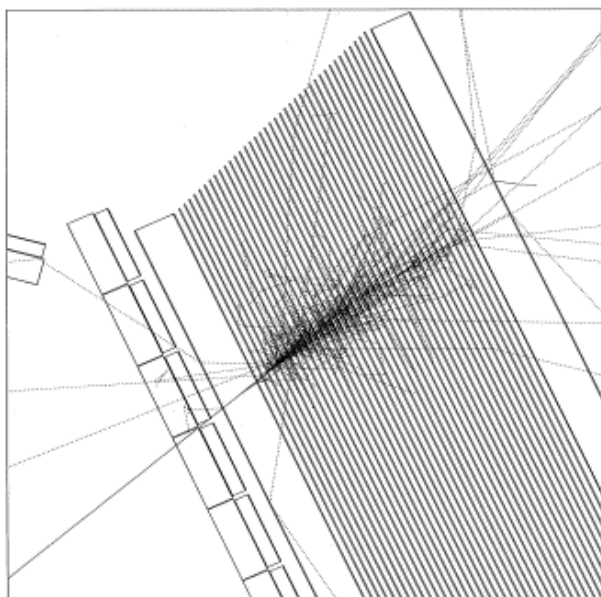


Figure 2.8: GEANT simulation of an electron showering in the EC. This figure originally appeared in [? ]

# Chapter 3

## Basic Analysis & Corrections

### 3.1 Introduction

This chapter discusses analysis procedures that are common to the subsequent data analyses of pions and kaons. These procedures can be divided into two groups. The first type of basic analysis described is the aggregation or calculation of scalar values over the run-period (examples include luminosity and helicity). The second type of analysis procedure described is a correction to measured values. Vertex corrections, timing corrections, and kinematic corrections will be discussed.

### 3.2 Luminosity Calculation

A useful concept in accelerator/collider physics is the luminosity  $\mathcal{L}$ . Luminosity is defined as the number of collisions per unit area per unit time that could lead to some process of interest. Consider as an example elastic scattering of electrons from protons, the luminosity is the number of electron-proton collisions per unit time per unit area. The rate  $\frac{dN}{dt}$  of the occurrence of events for some process  $X$  can be written in terms of this luminosity and the cross section for the process.

$$\frac{dN_X}{dt} = \mathcal{L}\sigma_X \quad (3.1)$$

For the fixed target case, the luminosity has a simple expression.

$$\mathcal{L} = \frac{j_e \rho_p l_T}{e} \quad (3.2)$$

Here  $l_t$  is the target length,  $\rho_p$  is the proton number density in the target, and  $j_e$  is the beam current. To find the total number of events which accumulate in some time  $t_{exp}$  the event rate is integrated with respect to time.

$$N_X = \int_0^{t_{exp}} \frac{j_e \rho_p l_T}{e} \sigma_X dt = \frac{\rho_p l_T}{e} \sigma_X \int_0^{t_{exp}} j_e dt = \frac{\rho_p l_T}{e} \sigma_X \Delta Q \quad (3.3)$$

Thus the experimentally observed cross section for some process  $X$  is,

$$\sigma_X = \frac{N_X}{\mathcal{L}_{int}} \quad (3.4)$$

where the number of events  $N_X$  is corrected for all effects and  $\mathcal{L}_{int}$  is the integrated luminosity as shown above.

Experimentally, the factor  $\Delta Q$  can be calculated from charge deposition measurements by the Faraday cup. The Faraday cup charge is a scalar value written periodically into the output event stream, not with every recorded event. This information is stored in the output BOS files in a bank called TRGS, the variable is named FCUP\_G2.

For this data analysis, the final ntuple (root files) used did not contain the Faraday cup charge information. For this reason, the authors used the BOS files directly and recorded the value of FCUP\_G2 for every scalar reading, as well as the event number directly after each scalar entry (from the HEAD bank). This event number correlates directly to the event number stored in the root files used for analysis.

The total accumulated charge over a run is simply the sum over consecutive differences in the Faraday cup charge.

$$\Delta Q = \sum_{i=1}^{n-1} q[i+1] - q[i] \quad (3.5)$$

Here  $n$  denotes the number of scalar entries for a given file. Due to the periodic nature of the scalar bank writing events are also recorded after the last reading of the file, and before the first scalar reading of the next file in the run. To account for this the difference between consecutive files last and first readings is added to the total.

For the E1-F dataset, a run typically contains around 20 files, each representing a raw file size of 2 gigabytes. These files are named by run number, and given an index from 0 to  $n_{files} - 1$ . It is not uncommon that a run will contain missing files in the middle of the range. If this occurs, the charge difference between last/first reading is not added to the total.

Any charge which accumulates in a period of time where the number of events did not change is not

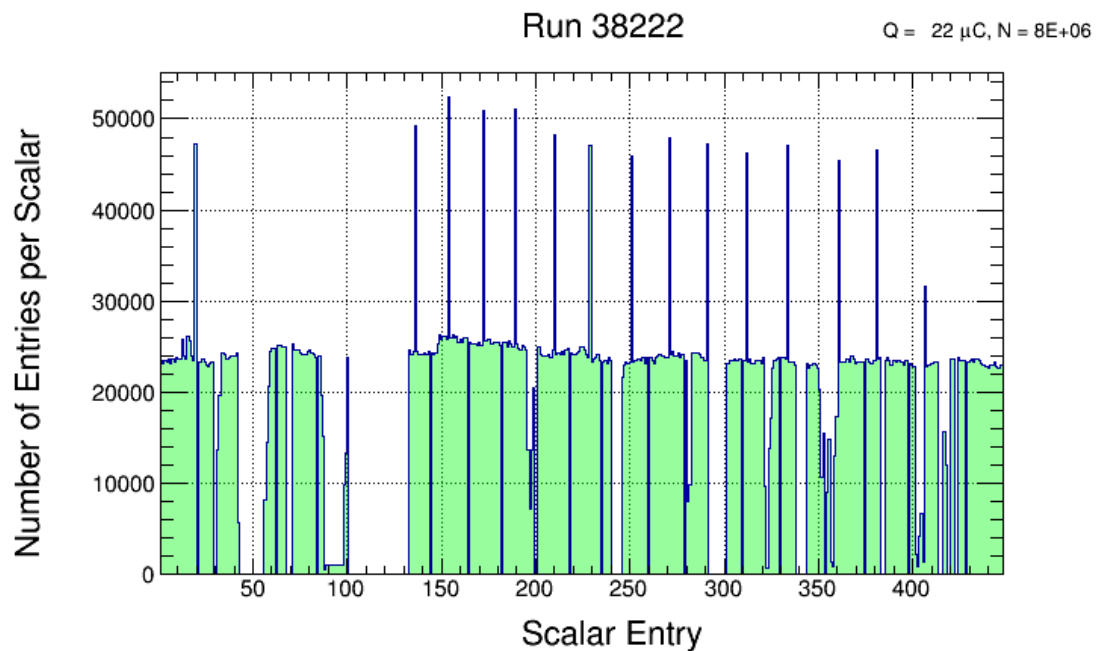


Figure 3.1: Entries per scalar reading for run 38222.

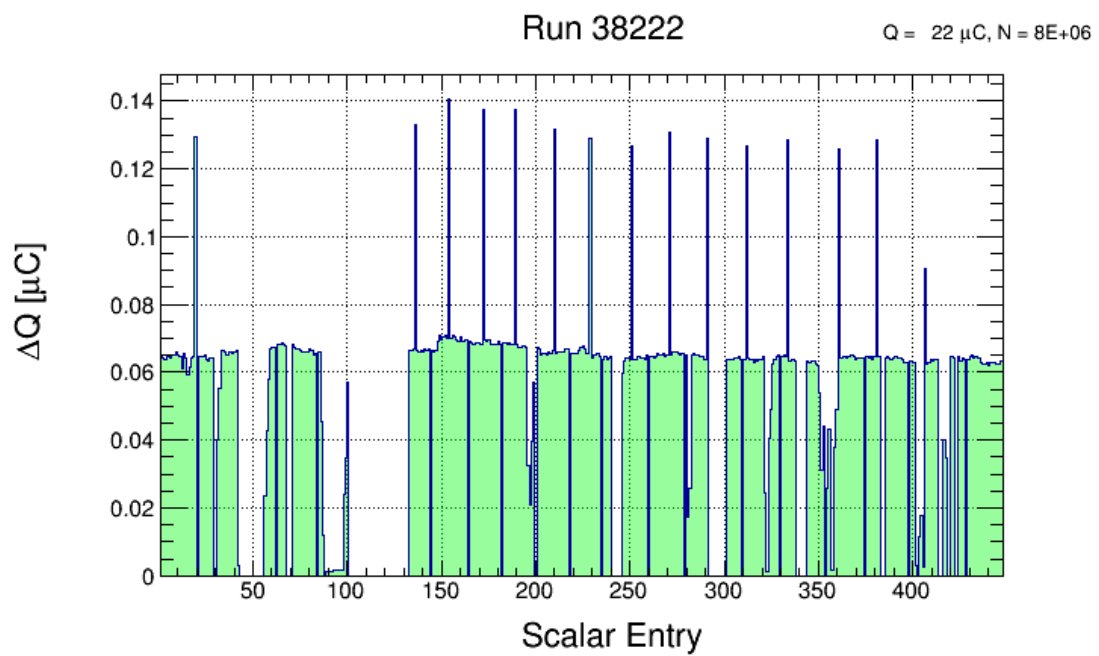


Figure 3.2: Charge per scalar reading for run 38222.

added to the total. Similarly, any events which occur within regions where no charge is recorded need to be discarded. This is accomplished by recording the bad event ranges for every file and removing these events from our analysis.

The result of this procedure is a numerical value of charge for each run. For practitioners, it is important to note that this value needs to be scaled by the DAQ scaling factor before it represents a value of charge. In our analysis, the numerical value of charge for a typical file is a few tens of micro-Coulombs.

### 3.3 Determination of Good Run List

The total dataset contains 831 runs. Due to the complexities of the CLAS experimental setup, it is not uncommon for run conditions to change during a small percentage of the runs such that the data collected are not of analysis quality. For this reason, a good run list is constructed.

Good runs are selected for the list by counting good electrons in each file and normalizing by the accumulated charge for the associated file. While the number of events collected varies from run to run the ratio defined above is a stable quantity – provided that the run conditions do not vary greatly. Runs which are within 3 standard deviations of the mean (calculated over the dataset) are used as good runs. The good run list used for this analysis contains 522 runs.

### 3.4 Helicity Determination

During the course of the E1-F run period the beam helicity convention was changed by the insertion of a half-wave plate at the injector. The definition of  $\pm$  helicity must change in accordance with these wave-plate insertions. To monitor these changes, the value of  $A_{LU}^{\sin \phi}$  for  $\pi^+$  is recorded for every run. Whenever the asymmetry (which has a magnitude of around 3%) changes sign, the sign convention has changed. These changes are taken into account in the data analysis.

### 3.5 Vertex Corrections

The track vertex position  $(v_x, v_y, v_z)$  is calculated based on the intersection of each track with the mid-plane (the plane which contains the beamline and bisects the sector at  $\phi_{rel} = 0$ ). If the beam is not centered at  $(x, y) = (0, 0)$ , the vertex position calculation needs to be corrected by shifting the mid-planes in accordance with the target offset. The offset  $(x, y)$  is identified by plotting events from the control foil placed near the target, which has a  $z$  position of -20 cm. For the E1-F run period, the beam

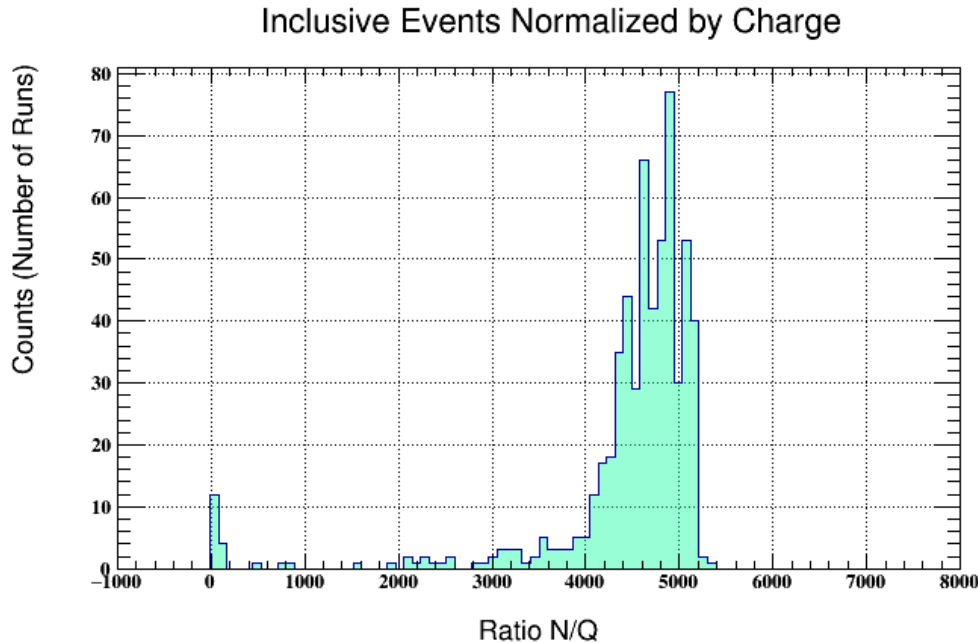


Figure 3.3: Inclusive electrons per file normalized by the total charge accumulated for the file. This quantity is used to make a good run list.

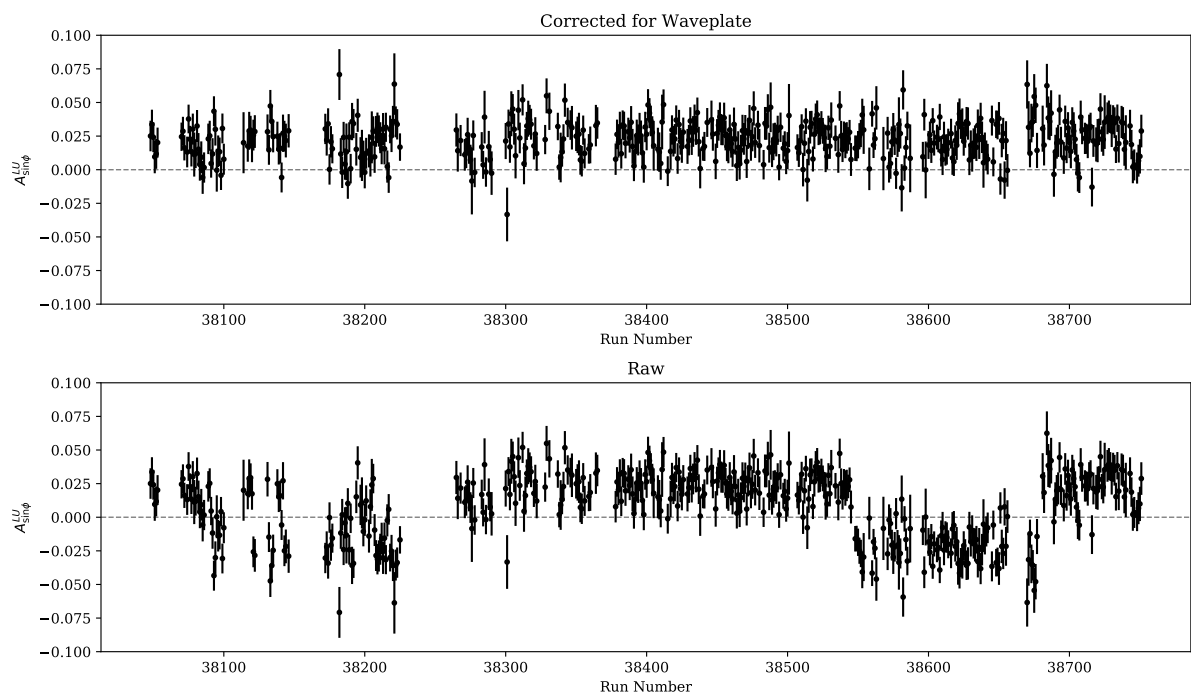


Figure 3.4: The waveplate position is determined and corrected by plotting the BSA for  $\pi^+$  mesons as a function of the run. The top panel shows the corrected results, the bottom shows the results before changing the helicity.

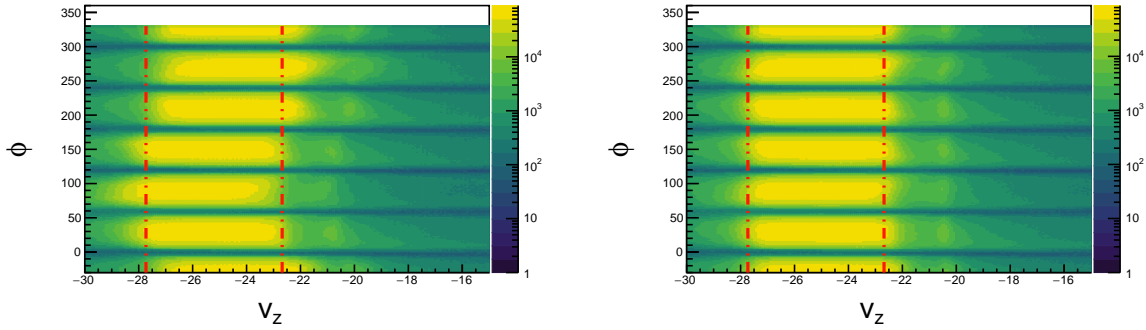


Figure 3.5: The z-vertex  $v_z$  position shown for different values of  $\phi$  the azimuthal angle in the hall. The left figure shows the distribution before corrections are applied, the right after. The vertical red lines bound the region which we define as acceptable for electrons in our analysis.

position was  $(0.15, -0.25)$  cm.

### 3.6 Timing Corrections

Timing information comes from the time-of-flight detector system. After calibration, small offsets in timing between time of flights paddles still exist for the E1-F dataset. These biases can be removed on a run-by-run and paddle-by-paddle basis by adding a small shift  $t_{corr}$ . In order to determine this shift  $t_{corr}$  for each paddle, charged pions are used.

Using momentum information from the drift chambers the value of  $\beta$  can be predicted and the difference  $\Delta\beta$  can be determined for each pion.

$$\Delta\beta = \beta_{obs} - \beta_{pred} = \frac{d}{ct_{obs}} - \sqrt{1 + (m/p)^2} \quad (3.6)$$

Here  $m$  is assumed to be  $m_\pi$ . The offset  $\Delta\beta$  from 0 is used to define the value of  $t_{corr}$  for each paddle. If this value is exceedingly small, no correction is applied. For some paddles with low statistics a reasonable value for  $t_{corr}$  cannot be obtained and these paddles are excluded from the analysis.

In the method described above, the calibrated paddle is the one which is struck by the pion. The electron paddle which was struck could also require calibration. In practice the magnitude of the correction term  $t_{corr}$  is small, and the paddle offset is (likely) randomly distributed about 0 when considering all paddles. By including events from many different (electron) paddles, miscalibration effects from the electron side cease to be important. This is demonstrated by the success of the technique in centering the  $\Delta\beta$  distributions. This work was first described in [?].

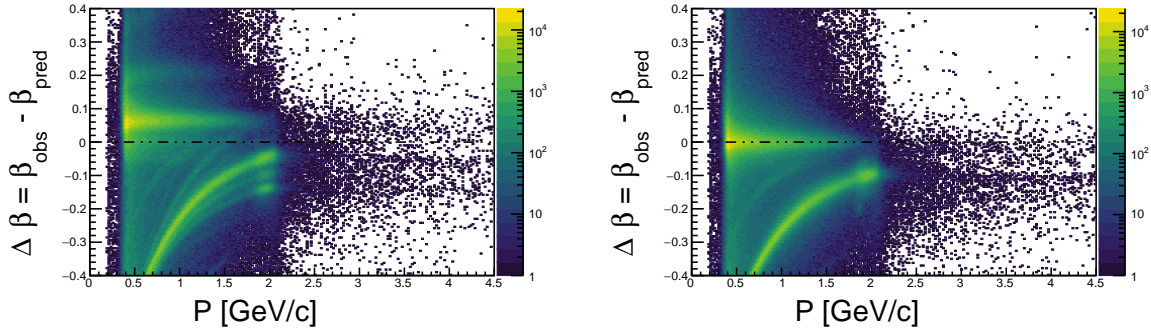


Figure 3.6: Timing corrections are shown for paddle 24 of sector 1. The left image shows the  $\Delta\beta$  distribution before corrections. On the right the same is shown after correction of the timing for this paddle. We assume the mass of the track to be the pion, these show up as the green band. Heavier protons are visible below the pion band.

### 3.7 Kinematic Corrections

The magnetic field map used in reconstruction to swim particle tracks cannot perfectly match the real magnetic field of the hall. As a result of this the reconstructed momentum of particles is often slightly off (of order 1%). Small misalignments in detector positions also contribute to this effect. In order to correct for these small differences, the momentum  $(p_x, p_y, p_z)$  and hence  $\theta$  of charged tracks is corrected.

Various procedures exist for the correction of kinematic variables of measured particles, and they all rely on energy and momentum conservation applied to standard processes (such as elastic scattering). The procedure used to derive corrections for the E1-F dataset was developed and described by Marco Mirazita in [? ].

As mentioned previously, the need for correction to  $\theta$  (the polar angle measured from the beamline) arises from misalignments in the drift chambers. This implies that the correction will be the same for positives and negatives, and this assumption is used in the correction algorithm. First, elastic ( $ep \rightarrow ep$ ) events are selected by identifying events that contain at least one electron and one proton, then requiring that the missing mass  $M_X$  of the  $(ep \rightarrow epX)$  system is close to 0. The kinematics of the event are then calculated.

$$k^\mu = (k, 0, 0, k) \quad (3.7)$$

$$p^\mu = (M_p, 0, 0, 0) \quad (3.8)$$

$$k'^\mu = (k', k' \sin \theta, 0, k' \cos \theta) \quad (3.9)$$

$$p'^\mu = (E_p, -p' \sin \alpha, 0, p' \cos \alpha) \quad (3.10)$$

Applying energy and momentum conservation to the equations above yields 3 equations.

$$k + M_p = k' + \sqrt{M_p^2 + p'^2} \quad (3.11)$$

$$k' \sin \theta = p' \sin \alpha \quad (3.12)$$

$$k = k' \cos \theta + p' \cos \alpha \quad (3.13)$$

Using these equations, the electron angle  $\theta$  and the proton angle  $\alpha$  can be predicted by using the momenta  $(k', p')$ . These values are compared with measured values and iteratively corrected by tuning the parameters of a phi-dependent 2nd order polynomial.

$$\cos \theta = 1 - M_p \frac{k - k'}{kk'} \quad (3.14)$$

$$\tan \alpha = \frac{1}{p'} \frac{k' \sin \theta}{k - k' \cos \theta} \quad (3.15)$$

After  $\theta$  corrections are applied, the momentum of the electrons are corrected by using an analogous procedure for  $k'$  instead of  $\theta$  and  $\alpha$ . The momentum corrections are calculated as functions of  $\phi$  for each sector in one degree bins of  $\theta$ . Finally, the positively charged particles momenta are corrected by selecting the exclusive event ( $ep \rightarrow e\pi^+N$ ). In this reaction the scattered electron and pion are detected and the neutron is selected using a missing mass cut. Assuming the electron momentum, electron angle, and pion angle to be correct, the pion momentum correction is then calculated by iteratively improving the central position of the neutron mass peak to coincide with  $M_N$ . Marco Mirazita shows in his note that these corrections can be satisfactorily applied to all negative and positive particles.

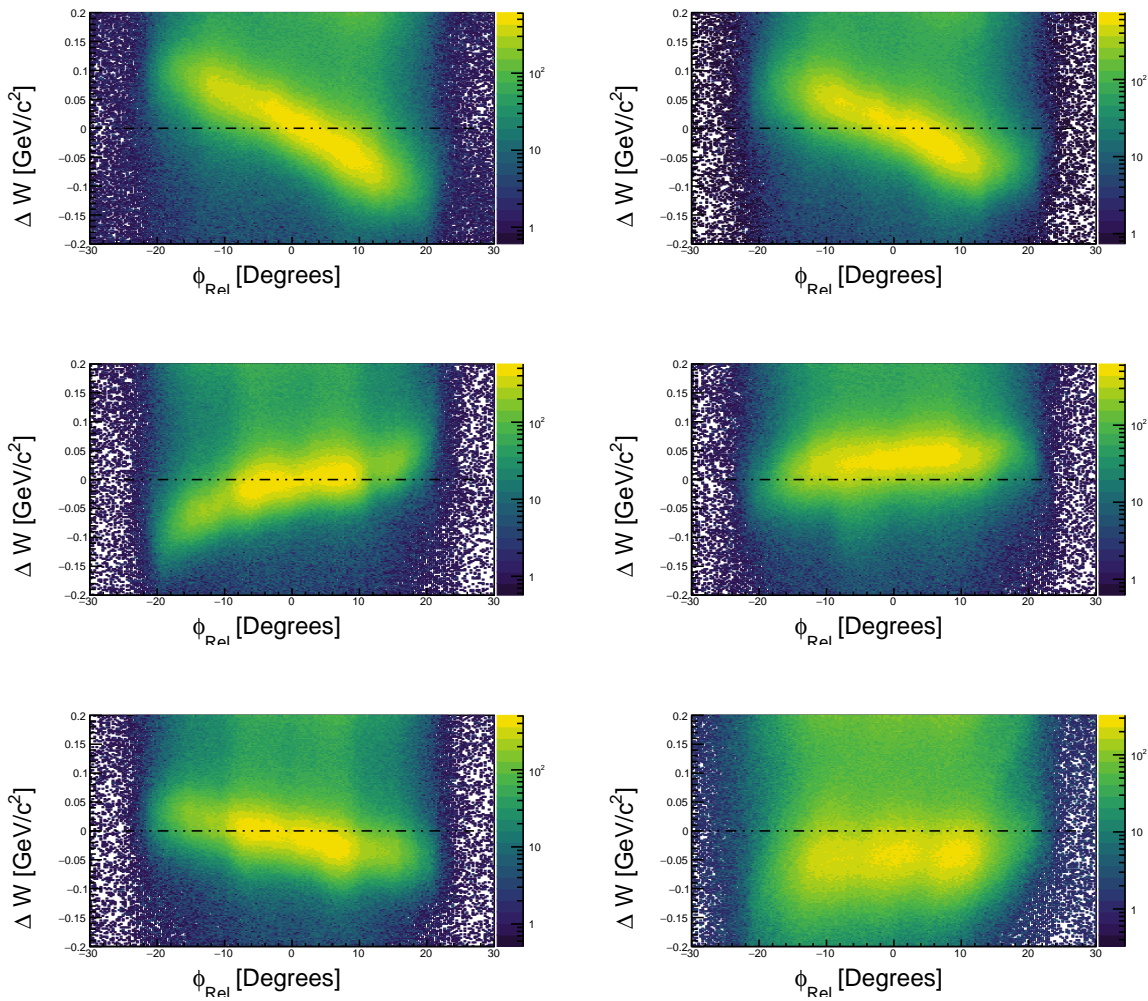


Figure 3.7: This figure shows the deviation from  $M_p$  of the  $W$  spectrum peak for elastic  $ep \rightarrow ep$  events (before corrections).

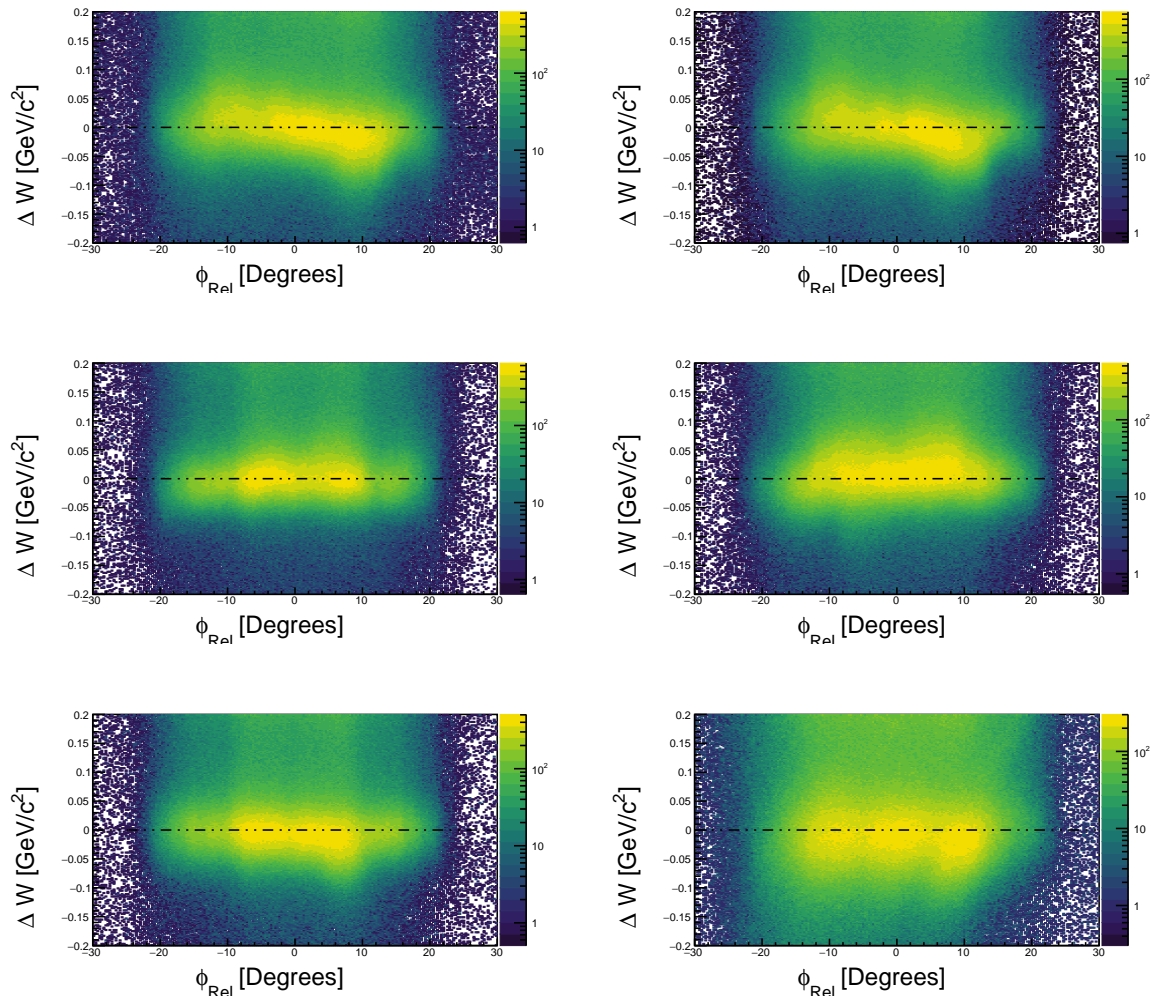


Figure 3.8: This figure shows the deviation from  $M_p$  of the  $W$  spectrum peak for elastic  $ep \rightarrow ep$  events (after  $\phi$ -dependent corrections).

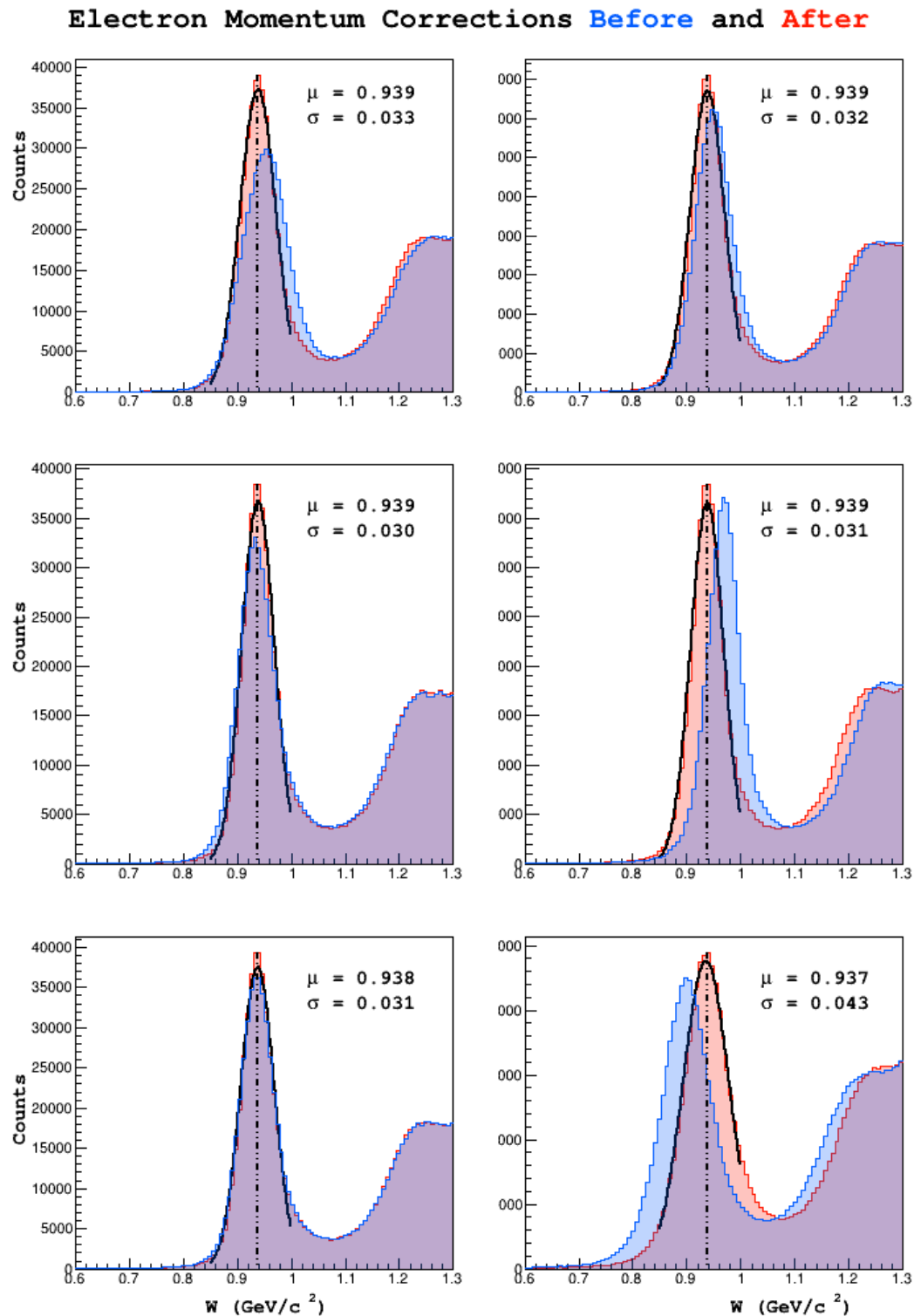


Figure 3.9: Elastic events shown in the spectrum of  $W$  before and after momentum corrections are applied.



# Chapter 4

## Particle Identification

### 4.1 Introduction

Particle identification (PID) is the process of classifying tracks as known particles. After reconstruction and matching of detector responses to each track, the reconstruction package `reccsis` assigns a preliminary particle identification based on loose selection criteria. In this analysis, tracks are classified based on a more stringent criteria. This chapter discusses the methodology used by the authors to classify particles.

### 4.2 Electron Identification

Electrons in CLAS are abundant, and the detection of an electron is a basic necessity for every event that will be analyzed. The most naive approach to performing electron identification would be to call all negatively charged tracks electrons. Doing this would provide an extremely efficient identification of electrons (none of them are missed), however the purity of the sample (the fraction of tracks identified as electrons that are actually electrons) would be low due to the vast quantity of negatively charged pions that are produced in during the experiment. Additionally, doing this would completely eliminate the possibility of identifying negatively charged pions or kaons, as all negative tracks would be called electrons. In practice then, the identification of electrons is concerned with removal of negative pions and kaons from the sample of negative tracks. This is accomplished by applying a series of cuts on measured variables that distinguish between electrons and pions (pions are the dominant background).

#### 4.2.1 Electron ID Cuts

The cuts used to select electrons are enumerated below.

- Negative charge

- Drift chamber region 1 fiducial
- Drift chamber region 3 fiducial
- Electromagnetic Calorimeter fiducial (UVW)
- EC minimum energy deposition
- Sampling Fraction (momentum dependent)
- z-vertex position
- Cherenkov counter  $\theta_{cc}$  matching to PMT number
- Cherenkov counter  $\phi_{rel}$  matching to PMT (left/right)

Each cut is now be described in more detail.

### Negativity Cut

Each track is assigned a charge based on the curvature of it's trajectory through the magnetic field of the torus. This is done during the track reconstruction phase. Tracks are eliminated as electron candidates if they are not negatively charged.

### Drift chamber fiducial

The fiducial region or volume is a term used to refer to the region of a sensitive detector which is unimpeded in it's acceptance of physics events. In practice, shadows from other detectors, poorly understood edge effects, or geometric obstacles may impede the flight of particles from the target, and render regions of sensitive detectors unreliable (to use the vocabulary presented above, these events fall outside of the fiducial region of the detector).

Negative tracks which pass geometrically close to the edges of the drift chamber are, from a tracking perspective, more difficult to understand. Additionally, tracks which fall outside of the fiducial region of the drift chambers are likely to fall outside of the fiducial region of the downstream detectors as well. For these reasons, it is common to remove tracks which are geometrically close to the boundaries of the drift chambers in region 1 as well as region 3 coordinate systems.

To implement this cut the  $(x, y)$  coordinates of the drift chambers are rotated into one sector. Then boundaries  $y_{left}, y_{right}$  are defined as linear functions of  $x$ . The boundary lines are parametrized by an offset  $h$  and an angle of the boundary line with respect to the center of the sector at  $x = 0$ . The slope of these lines is  $\pm \cot(\theta)$ .

Region	Height $h$ (cm)	Angle $\theta$ (degrees)
1	22	60
3	80	49

Table 4.1: Cut parameters used for the DC fiducial cut.

EC Coordinate	Min (cm)	Max (cm)
U	70	400
V	-	362
W	-	395

Table 4.2: Cut parameters used for the EC fiducial cut.

$$y_{right} = h + \cot(\theta)x \quad (4.1)$$

$$y_{left} = h - \cot(\theta)x \quad (4.2)$$

Tracks passing this criterion are those which have  $y > y_{left}(x)$  and  $y > y_{right}(x)$ .

### Electromagnetic Calorimeter fiducial (UVW)

As particles traverse the electromagnetic calorimeter they develop electromagnetic showers. If the track passes close to the edges of the detector, there is a chance that the shower will not be fully contained within the calorimeter volume (it spills out the edges). For this reason, it is standard to remove the hits which fall within the outer 10 centimeters of each layer of the EC (10 centimeters is the width of a scintillator bar). This cut is applied in the U, V, W coordinate system.

### EC minimum energy deposition

One way to differentiate between these electrons and pions is to exploit the difference in energy deposition between the two in the electromagnetic calorimeter. Electron typically develop a much larger and more energetic shower than  $\pi$  mesons, which minimally ionize the calorimeter material. The result is that the total energy deposition is typically larger for electrons than  $\pi$  mesons. In this analysis we require that at least 60 MeV was deposited in the inner calorimeter for electron candidates.

### Sampling Fraction (momentum dependent)

The electromagnetic calorimeter is designed such that electrons will deposit  $E_{dep}/p \approx 0.3$  approximately one-third of their energy, regardless of their momentum. In contrast to this, the ratio  $E_{dep}/p$  for  $\pi$  mesons decreases rapidly with momentum. To develop a momentum dependent cut for this distribution, all negative candidates are first filled into a two-dimensional histogram of  $E_{dep}/p$  vs.  $p$ . The histogram is then binned more coarsely in momentum, and projected into a series of 40 momentum

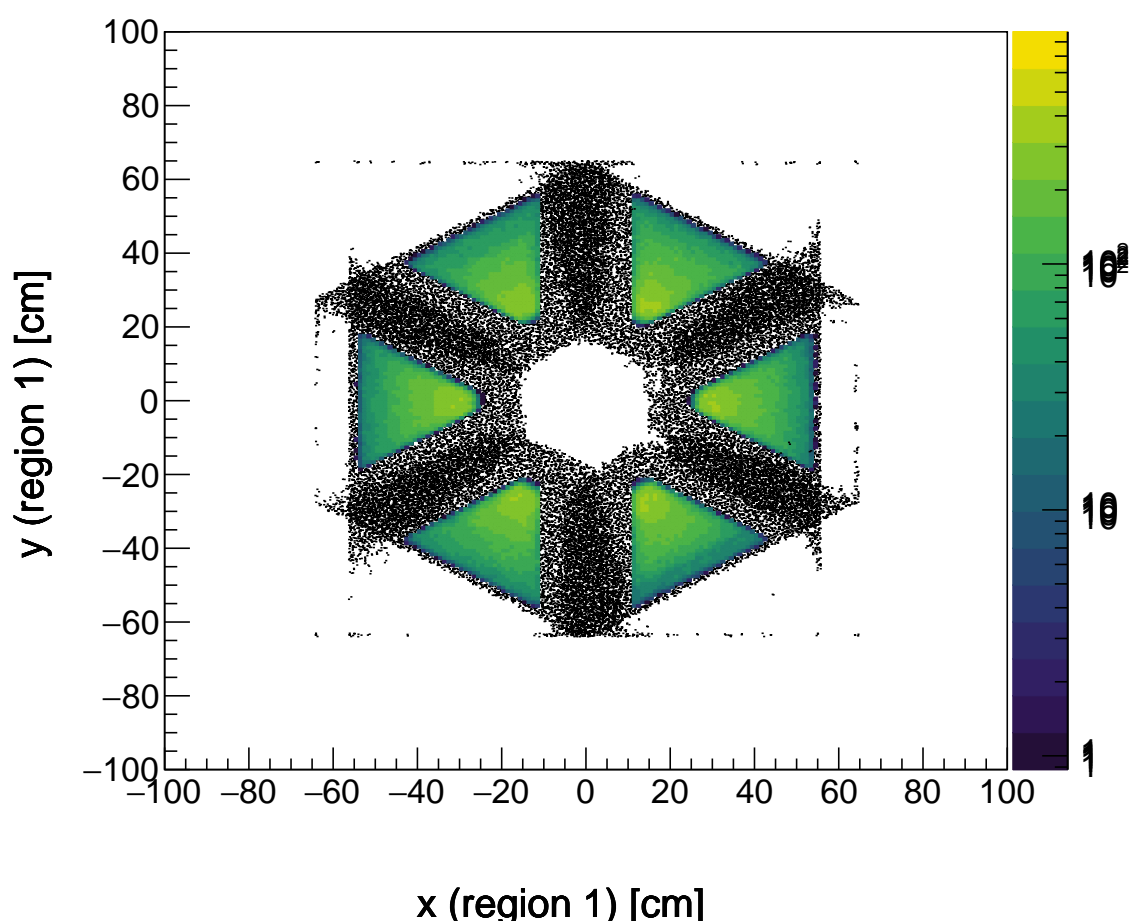


Figure 4.1: Tracks shown in color remain after the application of drift chamber region 1 fiducial cuts to all cuts, shown here as black points.

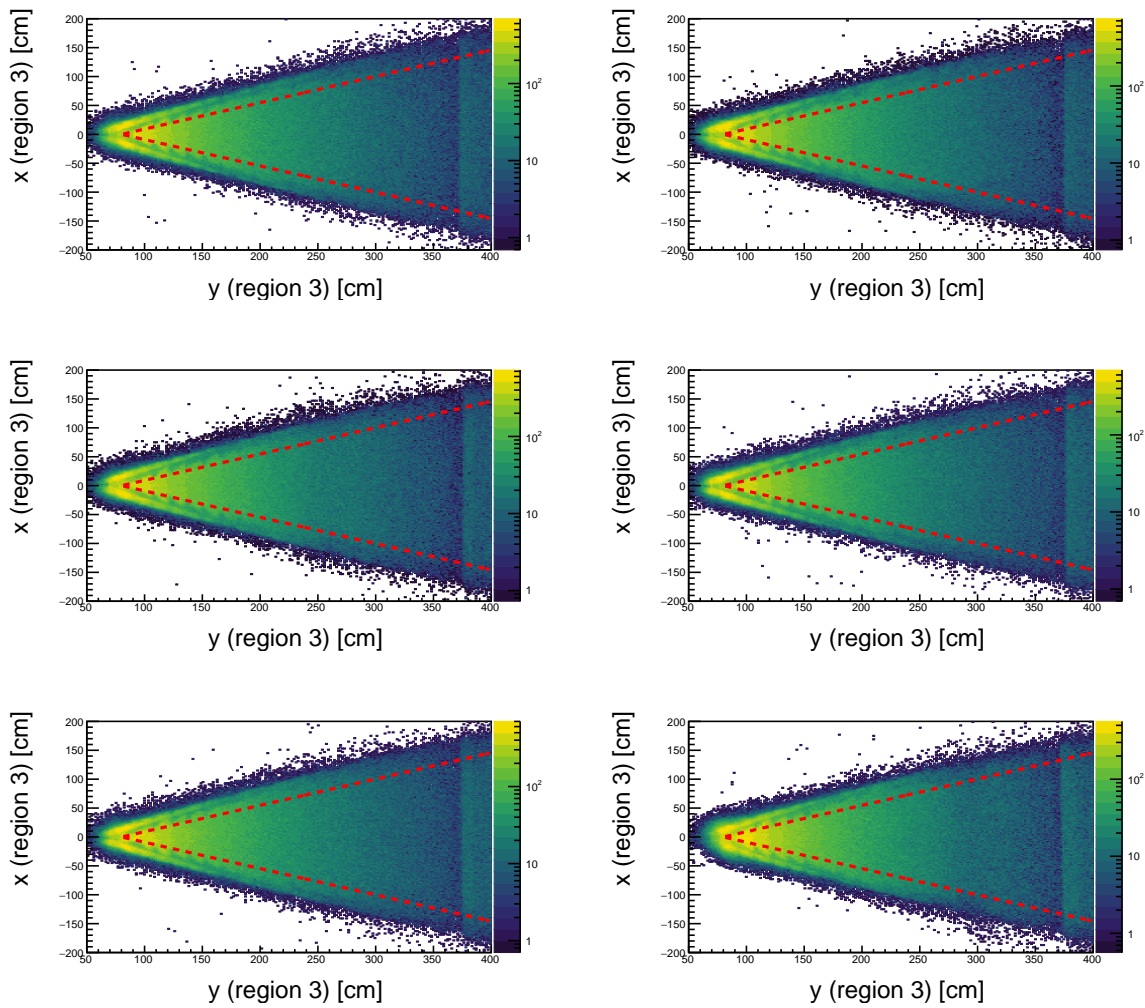


Figure 4.2: The selection criteria shown in red is applied to drift chamber region 3.

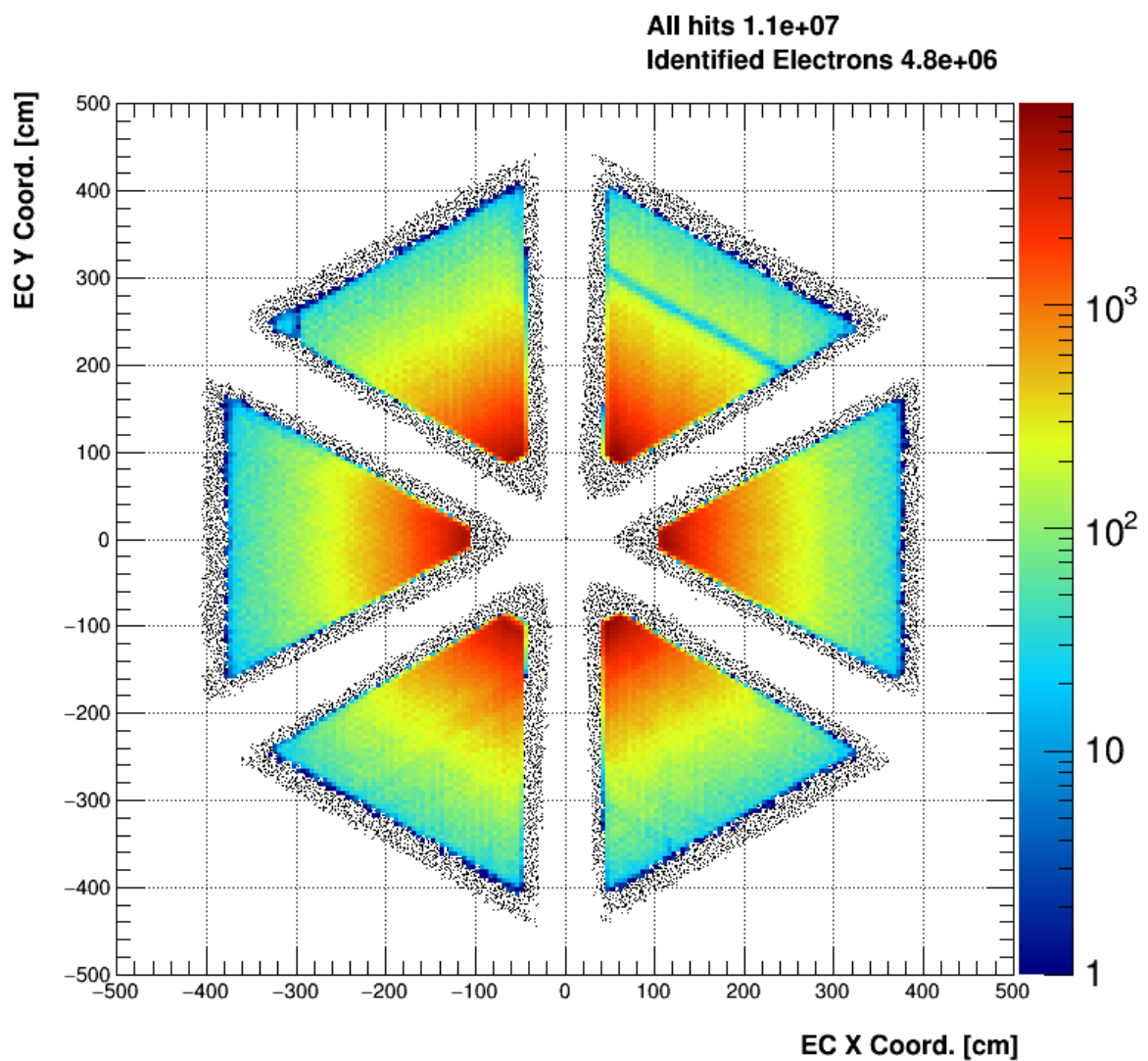


Figure 4.3: All negative tracks are shown here in black. In color, the tracks which pass the EC fiducial cut are shown.

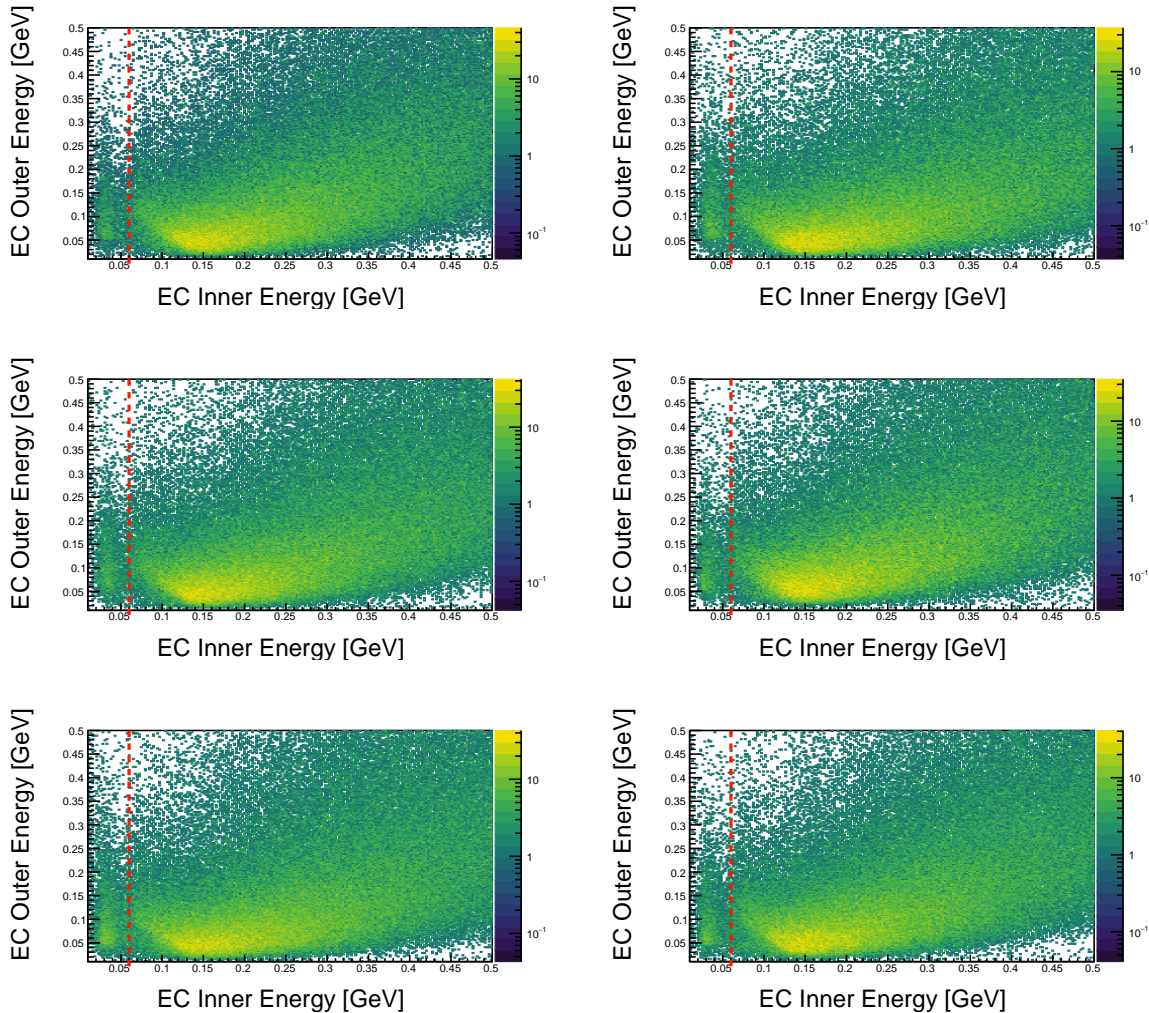


Figure 4.4: Each panel shown above contains events from one sector, increasing from 1-6 from top left to bottom right. The value selected of 60 MeV is applied to all sectors and separates the negatively charged pions (left) from the electrons (right).

slices. Each of these slices is fit with a Gaussian to extract the position  $\mu_i$  and width  $\sigma_i$  of the electron peak. Finally, a functional form for the mean and standard deviation of the distributions is chosen to be a third order polynomial in momentum.

$$\mu(p) = \mu_0 + \mu_1 p + \mu_2 p^2 + \mu_3 p^3 \quad (4.3)$$

$$\sigma(p) = \sigma_0 + \sigma_1 p + \sigma_2 p^2 + \sigma_3 p^3 \quad (4.4)$$

Boundaries are constructed from this information by adding (subtracting)  $n_\sigma$  from the mean. In the nominal case, we use  $n_\sigma = 2.5$ .

$$f_{max}(p) = \mu(p) + n_\sigma \sigma(p) = (\mu_0 + n_\sigma \sigma_0) + (\mu_1 + n_\sigma \sigma_1)p + (\mu_2 + n_\sigma \sigma_2)p^2 + (\mu_3 + n_\sigma \sigma_3)p^3 \quad (4.5)$$

$$f_{min}(p) = \mu(p) - n_\sigma \sigma(p) = (\mu_0 - n_\sigma \sigma_0) + (\mu_1 - n_\sigma \sigma_1)p + (\mu_2 - n_\sigma \sigma_2)p^2 + (\mu_3 - n_\sigma \sigma_3)p^3 \quad (4.6)$$

Due to slight differences between the 6 sectors of the CLAS detector, this cut is calibrated and applied for each sector individually. Results are shown in table 4.3.

Parameter	Sector 1	Sector 2	Sector 3	Sector 4	Sector 5	Sector 6
$\mu_3$	-8.68739e-05	0.000459313	9.94077e-05	-0.000244192	-7.65218e-05	-0.000392285
$\mu_2$	-0.000338957	-0.00621419	-0.00267522	-0.00103803	-0.00222768	-0.00105459
$\mu_1$	0.0191726	0.0393975	0.02881	0.0250629	0.0233171	0.0265662
$\mu_0$	0.2731	0.296993	0.285039	0.276795	0.266246	0.25919
$\sigma_3$	-0.000737136	0.000189105	-0.000472738	-0.000553545	-0.000646591	-0.000633567
$\sigma_2$	0.00676769	-0.000244009	0.00493599	0.00434321	0.00717978	0.00626044
$\sigma_1$	-0.0219814	-0.00681518	-0.0180929	-0.0140827	-0.0246181	-0.022029
$\sigma_0$	0.0474188	0.0475098	0.0461743	0.0492728	0.0546257	0.0517508

Table 4.3:  $\mu$  and  $\sigma$  values used to construct the momentum dependent sampling fraction cut.

### z-vertex position

Electrons can be produced as part of  $e^+e^-$  pairs, or by other processes. For this analysis, these are not of interest. For the purposes of this analysis it is then natural to accept only electron candidates which have a z-vertex  $v_z \in [-27.7302, -22.6864]$  within the expected target region. This cut is applied after the vertex position has been corrected (which is discussed in the basic analysis section).

### Cherenkov counter $\theta_{cc}$ and $\phi_{rel}$ matching to PMT

The angular arrangement of photo-multiplier tubes (PMTs) in the Cherenkov counter allows for additional consistency conditions to be applied. Each half-sector of the CC contains 18 PMTs increasing in polar angle away from the beamline, these divisions are known as segments. The polar angle measured

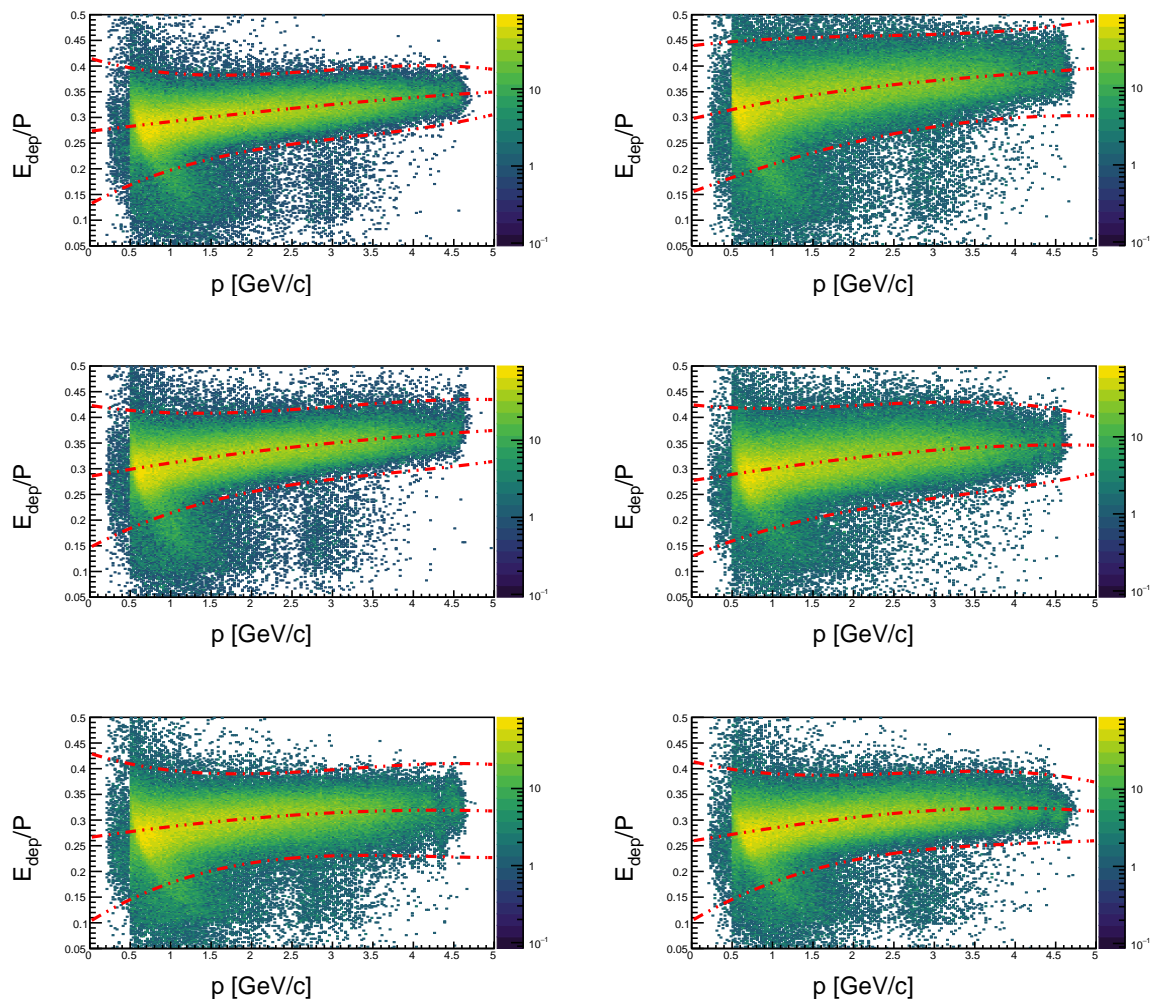


Figure 4.5: The sampling fraction selection boundary is shown here for the nominal value of  $N_{\text{sigma}} = 4$ .

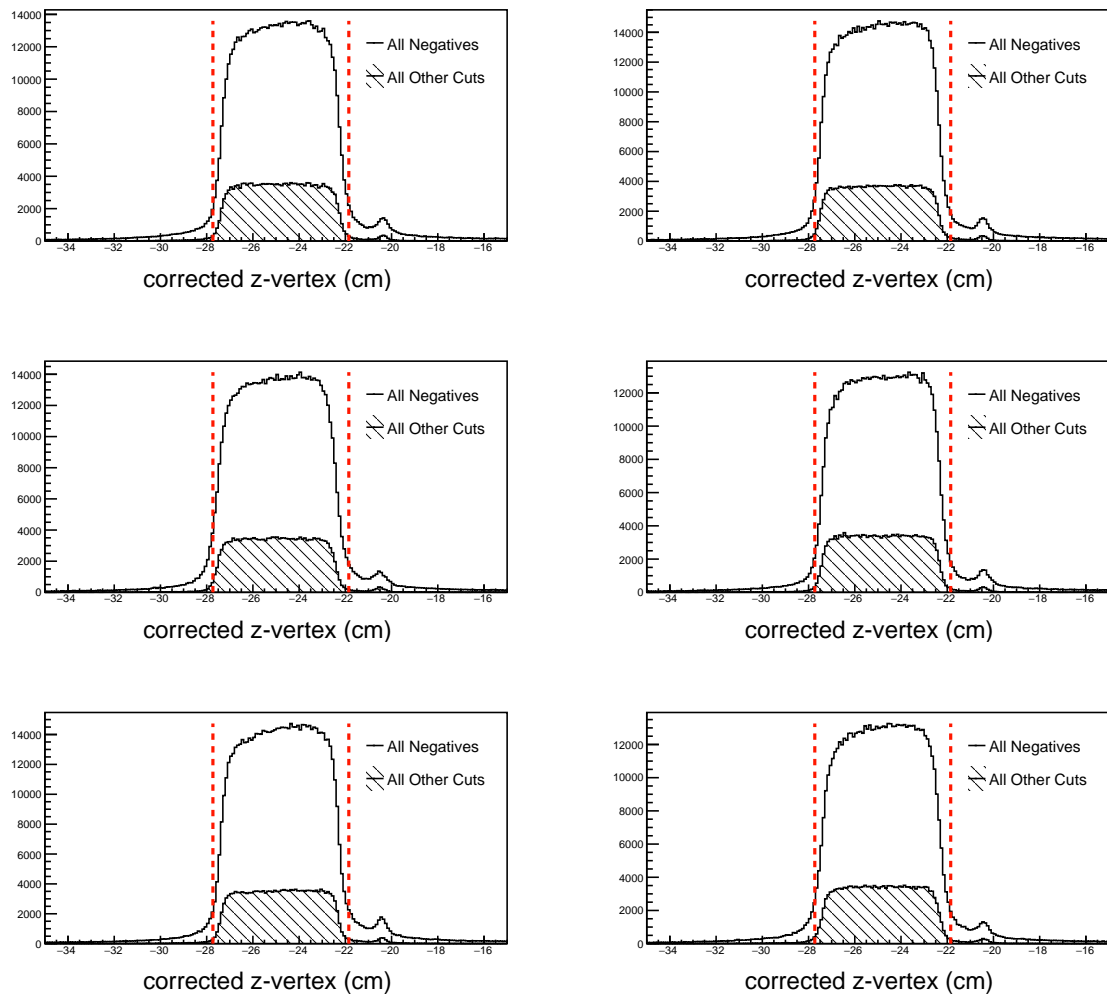


Figure 4.6: The track vertex cut is shown above. All negative tracks are shown in white, while the tracks passing all other criteria are shown in black hatch. The cut boundary is displayed as red lines. For E1-F the target center was located at -25 cm.

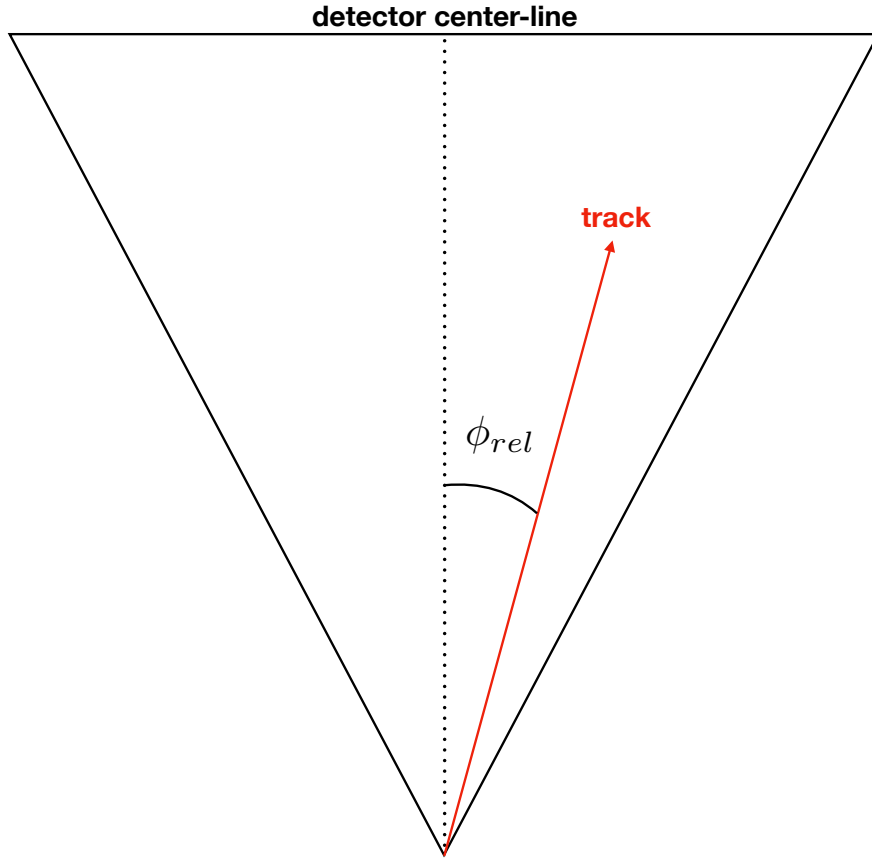


Figure 4.7: The angle  $\phi_{rel}$  is the azimuthal angle between the central line of the detector and the track.

at the Cherenkov counter  $\theta_{cc}$  is then correlated to the segment in which the track was detected. Additionally, PMTs that are placed on the left and right of the detector can be used to check consistency with the azimuthal angle the track forms with the central line of the detector (ie  $\phi_{rel} > 0$  means the track was in the right half of the sector,  $\phi_{rel} < 0$  means the track was in the left half of the sector). An integer is used to describe the PMT associated with the track. The left PMT is assigned value -1, the right 1, and a signal in both PMTs is assigned 0. If both PMTs have a signal, the track is allowed to pass. If the left PMT was the one that had a signal, only events with  $\phi_{rel} < 0$  passes. Similarly if the right PMT fired (code = 1), only events with  $\phi_{rel} > 0$  are allowed to pass. Technical note: the integers in question can be obtained from the ntuple22 format tree by doing the following.

---

```

for (int index = 0; index < event.gpart; index++) {
    int pmt = event.cc_segm[index]/1000 - 1;
    int segment = event.cc_segm[index]%1000/10;
}

```

---

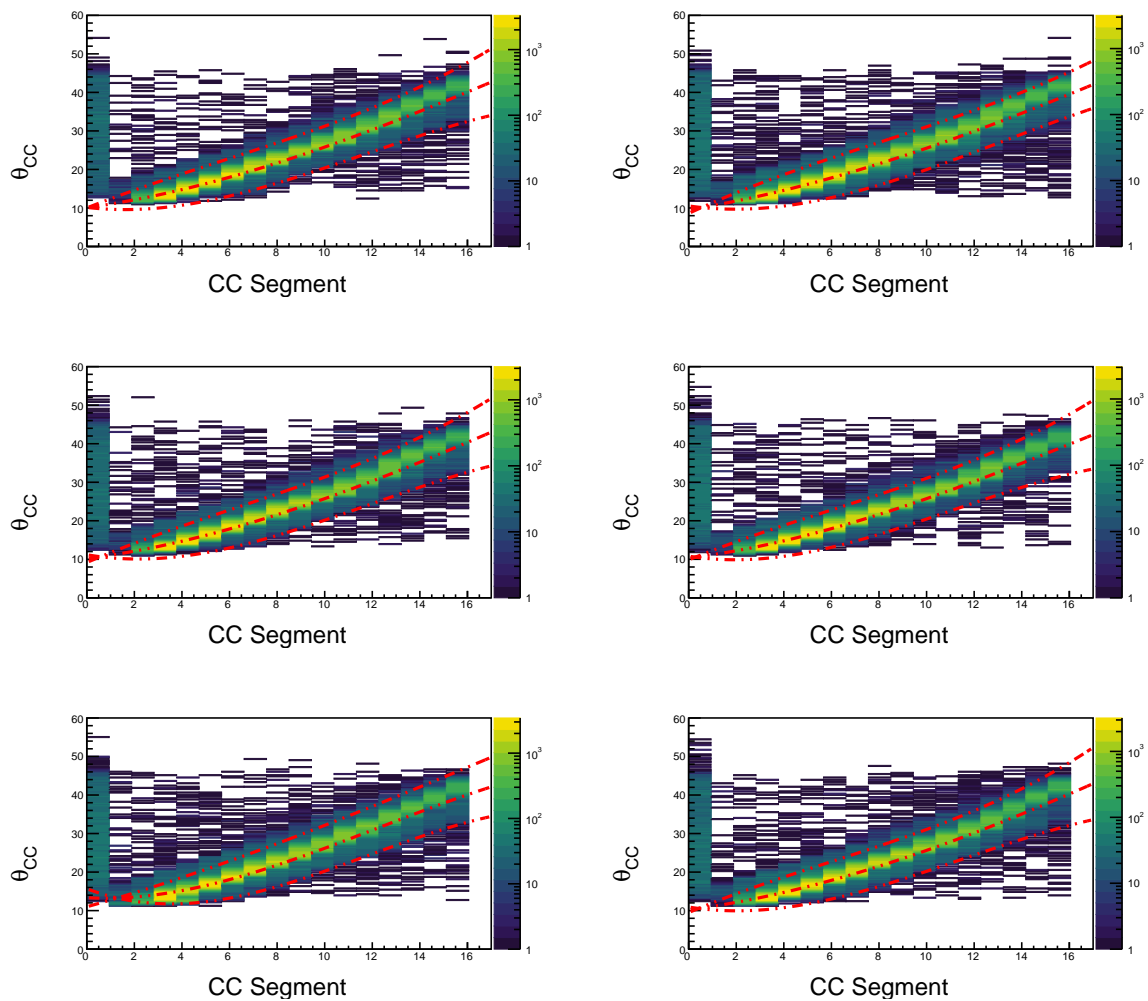


Figure 4.8: Correlation between  $\theta_{CC}$  and the CC segment is shown above, with our selection boundaries overlaid in red.

## 4.3 Hadron Identification

Hadron identification in CLAS is done by correlating particle momentum from the drift chambers with timing information supplied by the time of flight detector. In this analysis some quality assurance cuts are applied preliminarily, but they do not discriminate between different species of particle. The likelihood methodology described in this section is based on the discussion provided by the BES collaboration in [? ].

### 4.3.1 Hadron ID Cuts

The cuts used for hadron classification are enumerated below.

- Drift chamber fiducial
- Hadron-electron vertex difference
- Likelihood maximization of  $\beta(p, h)$

#### Drift chamber fiducial

Drift chamber fiducial cuts are applied (only region 1) using the same procedure as described for electrons. The parameters are for negative hadrons are those which are used for the electron. The parameters used for positive tracks are  $h = 10, \theta = 60$ .

#### Hadron-electron vertex difference

The distance between the electron vertex and the hadron candidate track vertex is computed ( $\delta v_z = v_z^e - v_z^+$ ). This distance is constrained to be within the length of the target (5 cm) see figure 4.3.1. This cut would not be applicable to studies where a significantly detached vertex is expected.

#### Likelihood maximization of $\beta(p, h)$

In this section, positive hadrons are used as an example. The same method is applied to the negative hadrons. For each particle species considered, a normalized probability density function  $P(x; p, h)$  is constructed for each input into the likelihood analysis. Here,  $x$  corresponds to the feature being used to categorize different particles (in our case,  $x$  is the  $\beta$  value measured by CLAS time-of-flight),  $p$  is the particle momentum, and  $h$  is the hadron being hypothesized (eg: the possible values for positive hadrons are pion, kaon, proton). In general if one uses a set of  $N$  variables  $x = (x_1, x_2, \dots, x_N)$ , the likelihood for a hypothesis  $h$  is defined below.

$$\mathcal{L}_h = \prod_{i=1}^N P_i(x_i; p, h) \quad (4.7)$$

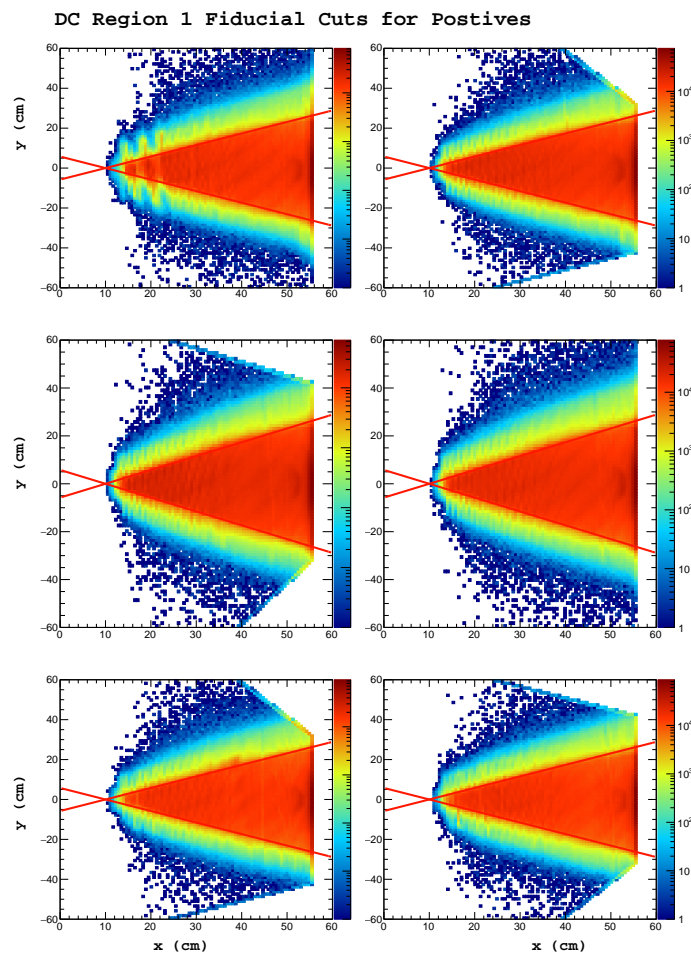


Figure 4.9: Shown above: Positive track hits on the region 1 drift chamber, events falling between the red lines are kept for analysis.

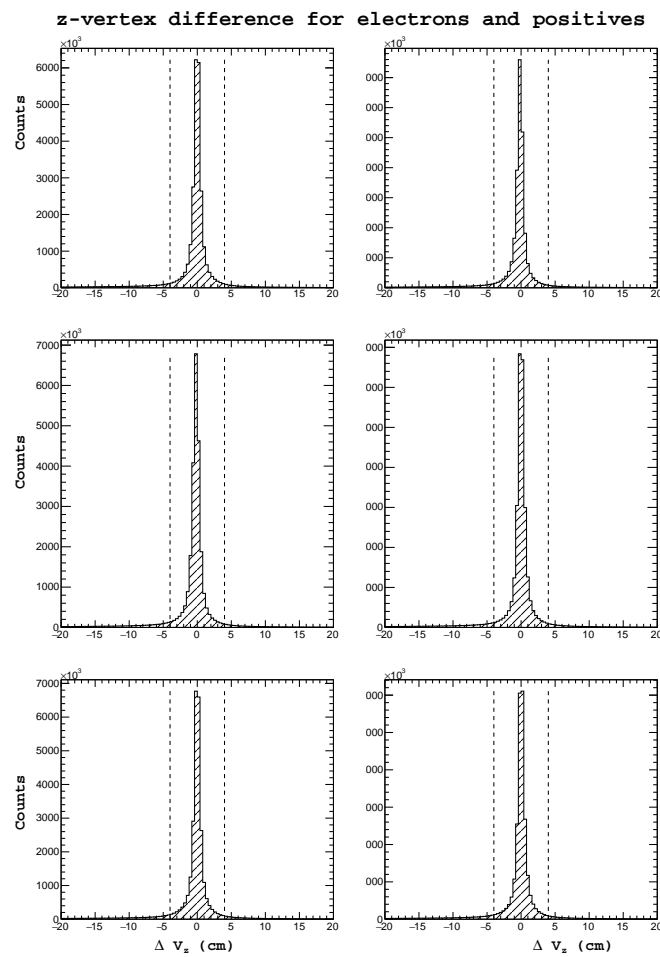


Figure 4.10: Shown above: The difference between the z-vertex position between detected electrons and positive tracks.

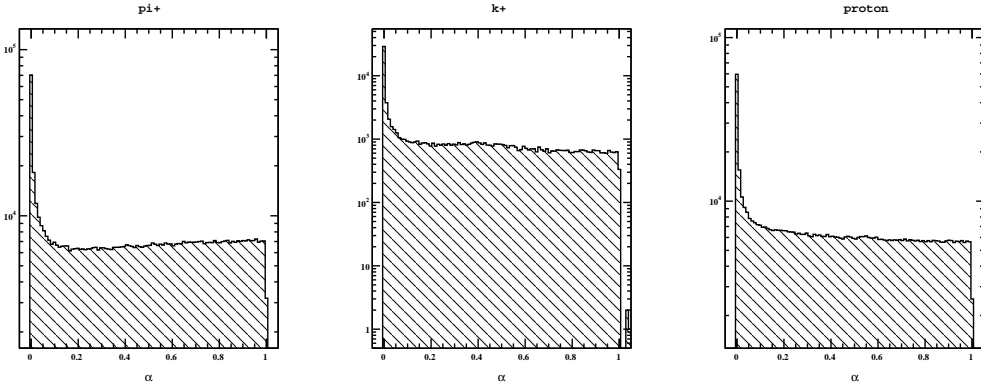


Figure 4.11: Shown above: The distribution of confidence level for all positive tracks after being classified by the likelihood ratio.

In our case, the only random variable we consider is  $\beta$ , and the likelihood is just the PDF. Here, and in many cases where the choice is statistically appropriate, it is possible to use a Gaussian PDF for the variable  $x_i$  (here  $\beta$ ).

$$P(\beta; p, h) = \frac{1}{\sqrt{2\pi}\sigma_\beta(p, h)} \exp \left\{ -\frac{1}{2} \left( \frac{\beta - \mu_\beta(p, h)}{\sigma_\beta(p, h)} \right)^2 \right\} \quad (4.8)$$

The identity is assigned by choosing the particle hypothesis  $h$  which maximizes the likelihood ratio.

$$\frac{\mathcal{L}_h}{\mathcal{L}_\pi + \mathcal{L}_K + \mathcal{L}_p} \quad (4.9)$$

Using this method, every positive track is assigned a particle identification. However, at times the likelihood value is quite small when compared with the maximum likelihood for that species. This is the case for positrons which are classified by this method as positive pions, because they are the closest particle for which a hypothesis has been provided. To avoid these situations, the confidence level  $\alpha$  of each track is calculated and a cut is applied on the minimum confidence. This cut can be easily varied to see how it changes the analysis result.

$$\alpha = 1 - \int_{\mu - \beta_{obs}}^{\mu + \beta_{obs}} P(\beta; p, h) d\beta \quad (4.10)$$

This quantity represents the probability to observe a value of  $\beta$  as far or farther from the mean as  $\beta_{obs}$ . Confidence levels close to zero correspond to tracks which are poorly identified as the class  $h$ . In the case that the PDF is Gaussian, the standard 1, 2, and 3  $\sigma$  cuts on  $\beta$  vs.  $p$  can be understood simply as confidence levels of approximately 0.32 = 1-0.68, 0.05 = 1-0.95, and 0.01 = 1-0.99.

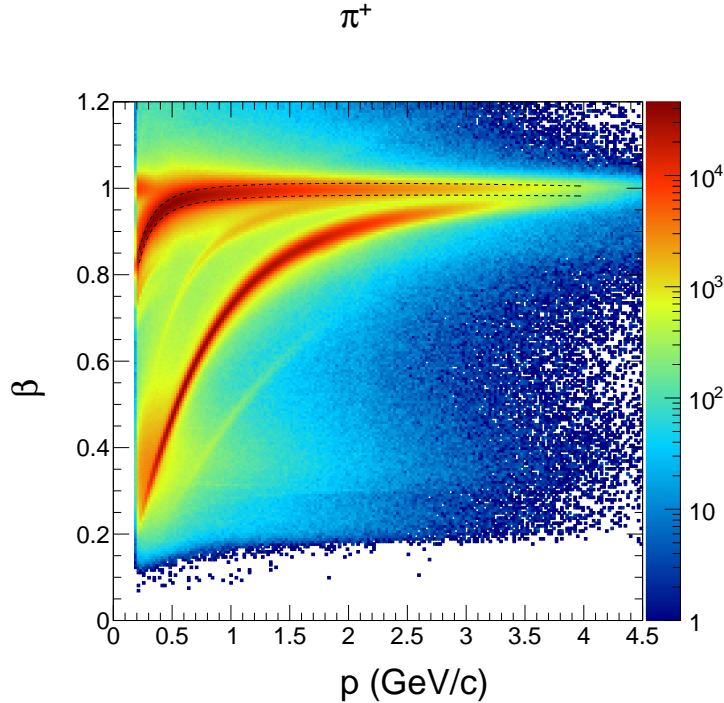


Figure 4.12: Shown above: All positive tracks overlaid with our determination of  $\mu(p) \pm \sigma(p)$  for  $\pi^+$

### Determination of probability density functions for likelihood method

The most important and most difficult part of constructing the likelihood ratio identification is the determination of the mean and standard deviation of the probability density function (which depends on momentum) for the different hypotheses. In the case where exceptionally accurate monte carlo (MC) simulations of the detector are available, one can use the truth information and track matching to construct the  $\beta$  vs.  $p$  2-dimensional histograms, and fit the  $\mu(p)$  and  $\sigma(p)$ . In the absence of high quality MC, analysts typically fit directly the spectrum of  $\beta$  vs.  $p$  and extract the mean and variance. In this work, an enhanced sample of candidates for each of the three positive particles in question is created before doing the fitting. In this way, we hope that our fit better represents the true  $\mu$  and  $\sigma$  for each particle. For fitting of pion and proton resolutions, positive tracks are assumed to be pions and the missing mass of the event is calculated. Then, a cut is placed around the neutron mass. In doing so, two main exclusive reactions are selected. The first is  $ep \rightarrow e\pi^+N$ , and the second is  $ep \rightarrow ep\pi^0$ . In this way most positrons, and positive kaons are removed from the sample prior to fitting. The mean and variance are fit using a third order polynomial in  $p$  (MINUIT  $\chi^2$  minimization is used). Negative pions and kaons are fit directly (as is normally done).

The parametrization used for the mean  $\mu(p, h)$  and resolutions  $\sigma(p, h)$  are shown below.

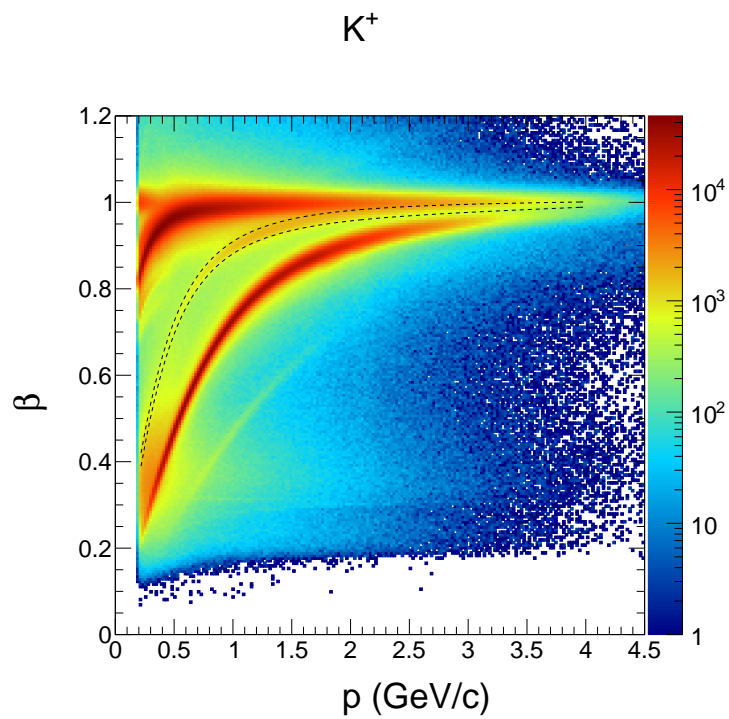


Figure 4.13: Shown above: All positive tracks overlaid with our determination of  $\mu(p) \pm \sigma(p)$  for  $K^+$

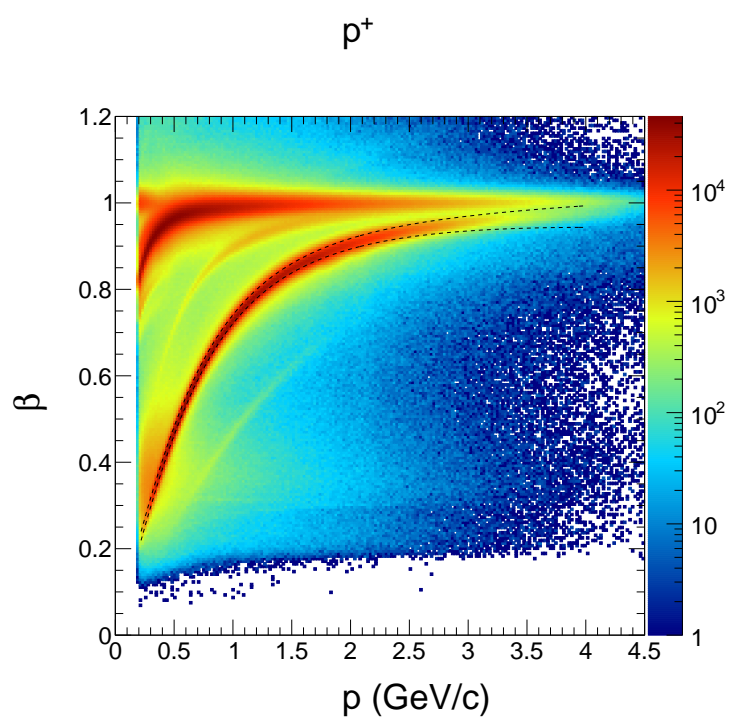


Figure 4.14: Shown above: All positive tracks overlaid with our determination of  $\mu(p) \pm \sigma(p)$  for  $p^+$

$$\mu(p, h) = \mu_{theory} + \Delta\mu \quad (4.11)$$

$$\mu_{theory} = \frac{1}{\sqrt{1 + (m_h/p)^2}} \quad (4.12)$$

$$\Delta\mu = \mu_0 + \mu_1 p + \mu_2 p^2 \quad (4.13)$$

$$\sigma(p, h) = \sigma_0 + \sigma_1 p + \sigma_2 p^2 \quad (4.14)$$

The values are displayed in the table below.

Hadron	Parameter	Sector 1	Sector 2	Sector 3	Sector 4	Sector 5	Sector 6
$K^+$	$\mu_2$	0.00111554	-8.97687e-05	4.78796e-05	0.000376425	-0.00204856	0.000652209
$K^+$	$\mu_1$	-0.00468038	6.19414e-05	-0.00081741	-0.00107931	0.00629181	-0.00264143
$K^+$	$\mu_0$	0.00361012	0.00134921	0.00299674	0.00220194	0.000117821	0.00162582
$K^+$	$\sigma_2$	-0.000331838	-0.00105807	-0.000712404	-0.000573934	-0.000259289	0.000508389
$K^+$	$\sigma_1$	-0.00105857	0.00236686	0.000509169	0.000163467	-0.00233617	-0.00461598
$K^+$	$\sigma_0$	0.0154964	0.0117702	0.0140748	0.0143761	0.0184055	0.0180945
$\pi^+$	$\mu_2$	-0.000962041	-0.000300602	-0.000306326	-3.2245e-05	-0.00226511	-0.000330818
$\pi^+$	$\mu_1$	0.00296349	0.0016512	0.0021962	0.00176045	0.00750862	0.00126443
$\pi^+$	$\mu_0$	-0.00225794	-0.00047045	0.000370406	0.000435526	-0.000449409	-0.00131045
$\pi^+$	$\sigma_2$	-0.000127659	0.000691895	-0.000289961	0.000315041	-0.000936521	-0.000131269
$\pi^+$	$\sigma_1$	-0.000489092	-0.0033948	0.00196853	-0.00197841	0.00212778	-0.000339411
$\pi^+$	$\sigma_0$	0.0155195	0.0167998	0.0124066	0.0157476	0.0145571	0.0141728
$p^+$	$\mu_2$	-0.00039358	-0.000701003	-0.000347651	0.0004854	-0.00121666	0.000563786
$p^+$	$\mu_1$	-0.000295423	0.00170899	0.000794901	-0.000744446	0.00376887	-0.00353545
$p^+$	$\mu_0$	0.00227353	0.00231676	0.00364672	0.00276859	0.00128827	0.00439605
$p^+$	$\sigma_2$	0.001429	0.00144256	0.00124456	0.00190709	0.00141039	0.0011516
$p^+$	$\sigma_1$	-0.0021472	-0.00262226	-0.00196308	-0.00385218	-0.00186708	-0.00186749
$p^+$	$\sigma_0$	0.0107541	0.0109091	0.0104381	0.0115449	0.0109969	0.0107759
$\pi^-$	$\mu_2$	3.28823666e-04	-1.30673670e-05	-2.32502052e-04	-9.75619848e-04	-5.89834444e-04	5.27496718e-04
$\pi^-$	$\mu_1$	-3.94924663e-03	-2.66028661e-03	-1.28565631e-03	9.09410075e-04	-2.01610684e-03	-4.42276918e-03
$\pi^-$	$\mu_0$	9.48011169e-04	1.55078786e-03	1.43431985e-03	1.35056935e-03	4.59833580e-03	2.30751866e-03
$\pi^-$	$\sigma_2$	4.37635504e-04	4.38306224e-04	5.32057510e-04	3.36999845e-04	7.74135462e-04	1.36515196e-04
$\pi^-$	$\sigma_1$	-3.28011836e-03	-3.28456104e-03	-3.82847286e-03	-3.11749323e-03	-4.63110728e-03	-2.21229710e-03
$\pi^-$	$\sigma_0$	1.63296567e-02	1.62229164e-02	1.59769911e-02	1.58803427e-02	1.74670064e-02	1.51753145e-02
$K^-$	$\mu_2$	-2.72020947e-03	-5.21081786e-03	-2.13868763e-02	-4.45600034e-03	-7.60703841e-03	-5.27074813e-03
$K^-$	$\mu_1$	1.78610401e-02	2.30787460e-02	9.49357818e-02	1.95764575e-02	3.63245785e-02	2.92417500e-02
$K^-$	$\mu_0$	-2.26190100e-02	-2.22562379e-02	-1.02704771e-01	-2.25931014e-02	-5.10484618e-02	-3.19918187e-02
$K^-$	$\sigma_2$	1.76905114e-02	1.62989708e-02	3.60928130e-02	1.51270521e-02	1.91308107e-02	2.38470033e-02
$K^-$	$\sigma_1$	-7.74901862e-02	-7.33041628e-02	-1.57454534e-01	-7.26870393e-02	-9.23654247e-02	-1.02397836e-01
$K^-$	$\sigma_0$	1.07082820e-01	1.00573410e-01	1.93148260e-01	1.00993689e-01	1.26963814e-01	1.30057621e-01

Table 4.4: Values used to calculate the mean and resolutions for hadron likelihood based identification.

## Validation of Kaon Identification

A Monte Carlo simulation was used to study particle identification of positive hadrons as a function of the hadronic momentum. As a result of this study the minimum confidence level ( $\alpha = 0.55$ ) and maximum momentum ( $p_{max} = 2.0 \text{ GeV}/c$ ) for  $K^+$  were determined.

To study this SIDIS events were generated using `clasdis`. Our simulation includes  $\pi^+$ ,  $K^+$  and protons (here denoted  $P^+$ ) over a range of kinematics consistent with the E1-F beam energy of  $E_{beam} = 5.498 \text{ GeV}$ . After passing these events through the CLAS detector simulation `GSIM`, reconstruction was used to fit tracks. The truth information for generated kinematics was stored in the output files, and we correlated reconstructed particles to their generated counter-part by requiring that magnitude of the three momentum difference was small ( $\delta P < 0.05$ ).

$$\delta P = \frac{|\vec{P}_{gen} - \vec{P}_{rec}|}{|\vec{P}_{gen}|} \quad (4.15)$$

In this simple equation  $P_{rec}$  and  $P_{gen}$  are the reconstructed and generated three momentum of the track being matched. After this matching procedure has been applied, we calculate two simple metrics, the *purity* and the *efficiency*. The purity refers to the fraction of tracks that are classified as kaons that are truly kaons. More formally it is written,

$$P = \frac{tp}{tp + fp} = \frac{N_{K^+}}{N_{K^+} + N_{\pi^+} + N_{P^+}} \quad (4.16)$$

where  $tp$  and  $fp$  are true positives and false positives respectively, and the variables  $N$  refer to the true number of tracks with that label in the sample. The efficiency is simply the fraction of all true kaons which are identified as kaons, and can be written as shown below.

$$\epsilon = \frac{tp}{tp + fn} = \frac{N_{K^+ \text{ identified}}}{N_{K^+}^{total}} \quad (4.17)$$

As a simple illustrative example, consider the case when all hadrons are called kaons, in this case the efficiency is 1, but the purity will be at its minimum (related to the fraction of total particles that are kaons). As the purity of the sample is increased, the efficiency drops. For this study the efficiency drives our statistical errors, but the purity is the more important metric. As the cut boundaries are restricted by raising the minimum confidence level of hadrons identified as kaons, the purity goes up and the efficiency goes down 4.3.1.

Based on this study, a maximum momentum of 2.0 GeV and a minimum confidence  $\alpha_{min}$  of 0.55 is required for all kaons in our analysis, which provides a purity of 80% or more (depending on the kinematics). The magnitude of the  $\pi^+$  asymmetry is known in these kinematics to be on the order of

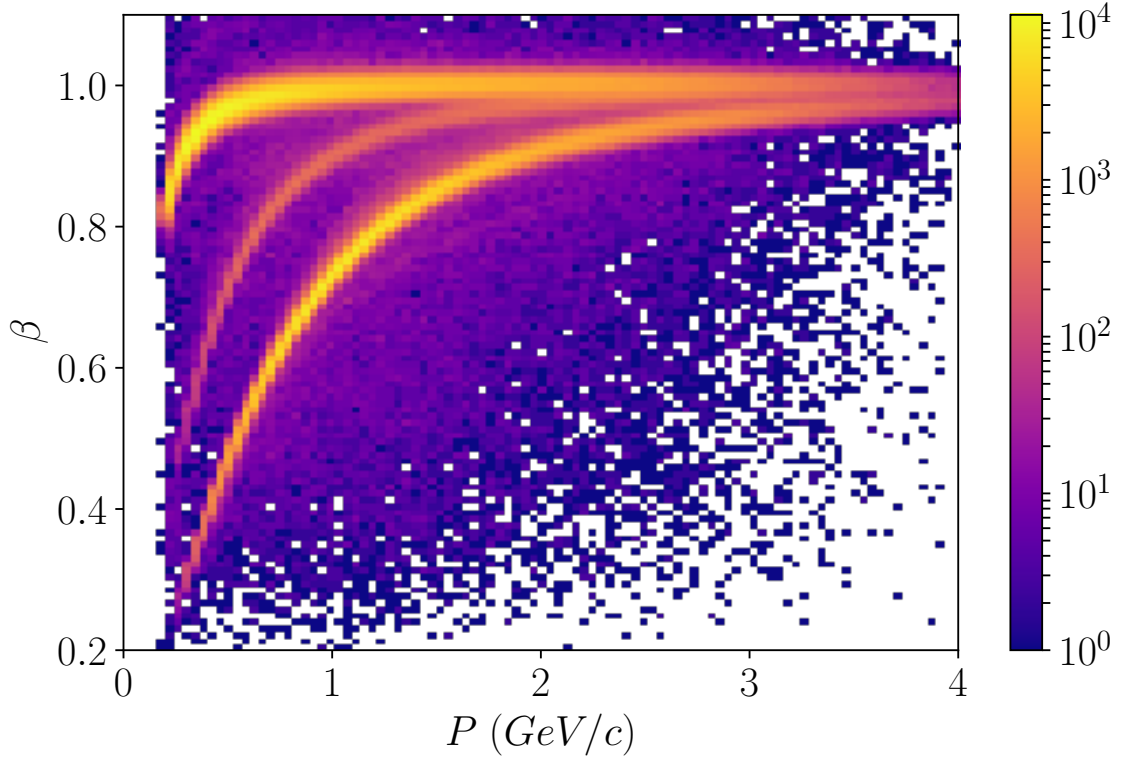


Figure 4.15: Positive hadrons from the Monte Carlo simulation produce a  $\beta$  vs.  $p$  simulation that is very similar to data.

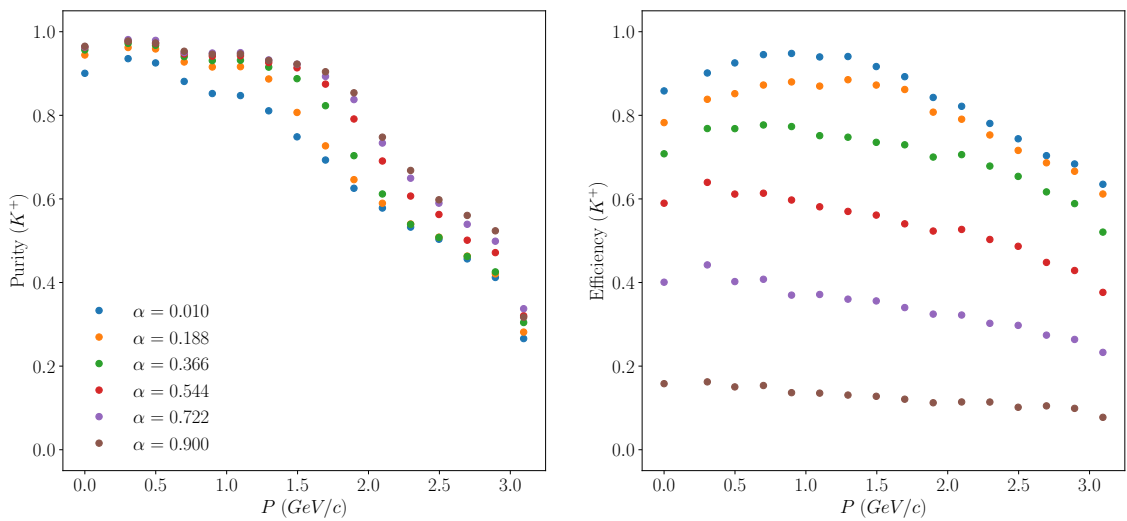


Figure 4.16: The efficiency and purity of our kaon sample are studied by using a Monte Carlo simulation. Here, the results are studied as a function of the confidence level, and of the track momentum.

0.02, if the sample is comprised of 20% pions (which is the worse case in our measurement) then the contribution to the total asymmetry is equivalent to a  $K^+$  asymmetry of 0.005, which is much smaller than our errors. This level of contamination is therefore very tolerable, and should have no significant impact on our analysis.



# Chapter 5

## Beam Spin Asymmetry Analysis

### 5.1 Introduction

Measurement of the beam spin asymmetry is carried out for the positively charged K-meson. As discussed in the introduction, the beam spin asymmetry theoretically depends on  $F_{UU,L}$ ,  $F_{UU,T}$ ,  $F_{UU}^{\cos\phi}$ ,  $F_{UU}^{\cos 2\phi}$ , and  $F_{LU}^{\sin\phi}$ . By dividing the electron-kaon events into several bins, beam spin asymmetry measurements are taken at different average values of the kinematic variables  $x$ ,  $Q^2$ ,  $z_h$ , and  $P_T$ . Finally, the structure function ratios  $A_{LU}^{\sin\phi}$ ,  $A_{UU}^{\cos\phi}$ , and  $A_{UU}^{\cos 2\phi}$  are extracted from each bin. In this chapter a discussion is provided of SIDIS event selection, the binning used in this analysis, measurement values with associated systematic uncertainties, and the extraction of structure function ratios using the  $\phi_h$  dependence in each kinematic bin.

### 5.2 Event Selection and Binning

#### Event Selection

After particle identification, events which have a trigger electron and a positive kaon are kept for analysis. Events are discarded that do not have  $W > 2 \text{ GeV}/c^2$  and  $Q^2 > 1 \text{ GeV}^2/c^2$ , because they are not considered part of the deeply inelastic region. Additionally, to avoid exclusive resonances in the  $ep \rightarrow eK^+X$  spectrum, a minimum value is imposed on the missing mass of the final state  $M_X$  ( $ep \rightarrow eK^+X$ ). Here, we use  $M_X(ep \rightarrow eK^+X) > 1.25 \text{ GeV}/c^2$ . Finally, a cut is applied to exclude low values of  $z$  to constrain our kinematics to the current factorization region where TMD factorization has been demonstrated at leading order. It is additionally required that  $z < 0.75$  to avoid exclusive events. This restriction on  $z$  is applied when  $z$  is integrated over (for the axes  $x$ ,  $Q^2$ , and  $P_T$ ) but not to the  $z$  axis itself, where we measure the asymmetry across the entire experimentally observed kinematic range.

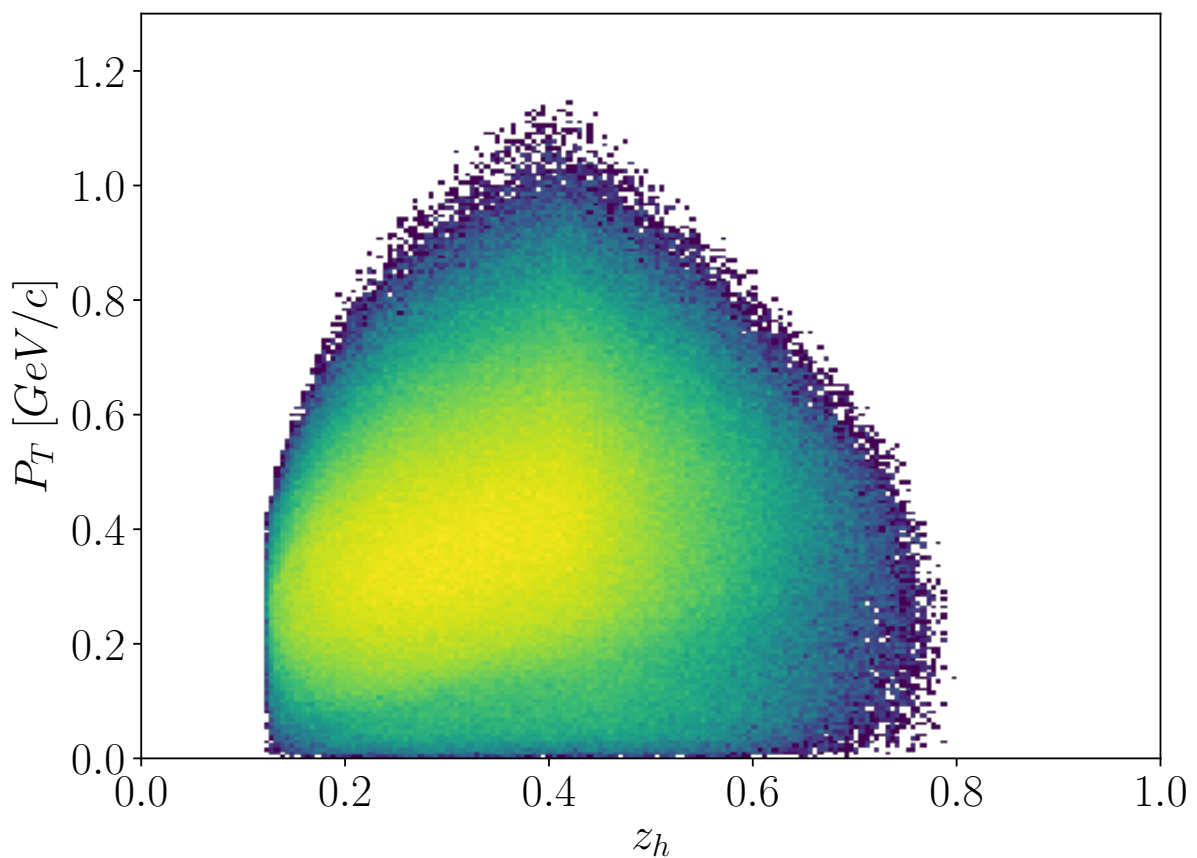


Figure 5.1: Correlation between  $z$  and  $P_T^2$  ( $GeV^2/c^2$ ) for each event in our analysis sample.

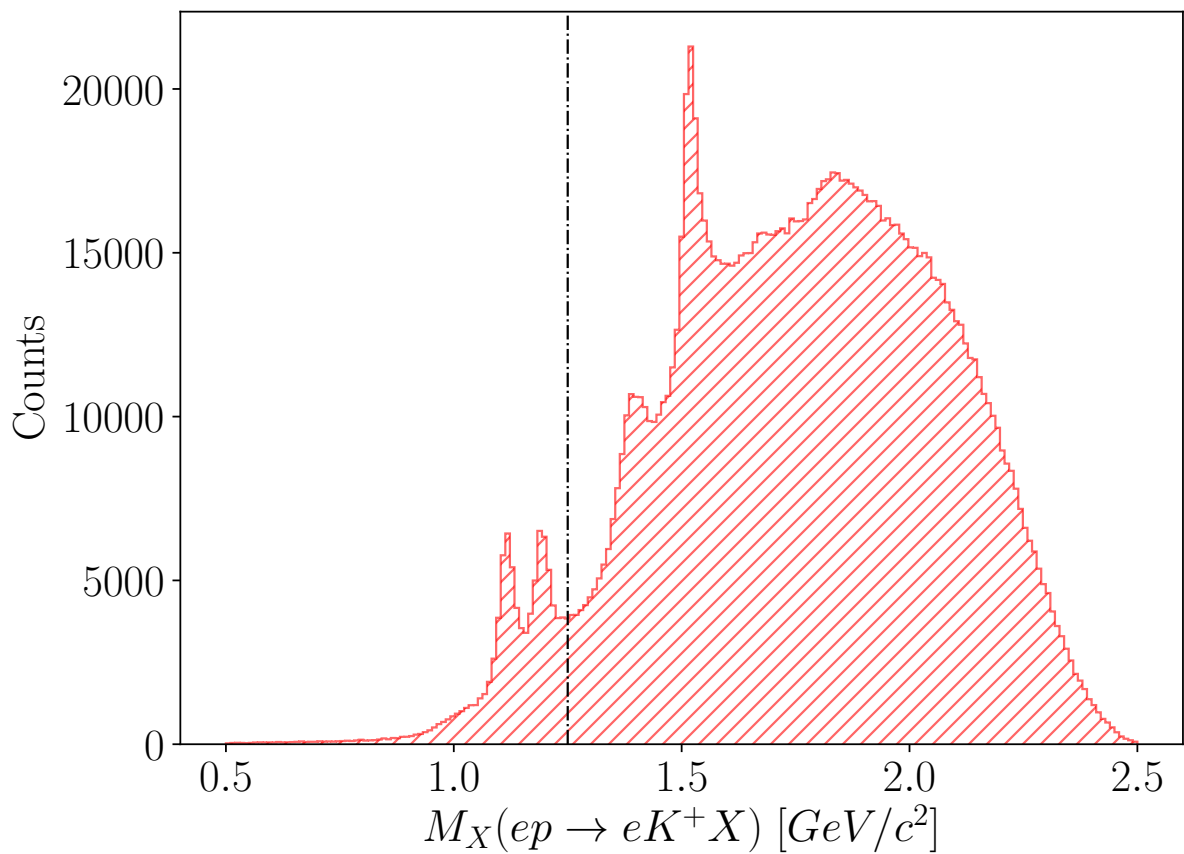


Figure 5.2: The missing mass spectrum for the reaction  $ep \rightarrow e'K^+X$  is shown after the application of all cuts used in the analyses except for the cut we apply on the missing mass.

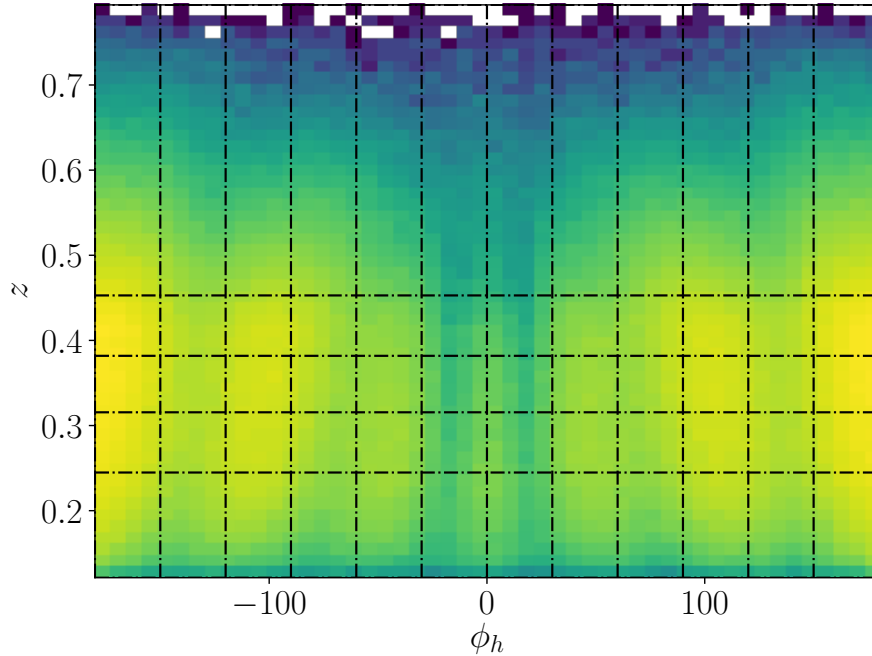


Figure 5.3: Bins used for this analysis are displayed in two dimensions for the  $z$  axis.

### Binning

The beam spin asymmetry measurement is performed for the kinematic variables  $x$ ,  $Q^2$ ,  $z$ , and  $P_T$ . For each variable 5 bins are chosen, as well as 12 bins in  $\phi$  for a total of 60 analysis bins.

Bins were chosen using a simple method to ensure equal statistics in each kinematic variable bin (the phi bins do not have equal statistics). The procedure is described using the axis  $x$  as an example. First, all events are sorted by their  $x$  value from smallest to largest. Then, the smallest and largest values are recorded, which are  $x_1$  and  $x_N$  if there are  $N$  events in the sample. Next, the target number of bins  $M$  is chosen (this choice depends on each analysis). Finally, the limits of each bin can be chosen by calculating the number of events per bin  $N/M$  and then using the value of  $x$  which corresponds to multiples of  $N/M$  in the sample.

$$\vec{b} = (x_1, x_{N/M}, x_{2N/M}, \dots, x_N) \quad (5.1)$$

Here, the symbol  $\vec{b}$  denotes a vector of  $(M+1)$   $x$  values which represent bin limits. The binning in  $\phi$  is chosen to be regularly spaced between -180 and 180 degrees.

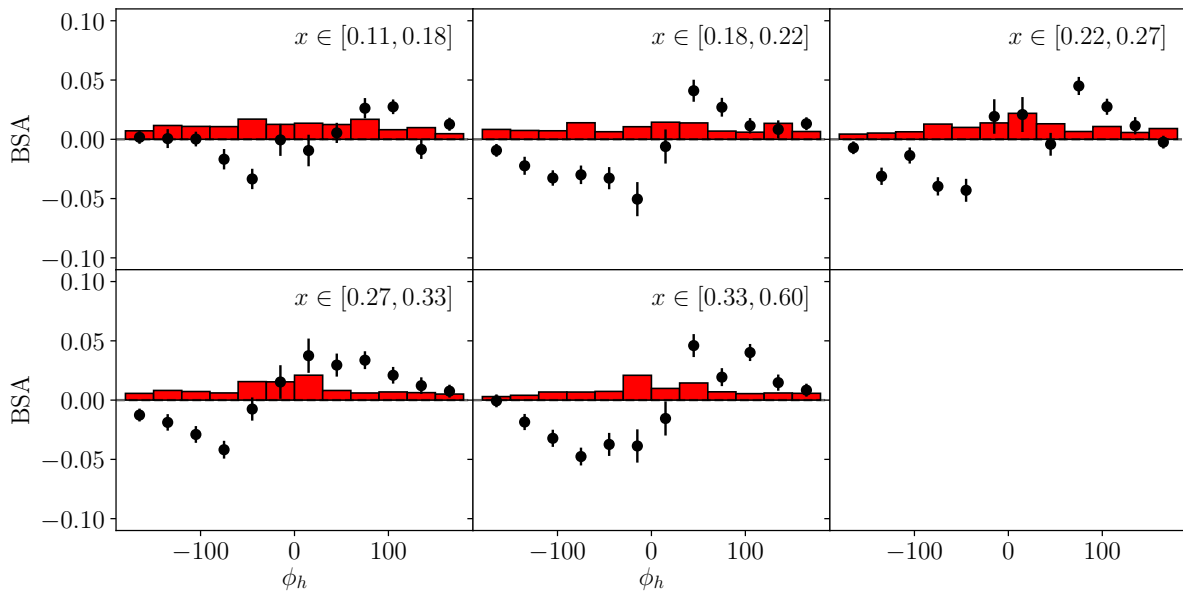
### 5.3 Measured $\phi_h$ Distributions

#### Measured Asymmetry Values

In each bin  $i$  the beam spin asymmetry (here  $A_i$ ) is calculated according to,

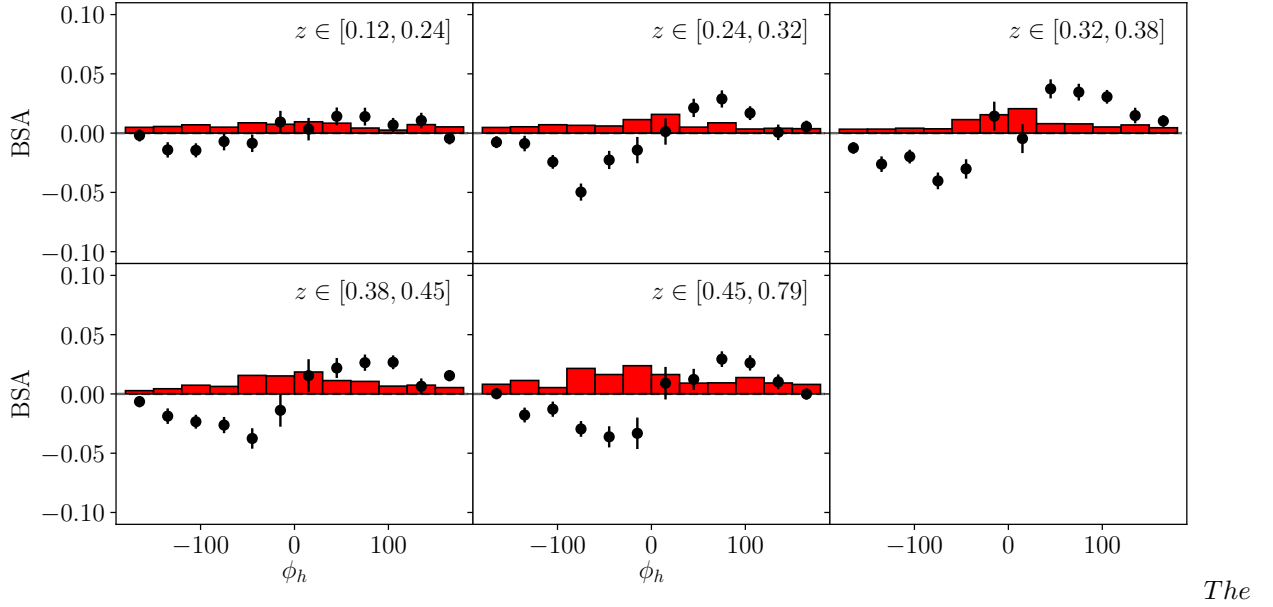
$$A_i = \frac{1}{P_e} \frac{n_+^i - n_-^i}{n_+^i + n_-^i} \quad (5.2)$$

where  $P_e$  is the average beam polarization over the dataset (74.9%). The symbols  $n_\pm^i$  refer to the number of events counted in bin  $i$  with helicity  $\pm$ .



The

$\phi_h$  dependence is shown for each bin of  $x$ , increasing in value from the top left to the bottom right. The statistical uncertainty is shown as black error bars on each point. The total systematic uncertainty is shown as a red bar centered at zero. (5.3)



$\phi_h$  dependence is shown for each bin of  $z$ , increasing in value from the top left to the bottom right. The statistical uncertainty is shown as black error bars on each point. The total systematic uncertainty is shown as a red bar centered at zero. (5.4)

## Statistical Uncertainties

The uncertainty on the measured value of  $A_i$  can be attributed to statistical uncertainty on the counts  $n_i^\pm$ , and the uncertainty associated with the measurement of  $P_e$ . The statistical uncertainty reported on the measurement includes the contribution from counts, but not from the uncertainty in  $P_e$  which is included in the systematic errors. In general, the uncertainty in a measured observable  $\mathcal{O}$  depends on the uncertainty of the parameters (here denoted by  $\vec{\theta}$ ) used in the analysis in the following way (see appendix for derivation).

$$\sigma_{\mathcal{O}}^2 = \sum_{i=1}^N \sum_{j=1}^N \frac{\partial \mathcal{O}}{\partial \theta_i} \frac{\partial \mathcal{O}}{\partial \theta_j} \rho_{ij} \sigma_i \sigma_j \quad (5.5)$$

For the beam spin asymmetry in the  $i^{th}$  bin  $A_i$  one finds that without correlations ( $\rho_{ij} = \delta_{ij}$ ) the error propagation proceeds as shown below.

$$\sigma_A^2 = \frac{A^2}{P_e^2} \sigma_{P_e}^2 + \frac{4(n_-^2 \sigma_+^2 + n_+^2 \sigma_-^2)}{P_e^2 (n_+ + n_-)^4} \quad (5.6)$$

The first term which is the contribution from the variance in the measurements of beam polarization

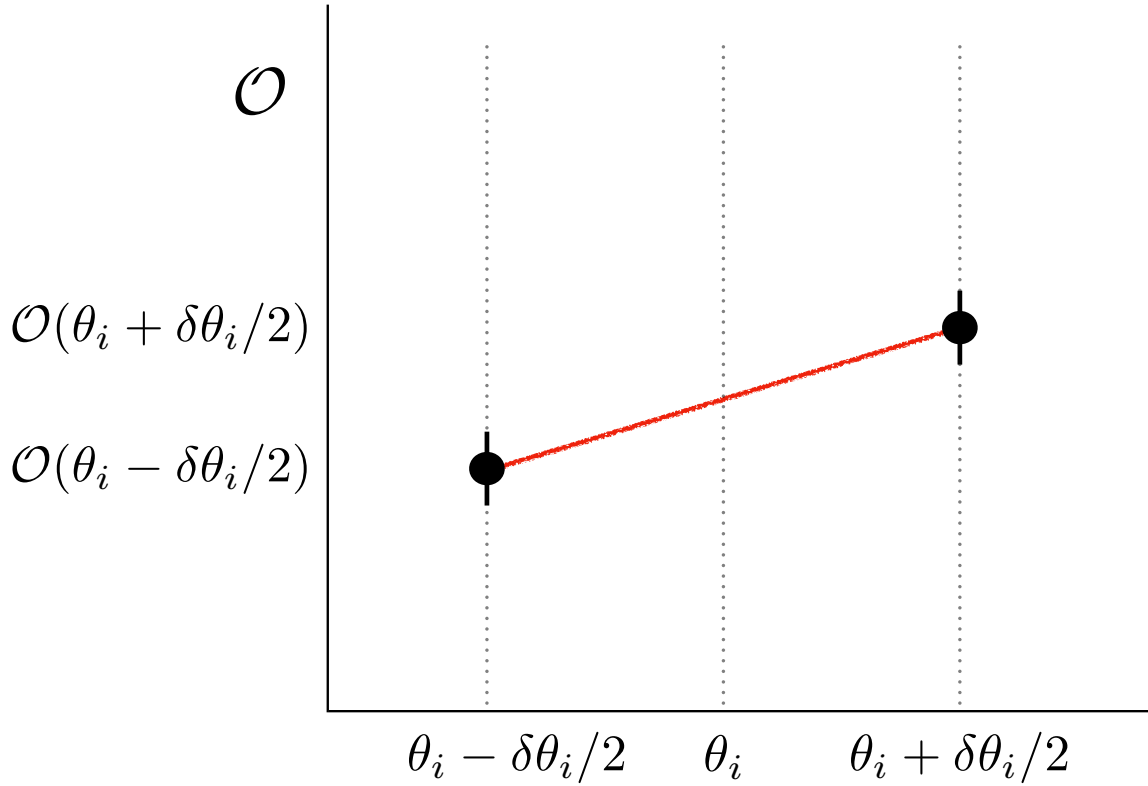


Figure 5.4: The analysis is run for variations in the input parameters  $\theta_i$  to calculate the dependence of the result  $\mathcal{O}$  on each parameter, as described in this section.

will be included as a systematic error. The second term is used as the statistical error bars shown through the analysis. The counts  $n_{\pm}^i$  for the  $i^{th}$  bin are assumed to be Poisson in nature, and therefore have a variance equal to the expected number of counts  $\sigma_{\pm}^2 = n_{\pm}^i$ . With this expression for the statistical uncertainty on the counts, and dropping the beam polarization term for now, the expression becomes:

$$\sigma_A^2 = \frac{4n_+n_-}{P_e^2(n_+ + n_-)^3} \quad (5.7)$$

## Systematic Uncertainties

### Basic Formalism

Systematic effects are shifts or biases in the measured result of some observable as a result of the procedure used in the measurement. Systematic effects can typically be identified and corrected for, or removed all together from the measurement. In the cases where an effect cannot be completely removed, the degree to which the correction for the effect is uncertain is included in the result of the measurement as a systematic uncertainty [? ].

Systematic uncertainties are included using the standard equation for error propagation. In some cases it is possible to analytically find the derivatives needed to calculate the dependence of the observable on a source of systematic uncertainty. This is the case for effect of the variance of the beam polarization on the beam spin asymmetry observable. However in many cases, it is not possible to analytically calculate the effect of an analysis parameter  $\theta_i$  on the observable  $\mathcal{O}$ . Since the observable is usually calculated using some computational chain which starts with the input parameters  $\vec{\theta}$ , it is possible to find the dependence of the observable  $\mathcal{O}$  on the inputs numerically.

$$\frac{\partial \mathcal{O}}{\partial \theta_i} \approx \frac{\mathcal{O}(\theta_i + \sigma_{\theta_i}/2) - \mathcal{O}(\theta_i - \sigma_{\theta_i}/2)}{\sigma_{\theta_i}} \quad (5.8)$$

After inserting the above into equation 5.5 one finds,

$$\sigma_{\mathcal{O}}^2 = \sum_{i=1}^n \sum_{j=1}^n \rho_{ij} (\mathcal{O}(\theta_i + \sigma_{\theta_i}/2) - \mathcal{O}(\theta_i - \sigma_{\theta_i}/2)) (\mathcal{O}(\theta_j + \sigma_{\theta_j}/2) - \mathcal{O}(\theta_j - \sigma_{\theta_j}/2)) \quad (5.9)$$

where  $\rho_{ij}$  is the correlation  $V_{ij}/\sigma_i \sigma_j$ . In most cases, these correlations are assumed to be zero. In some cases, when the parameters  $\theta_i, \theta_j$  come from a fit one may have a correlation provided by the covariance matrix and it should be used. In the case where correlations are assumed to be zero, the total systematic uncertainty is simply the quadratic sum of the shifts in the observable within the uncertainty window on each parameter.

$$\sigma_{\mathcal{O}}^2 = \sum_{i=1}^n \left[ \mathcal{O}(\theta_i + \sigma_{\theta_i}/2) - \mathcal{O}(\theta_i - \sigma_{\theta_i}/2) \right]^2 \quad (5.10)$$

## Sources of Systematic Uncertainty

Systematic uncertainties are calculated using the techniques described above for both the  $\phi_h$  dependent asymmetry measurement as well as the results of the parameter estimation for each kinematic bin. The systematic errors on the phi dependent asymmetry bins is not used in the parameter estimation for the structure function ratios  $A$ . Table 5.1 below summarizes the sources of systematic uncertainty considered in this analysis.

Except for the beam polarization and the momentum of the kaon track, all parameters listed in the table are treated using the formalism outlined above. The beam polarization uncertainty quoted at 2.4% contains contributions from the standard deviation of the Moller polarimetry measurements (0.2%), residual target polarization effects (1.4%), and atomic motion/finite acceptance corrections (0.8%).

Source	Variation
Beam polarization	0.024
DC Region 1 Fid.	1 (cm)
DC Region 3 Fid.	3 (cm)
EC-W	12 (cm)
EC-V	12 (cm)
EC-U	12 (cm)
Kaon Confidence ( $\alpha$ )	0.5-0.6
$\theta_{cc}$ Matching	$\sigma$
EC Energy Deposition	0.01 (GeV)
$p_{K^+}$	1.9-2.1
EC Sampling Fraction	$0.5\sigma$
Z-Vertex	0.5 (cm)
Vertex diff.	1 (cm)

Table 5.1: Different sources of systematic effect considered in this analysis. The magnitude of the effect is shown here averaged over all bins of  $\phi_h$ .

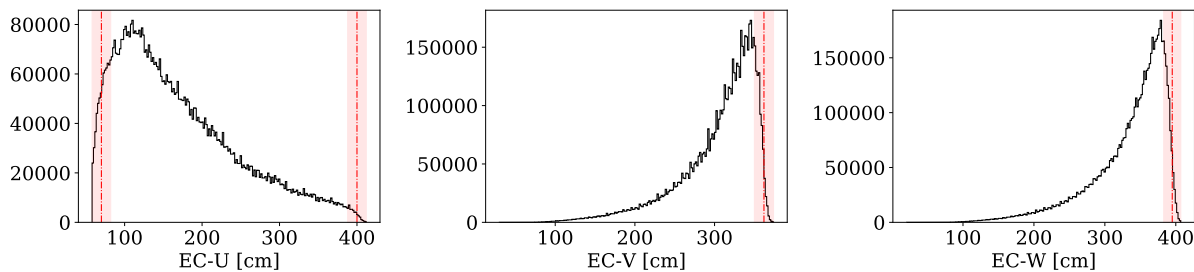


Figure 5.5: Boundaries and associated uncertainties for the *EC* coordinate cuts.

### Electromagnetic Calorimeter Fiducial Cuts

The electron identification cuts used on ECAL are varied in order to estimate the dependence of the asymmetry on these parameters. These boundaries (which are sometimes excluded from systematic uncertainties) produce some of the largest changes in our analysis, associated with the large deviation of the distributions around the cut 5.3. The shift in the measured beam spin asymmetry is large particularly for low  $x$ , low  $Q^2$ , low  $P_T$  and high  $z$ . These shifts likely arise from the reduction of statistics in the low angle region ( $x$  is correlated with *ECU* with coefficient 0.49,  $Q^2$  is correlated with *ECU* with coefficient 0.8).

### Missing Mass

To investigate the effect of varying our missing mass cut on the analysis we shift it left and right by 50 MeV, which produces little to no effect. This is demonstrated in the figures 5.3 5.3 5.3.

### Confidence Level

The minimum acceptable confidence level is varied between 0.5 at the loosest and 0.6 at the tightest. For the  $x$ ,  $Q^2$ , and  $P_T$  axes the observed shift is roughly constant regardless of the kinematic bin.

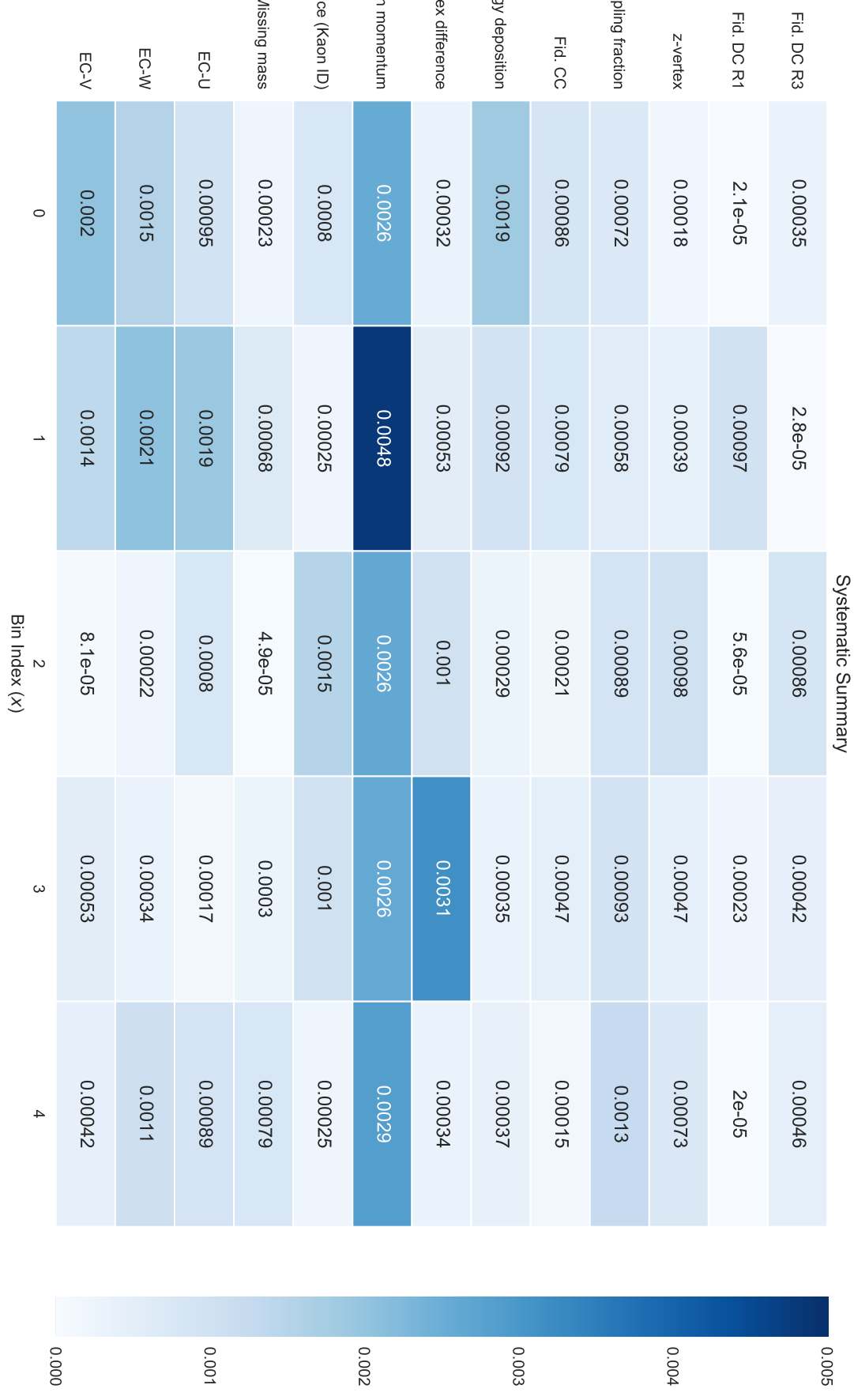


Figure 5.6: The magnitude of each systematic error source considered is shown above in a heat-map for the  $x$  axis. The vertical scale maximum corresponds to half of a percent.

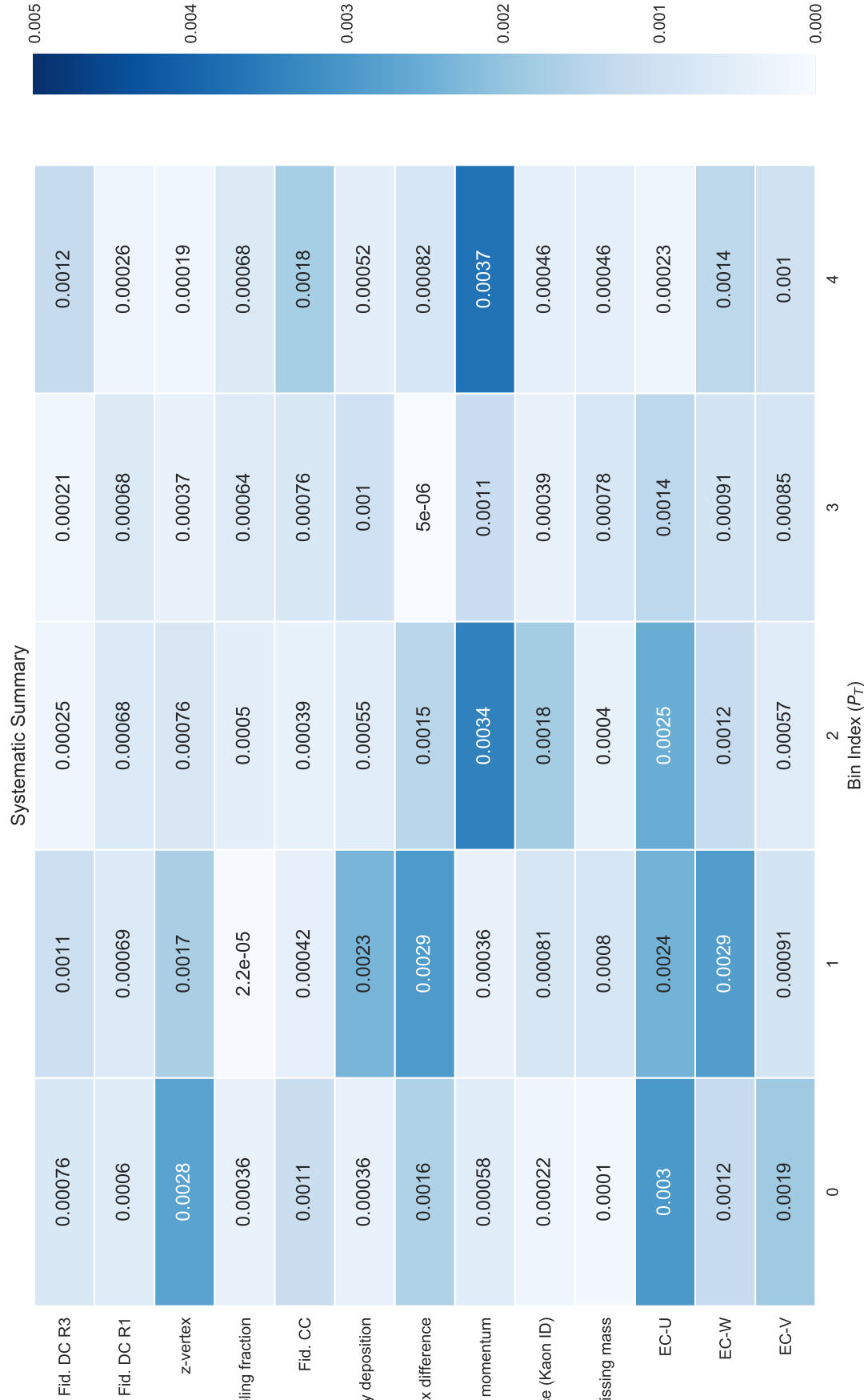


Figure 5.7: The magnitude of each systematic error source considered is shown above in a heat-map for the  $P_T$  axis. The vertical scale maximum corresponds to half of a percent.

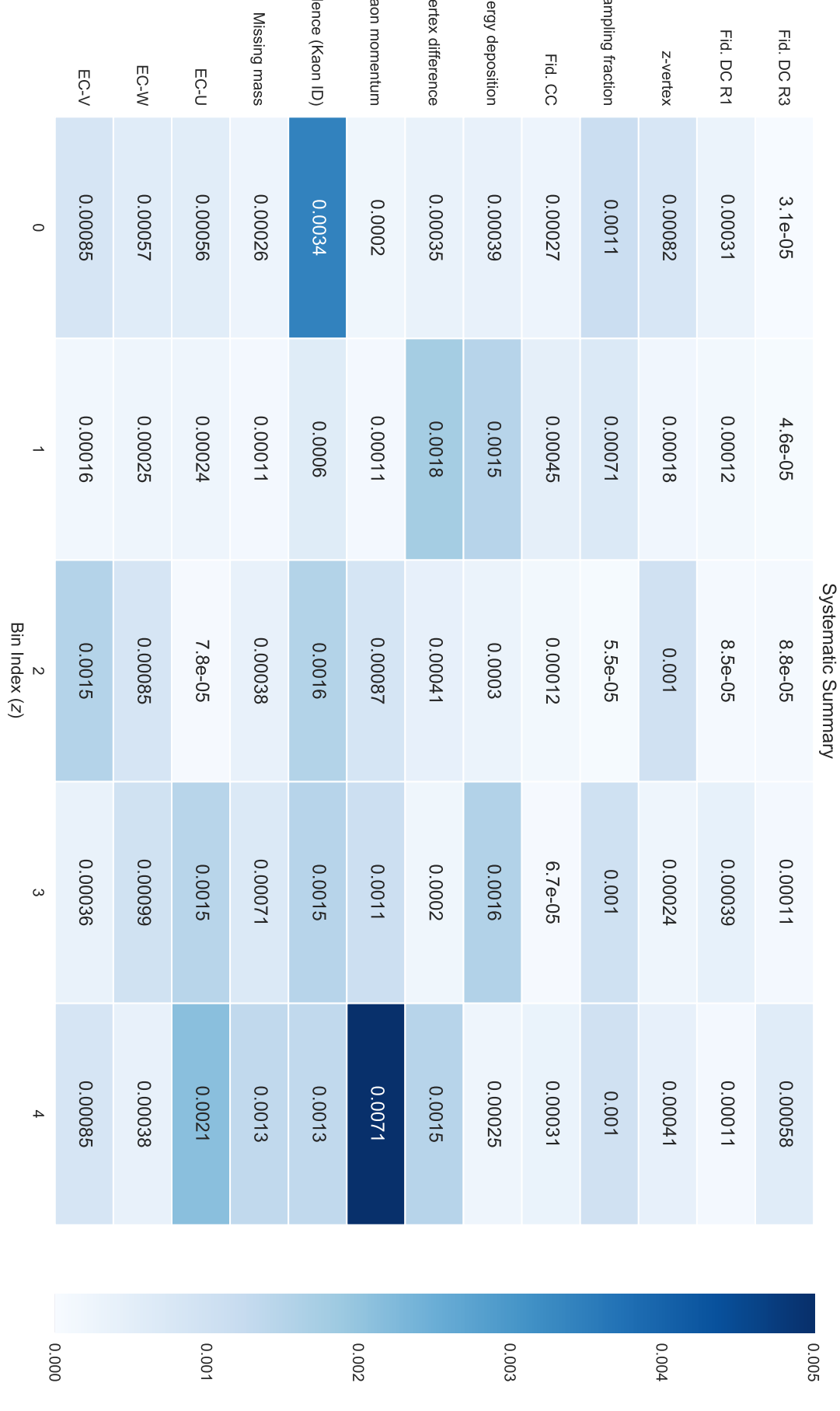


Figure 5.8: The magnitude of each systematic error source considered is shown above in a heat-map for the  $z$  axis. The vertical scale maximum corresponds to half of a percent.

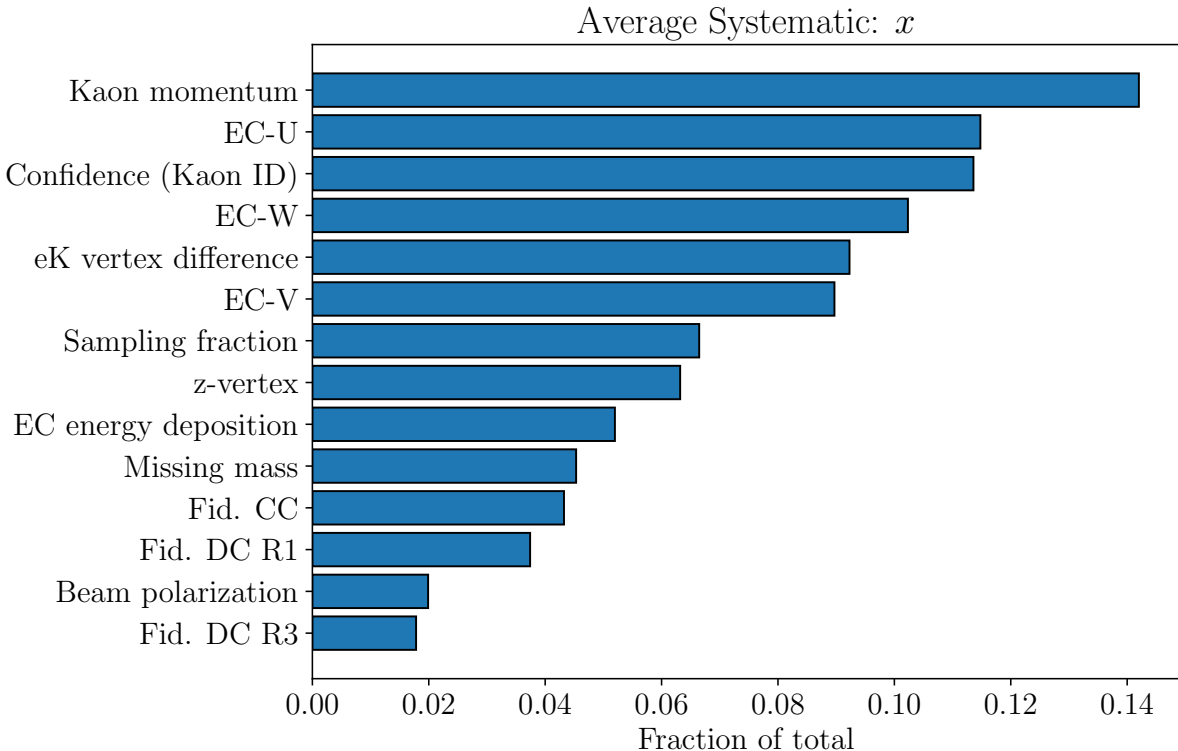


Figure 5.9: The relative contribution of each systematic uncertainty to the total is shown above averaged over the bins of the  $x$  axis.

### Kaon Momentum

Monte Carlo analysis of kaon identification purity and efficiency was used to establish a maximum acceptable momentum for kaons included in our analysis. In order to study the impact of that value (2.0), the value is varied by 100 MeV and the result is included as a systematic error.

### Electromagnetic Calorimeter Energy Cuts

The momentum dependent sampling fraction cut, as well as the energy deposition cut placed on the inner electromagnetic calorimeter do not contribute much to the total systematic uncertainty. In this study, the variation of the energy deposited cut by 10 MeV did not have a strong impact on the result. Additionally, the observed shift was mostly constant over the kinematic variables. The same is true for the sampling fraction cut.

### Fiducial Cuts on DC and CC

The variation of our fiducial cuts on the drift chambers regions 1 and 3, as well as the Cherenkov counter produced no major shift in our measured asymmetries. This reflects the redundancy of using several fiducial cuts.

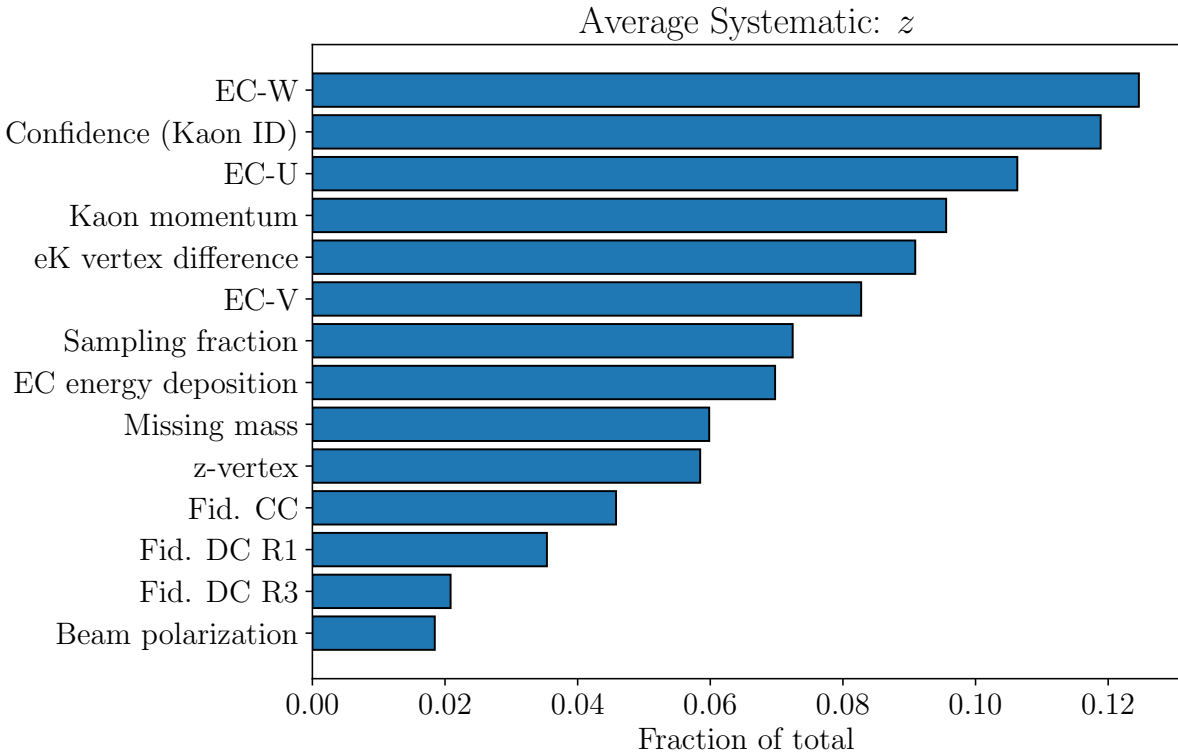
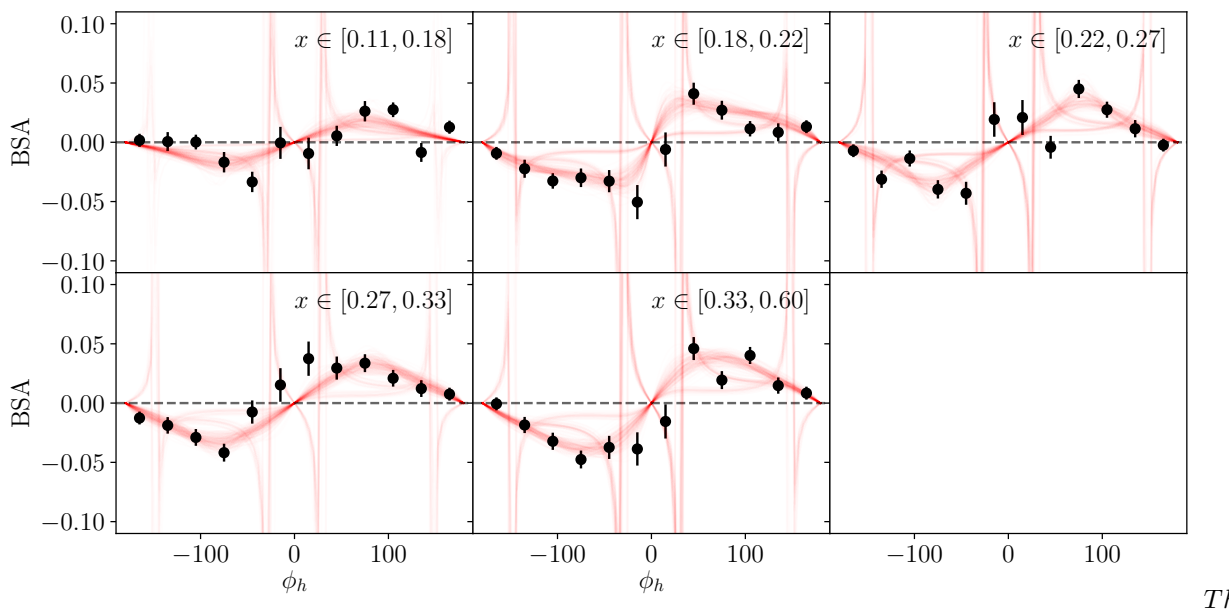


Figure 5.10: The relative contribution of each systematic uncertainty to the total is shown above averaged over the bins of the  $z$  axis.

### Vertex Cuts

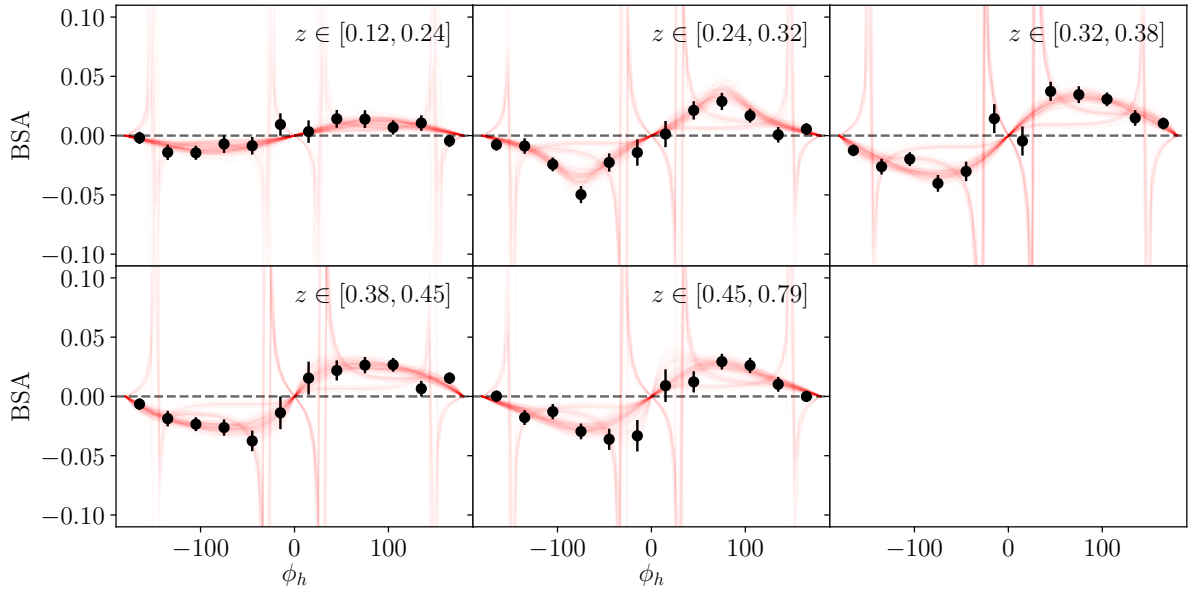
The vertex cut position was varied by  $\pm 0.5$  ( $cm$ ) and small changes were observed in the extracted beam spin asymmetries. Additionally, no kinematic dependence was observed in the shifts.

## 5.4 Extraction of Modulations



The

$\phi_h$  dependence is shown for each bin of  $x$ , increasing in value from the top left to the bottom right. The statistical uncertainty is shown as black error bars on each point. Fits to 256 replicas have been superimposed on the figure. (5.11)



The

$\phi_h$  dependence is shown for each bin of  $z$ , increasing in value from the top left to the bottom right. The statistical uncertainty is shown as black error bars on each point. Fits to 256 replicas have been superimposed on the figure. (5.12)

The motivation to measure the beam spin asymmetry in several kinematic bins as well as bins of  $\phi_h$  is to perform an estimate of the value of structure functions at the kinematic points (more precisely the average value of the structure functions over the range of values included in a point). To do this, the authors perform parameter estimation on the  $\phi_h$  distributions taking as a model the theoretical dependence of the beam spin asymmetry on  $\phi_h$ .

$$f(\phi_h, \vec{a}) = \frac{a_0 \sin \phi_h}{1 + a_1 \cos \phi_h + a_2 \cos(2\phi_h)} \quad (5.13)$$

The parameters  $\vec{a}$  are the structure function ratios to be extracted. The simplest way to extract these parameters is to use  $\chi^2$  minimization implemented in a standard fitting package. In these approaches,  $\chi^2$  is defined as the square difference between the observed data values and those predicted by the model, normalized by the error. If the fluctuation between the data and theory predictions is on the

order of the error, the  $\chi^2$  is simply on the order of the number of data points. The parameters  $\vec{a}$  which best describe the data are those which make the  $\chi^2(\vec{a})$  assume its minimum value. This minimization is done in practice with gradient descent or quasi-Newton's method based algorithms like those provided in `Minuit` or `scipy.optimize.minimize`, the details of such algorithms will not be discussed here. It is sufficient to say that these minimization methods produce the parameters  $\vec{a}$ , and an estimate of the covariance matrix  $V$ . The parameters and their errors become the extracted value and uncertainty of the structure function ratio in each bin.

Unfortunately, applying the standard single-fit procedure described above does not always produce stable results. In some cases, the resulting parameter sets are reasonable, in other cases however the parameters in the denominator become nonphysically large and oppose each other. This effect has motivated previous analysts to search for other means of extracting the dominant  $\sin \phi_h$  behavior from the distributions. One common technique is to assume that the coefficients  $a_1$  and  $a_2$  of above are small compared to 1. The analyst can then fit the  $\phi_h$  distribution with just one linear parameter  $a_0$ . This produces a stable result, but has the disadvantage that one needs to introduce a systematic uncertainty associated with the difference observed between using the full model (with a restricted range for the parameters in the denominator) and the results obtained using the single parameter model. Additionally, the structure function decomposition of the SIDIS cross section relies on theoretically solid ground, therefore it should be used in its full form. If the data contain little information regarding the structure function ratios in the denominator, the authors believe it more valuable to demonstrate this by extracting those parameters with (large) errors, rather than ignore their contribution. In order to accomplish this, the method of replicas (or parametric bootstrapping) is used to perform the parameter estimation. The replica method consists of generating  $N_{rep}$  pseudo-data  $\phi_h$  distributions which have a normal distribution located at the observed value, and with a variance equal to the statistical errors on the associated data point.

$$\vec{A}_{rep} = \mathcal{N}(\vec{A}, \sigma_A) \quad (5.14)$$

Here  $\vec{A}$  is a vector of length  $n_{phi}$  bins, representing the measured beam spin asymmetry for each value of  $\phi_h$  in a given kinematic bin. Each of these distributions is fit with the full model, and the resulting parameter values are saved. The final reported value for each fit parameter, as well as its uncertainty can be reported as the mean, and standard deviation of the fit results. This procedure which is similar to bootstrapping, can be seen as an attempt to fit the underlying distribution that generated the data while avoiding the statistical noise. This technique has been discussed in [? ].

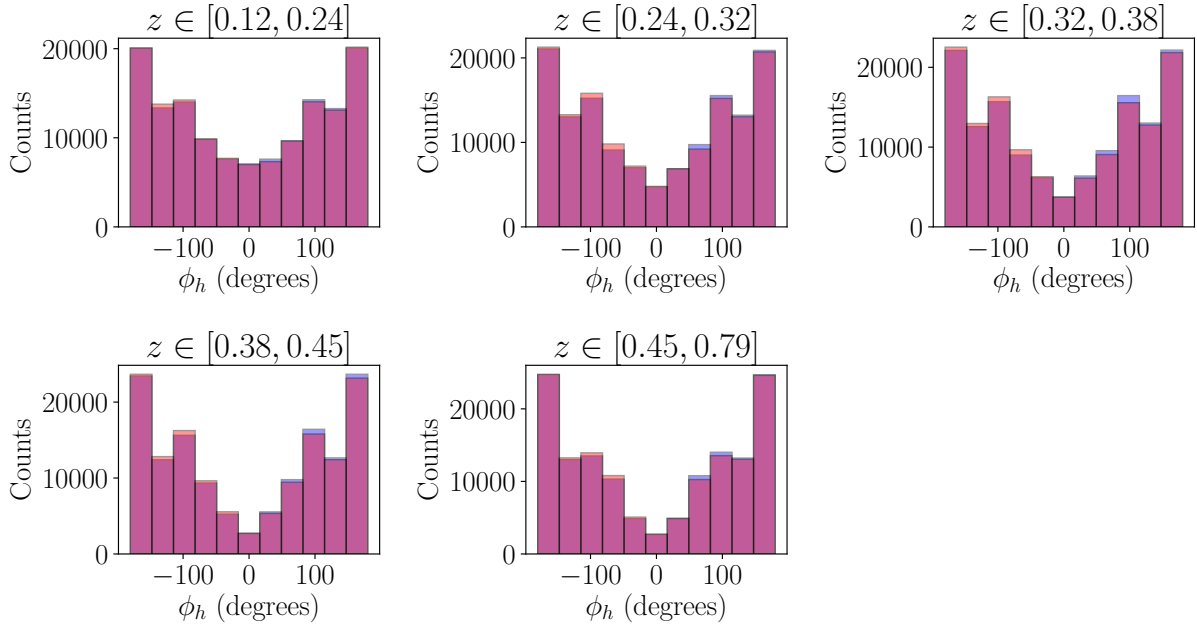


Figure 5.11: Counts for different helicity states are superimposed for different bins of  $z$ .

$$\langle a_j \rangle = \frac{1}{N_{rep}} \sum_{i=1}^{N_{rep}} a_j^{(i)} \quad (5.15)$$

$$\sigma_{a_j}^2 = \frac{1}{N_{rep}-1} \sum_{i=1}^{N_{rep}} (a_j^{(i)} - \langle a_j \rangle)^2 \quad (5.16)$$

## Results

As is the case for positive pions, the observed structure function ratio  $A_{LU}^{\sin \phi}$  is positive for all kinematic points that were measured. In general, this extraction reveals that the  $\sin \phi_h$  moment has a magnitude around 3% for most kinematic points, and depends weakly on the kinematic variables used in this analysis. The relative asymmetry value to total error ratio is around 1.5% for most measured points.

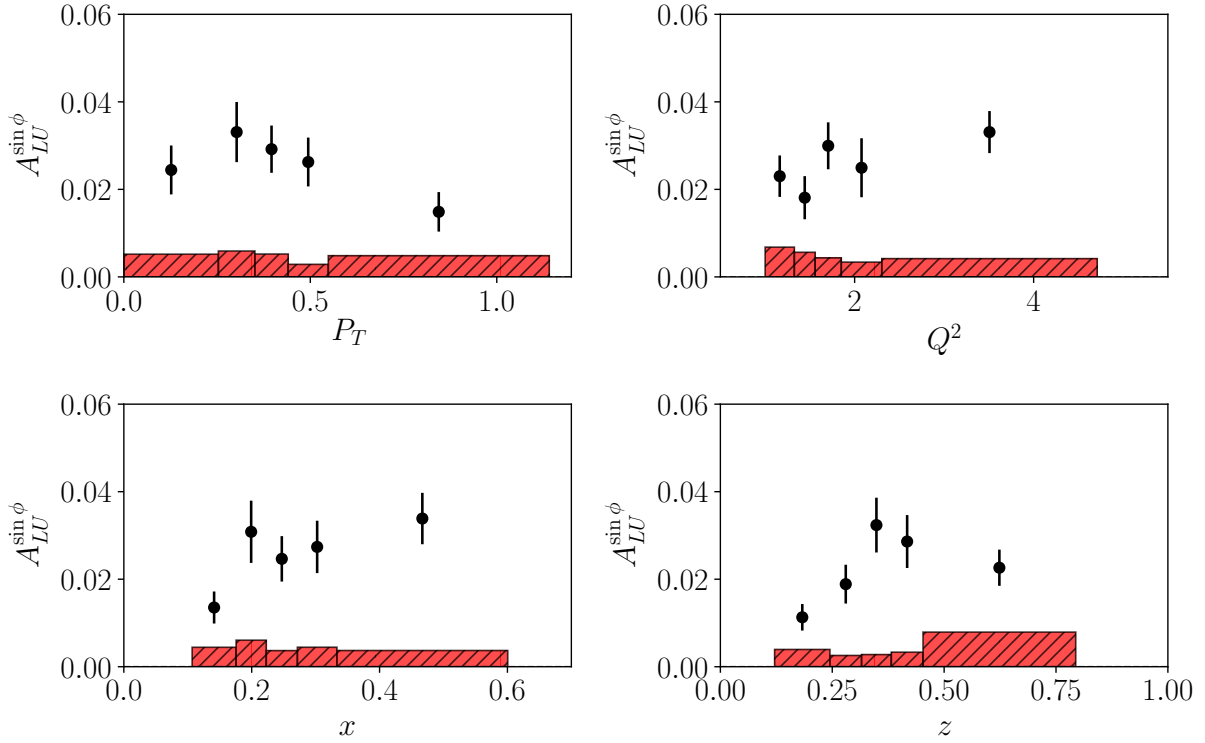


Figure 5.12: Our extraction of  $A_{LU}^{\sin \phi}$  for the kinematic bins described above. The black error bars represent uncertainty in the extraction of the parameter value. Red error bars are systematic uncertainties.

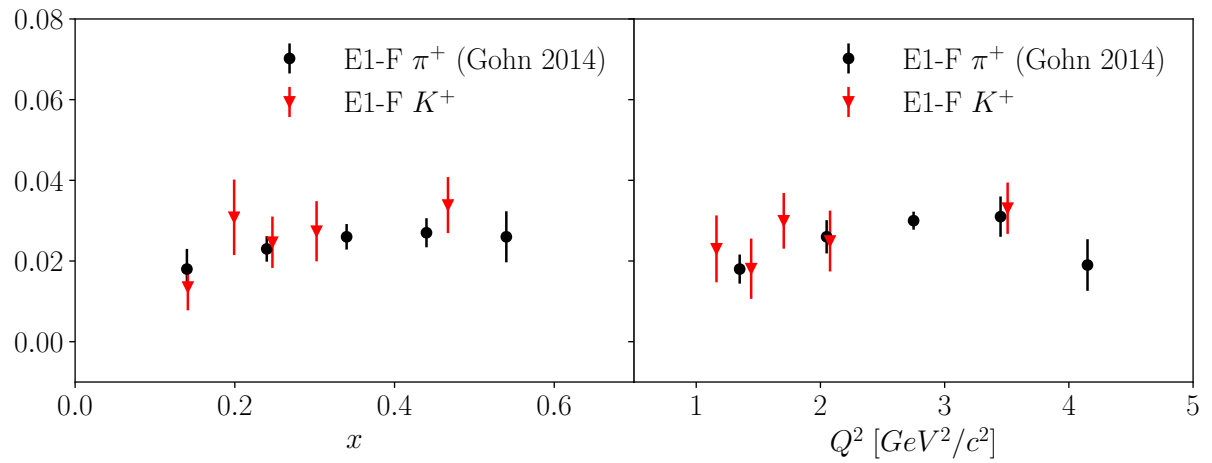


Figure 5.13: In this figure the results of this study for positively charged kaons are compared with previous results from the same dataset produced by [? ] for positively charged pions. This figure shows the  $x$  and  $Q^2$  dependence of  $A_{LU}^{\sin \phi_h}$ .

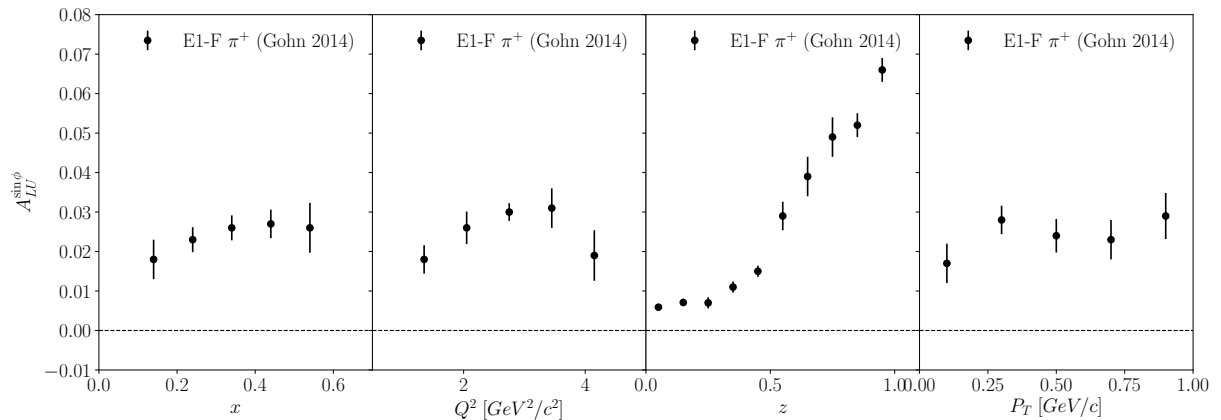


Figure 5.14: In this figure the results of this study for positively charged kaons are compared with previous results from the same dataset produced by [? ] for positively charged pions. This figure shows the  $z$  and  $P_T$  dependence of  $A_{LU}^{\sin \phi_h}$ .



# Chapter 6

## Inclusive Cross Section

One of the primary goals of this thesis work is the accurate determination of cross sections for charged  $\pi$  mesons in SIDIS. The measurement of a cross section for a well known process such as elastic scattering or inclusive electron scattering is typically calculated (using the same data) before new cross sections are provided. Not only does this procedure provide validation of the integrated luminosity factor, it also builds confidence that the overall quality of the dataset is high, the electron identification is accurate, and the list of files used in the analysis is reasonable. In this chapter, the inclusive electron scattering cross section is discussed. First, a short discussion is provided that describes what inclusive scattering is in this study. A discussion is then provided about the model that is used in both MC simulation and as a metric to compare the results with. The majority of this chapter that follows is devoted to the description of event selection, binning, acceptance corrections, bin center corrections, and radiative corrections. Finally, the results are discussed and compared to the model.

### 6.1 Motivation

Inclusive electron scattering is the process  $ep \rightarrow eX$ , where only the final state electron is detected and the rest of the event is not (anything apart from the electron that is detected is not analyzed). As a function of  $W$  (the invariant mass of the final state ( $\gamma^* + p$ ) system) the region below 2 GeV contains resonances and is often referred to as the resonance region. Resonance structures are difficult to detect higher than about 2 GeV, and this region is typically called the *deeply inelastic* region. While the deeply inelastic region is used extensively for measurements in nuclear/particle physics, the goal of luminosity verification is more easily achieved in the resonance region. This fact is due principally to the excess of Bethe-Heitler events which collect in the  $2 < W < 3$  region for  $E_{beam} = 5.498$  (such events are difficult to remove when detecting only the final state electron).

Measurement of the inclusive cross section is performed for each sector independently by counting reconstructed events  $N_i$  in each bin  $i$  of the phase space of  $W$  and  $Q^2$ . Experimentally the cross section for bin  $i$  is,

$$\frac{d\sigma_i}{dW \, dQ^2} = \frac{N_i}{\mathcal{L} A_i B_i R_i} \frac{1}{\Delta W \, \Delta Q^2} \quad (6.1)$$

where the factor  $\mathcal{L}$  is the integrated luminosity for the time period over which the events  $N$  were collected (the subscript  $i$  indicates the bin, but is omitted here to emphasize that the luminosity does not depend on the bin). The correction factors  $A_i$ ,  $B_i$ , and  $R_i$  refer to the acceptance, bin center, and radiative corrections for bin  $i$  respectively.

## 6.2 Inelastic Scattering Model

A particularly important aspect of this validation study is the reference model. Not only is the model used to predict the cross section for comparison, it also sampled in the Monte Carlo event generators used in study detector acceptances and radiative corrections. The model which is used in this study was first developed by Cynthia Keppel [? ]. Data taken by SLAC experiments NE11 and E133 was used to fit a 24 parameter model, 3 background terms and 3 resonance terms in  $W$  as well as polynomial in  $Q^2$ . While the model is constrained at higher  $W$  by data points from the DIS region, it is designed to operate in the resonance region (starting at the pion production threshold).

## 6.3 Analysis

### 6.3.1 Event Selection

The problems solved by event selection are two-fold. First, it is required that the negative momentum transfer squared  $Q^2 > 1 \text{ GeV}^2/c^2$  is sufficiently large so that our measurement can be considered part of the DIS region. Analyses in CLAS have typically used  $1 \text{ GeV}^2/c^2$  as the working assumption for what constitutes the lowest acceptable momentum transfer to be considered DIS, and this value is used in the SIDIS presented in this work. Because we study the resonance region with  $W \in [1.1, 2.1]$  and the beam energy is  $E_{beam} = 5.498 \text{ GeV}$  the kinematics are sparsely populated for  $Q^2 < 1.6 \text{ GeV}^2/c^2$  and this limit is applied in our study. The second important function of event selection in this study is to avoid the largest source of background, Bethe-Heitler events.

As mentioned in the introduction, Bethe-Heitler events (where a real photon is radiated by the elec-

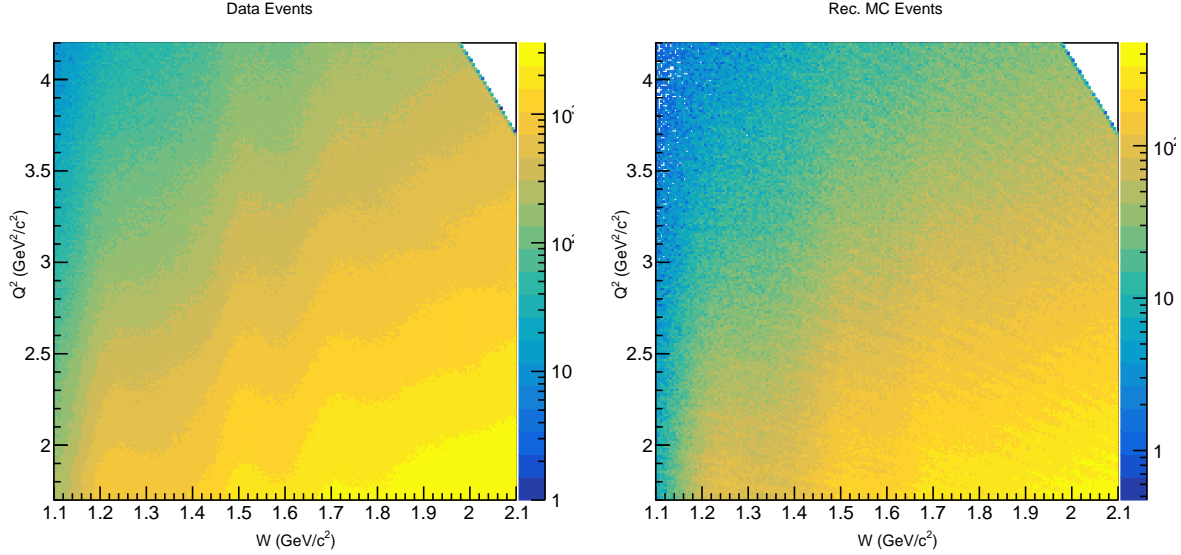


Figure 6.1: Data and Simulation (reconstructed) events are compared.

tron in the initial or final state) are the dominant source of background for this measurement. When studying elastic scattering the final state electron and the scattered target proton are detected, in this case it's possible to apply energy-momentum constraints to the system and eliminate radiative Bethe-Heitler events. However, in this measurement only the final state electron is detected and used to workout the event kinematics. There is no way to directly apply energy-momentum conservation to eliminate Bethe-Heitler events. Faced with this problem, we choose to restrict the values of *inelasticity*  $y = 1 - E'/E < 0.7$  that are included in our event sample to limit this contribution. This restriction is applied because events with large- $y$  have a significantly higher probability to be Bethe-Heitler events (this is verified by simulation and shown below in figure 6.3.1). This restriction is equivalent to enforcing a minimum energy for the scattered electron.

$$E_{min} = E_{beam}(1 - y_{max}) \approx 1.6 \text{ GeV} \quad (6.2)$$

Figure 6.3.1 shows the kinematic distribution of events from simulation and data, and illustrates the need for this  $y$  cut. The number of Bethe-Heitler events in our sample is further reduced by limiting the measurement to the resonance region. Simulations for  $E_{beam} = 5.498 \text{ GeV}$  show that the majority of Bethe-Heitler events occur between  $W \in [2, 3]$ .

### 6.3.2 Binning

Detected inclusive events are divided into 10 bins of equal size in  $Q^2$  and 40 bins of equal size in  $W$  (for a total of 400 bins for each sector). Bins are chosen small enough in  $W$  to detect resonance features,

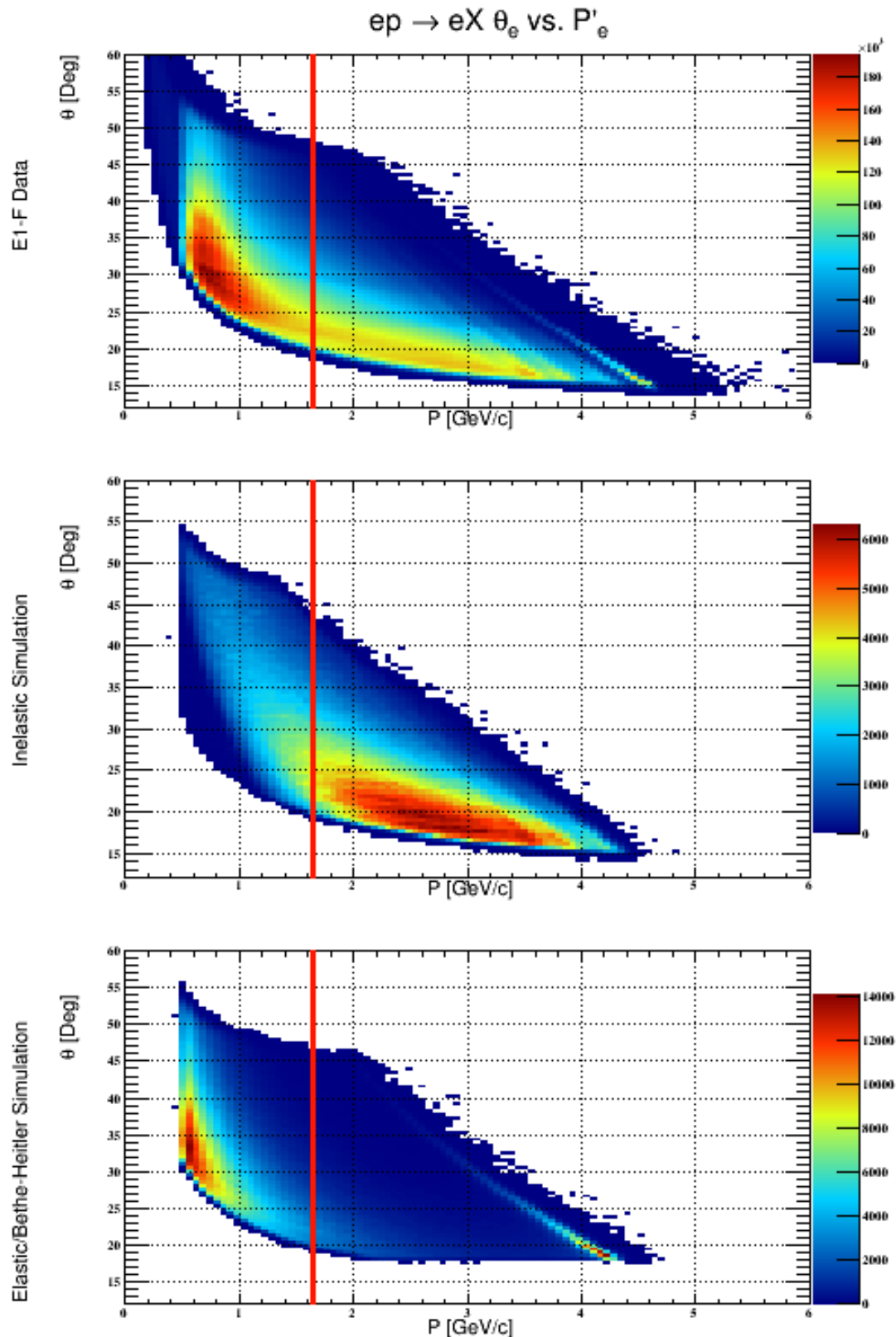


Figure 6.2: Event distributions ( $\theta_e$  vs  $p$ ) for data, simulated inelastic events, and simulated elastic events with radiation are shown. The red line indicates the momentum cut applied by restricting  $y < 0.7$ . The band of events on the right side of the figure contains all un-radiated elastic events. The larger portion of events present on the left side are Bethe-Heitler events which we wish to avoid in our analysis.

Variable	N	Min.	Max	Width
$W$	40	1.1	2.1	0.25
$Q^2$	10	1.7	4.2	0.25

Table 6.1: Summary of  $W$  and  $Q^2$  binning used for the inclusive cross section.

but larger than the resolution of CLAS to avoid having a large numbers of events reconstructed in a bins that they do not belong in. Equal sized bins are chosen for their simplicity and because for cross sections (unlike asymmetry measurements) we can tolerate bins with comparatively low statistics.

### 6.3.3 Simulation

All processes that CLAS measures are observed through the combination of signals from several sub-detectors. During analysis all sub-systems are calibrated accurately, but such a complicated system still often produces distributions that do not look like the true physical distribution. This discrepancy arises from the combination of several effects.

1. Holes, barriers, obstructions, shadows of other detectors, and any other physical effects that prevent events from being measured in some range of  $\theta, \phi$  are known as geometrical acceptance effects. An important geometrical acceptance effect is the presence of the torus coils in between every sector. These represent a complete loss of information for a small range of  $\phi$  between each sector.
2. Inefficiencies due to the probabilistic nature of particle interaction in the detector subsystems also lower the overall acceptance.
3. Detectors have finite spatio-temporal resolutions.

In order to understand and limit the impact of these effects on the physics extracted from the experiment, a mock experiment is simulated. In the simulated experiment everything is modeled as realistically as possible. The simulation used for CLAS is called GSIM and is based on the CERN package GEANT3 (GEometry ANd Tracking).

In this controlled environment, control samples of events can be generated and fed into the simulation. The output of GSIM is a bos file that is similar to the raw data from the data acquisition system. This is then reconstructed using the same reconstruction algorithm that is applied to data (`userana`).

By retaining the truth information for all particles that are generated, the effect of the detector can be studied completely. These concepts can be stated more formally by considering the true  $t(x')$  and measured  $m(x)$  distributions of some observable. In the absence of background processes, the relationship between these distributions is expressed as a Fredholm integral equation of the first kind.

$$m(x) = \int_{\Omega} K(x, x') t(x') dx' \quad (6.3)$$

Here  $K(x, x')$  is a kernel which encodes information about detector acceptance due to the effects described above. The goal of the Monte Carlo simulation is to *unfold* the measured distribution  $m(x)$  by providing an estimate of  $K(x, x')$  and finally corrected the data to get  $t(x)$ .

Observed events are usually aggregated into bins and the problem is naturally discretized and written in vector-matrix form.

$$\mathbf{A}\mathbf{x} = \mathbf{y} \quad (6.4)$$

In this notation  $\mathbf{A}$  represents the response matrix, a discretized version of the kernel function  $K$ , the vector  $\mathbf{y}$  represents the measured distribution in the bins, and the vector  $\mathbf{x}$  is the true distribution over the bins. The matrix elements  $A_{ij}$  can be estimated by using generating events, passing them through a Monte-Carlo detector simulation, and then counting the number of events that are reconstructed in bin  $i$  when generated in bin  $j$ . This quantity is then normalized by the total number of events generated in the  $j^{th}$  bin. In the absence of bin migration and with perfect acceptance this matrix is the identity matrix  $I^n$  where  $n$  is the total number of bins.

$$A_{ij} = \frac{n_{rec=i, gen=j}}{n_{gen=j}} \quad (6.5)$$

The binned true distribution can be recovered by inverting the response matrix and correcting the observed distribution.

$$\mathbf{x} = \mathbf{A}^{-1}\mathbf{y} \quad (6.6)$$

In the absence of bin migration, the matrix becomes diagonal with efficiency elements  $\epsilon_i$  that represent the fraction of events reconstructed in the bin  $i$ .

$$\mathbf{A} = \begin{pmatrix} \epsilon_0 & 0 & 0 \\ \vdots & \ddots & \\ 0 & & \epsilon_n \end{pmatrix} \quad (6.7)$$

The inverse is,

$$\mathbf{A}^{-1} = \begin{pmatrix} 1/\epsilon_0 & 0 & 0 \\ \vdots & \ddots & \\ 0 & & 1/\epsilon_n \end{pmatrix} \quad (6.8)$$

and the corrected observation for the  $i^{th}$  bin is simply given by the observation over the efficiency.

$$t_i = \frac{m_i}{\epsilon_i} = m_i \frac{n_{gen=i}}{n_{rec=i}} \quad (6.9)$$

This is the simple *bin-by-bin* acceptance correction method, which is widely used and produces accurate results provided that bin migration is not significant. In this analysis the simple bin-by-bin acceptance correction is used.

### 6.3.4 Radiative Corrections

Inclusive events detected in CLAS are really *radiated* inclusive events. By using the term *radiated*, one implies that the electron could have radiated a real photon in the initial or final state, or that internal radiative correction diagrams could have influenced the event kinematics. Unfortunately, there is no way of detecting these events. For this reason, a radiative correction procedure that unfolds these effects from the cross section is applied to our measured distributions.

Two Monte Carlo event generators are used to calculate radiative corrections for each bin, both sample from the cross section model discussed in the beginning of the chapter. The first program generated events with no radiative corrections by sampling directly from the cross section model. The second program uses the same cross section model but generates radiated events following the procedure of Mo and Tsai [?] which includes corrections due to internal and external Bremsstrahlung. The correction ratio for the  $i^{th}$  bin  $R^{(i)}$  is defined for the  $i^{th}$  bin as shown below.

$$R^{(i)} = \frac{n_{unrad}^{(i)}}{n_{rad}^{(i)}} \quad (6.10)$$

This factor can be estimated without passing events through the simulation and the results are used directly from the output of the event generator to correct the cross section.

### 6.3.5 Bin Center Corrections

Measurement of the cross section is done in bins, meaning that what is actually measured is the average cross section over some finite range of  $W$  and  $Q^2$  for each bin. When reporting and plotting the results the  $W$  and  $Q^2$  value at the center of the bin is typically quoted. If a model is available for comparison, the model is usually queried at the bin center, and the resulting prediction is often incorrect. In order to obtain the correct prediction, one should average the model prediction over the measured bin. In this study, an accurate model prediction is available (described in detail below) and a correction factor is applied to the measured cross section value to remove the effect of plotting and reporting the cross section at the central bin value. The factor,

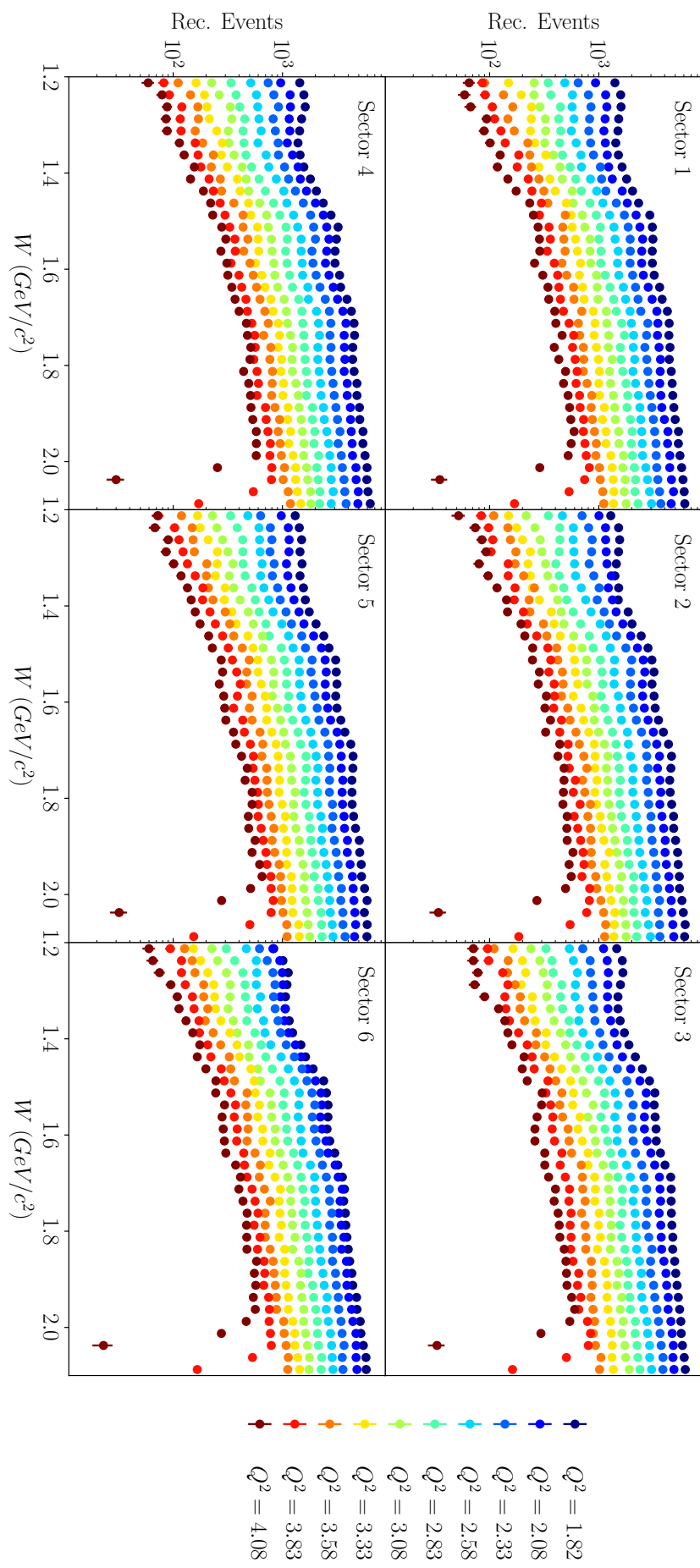


Figure 6.3: Reconstructed Monte Carlo events displayed for different sectors (by panel) and different  $Q^2$  bins represented by different colors.

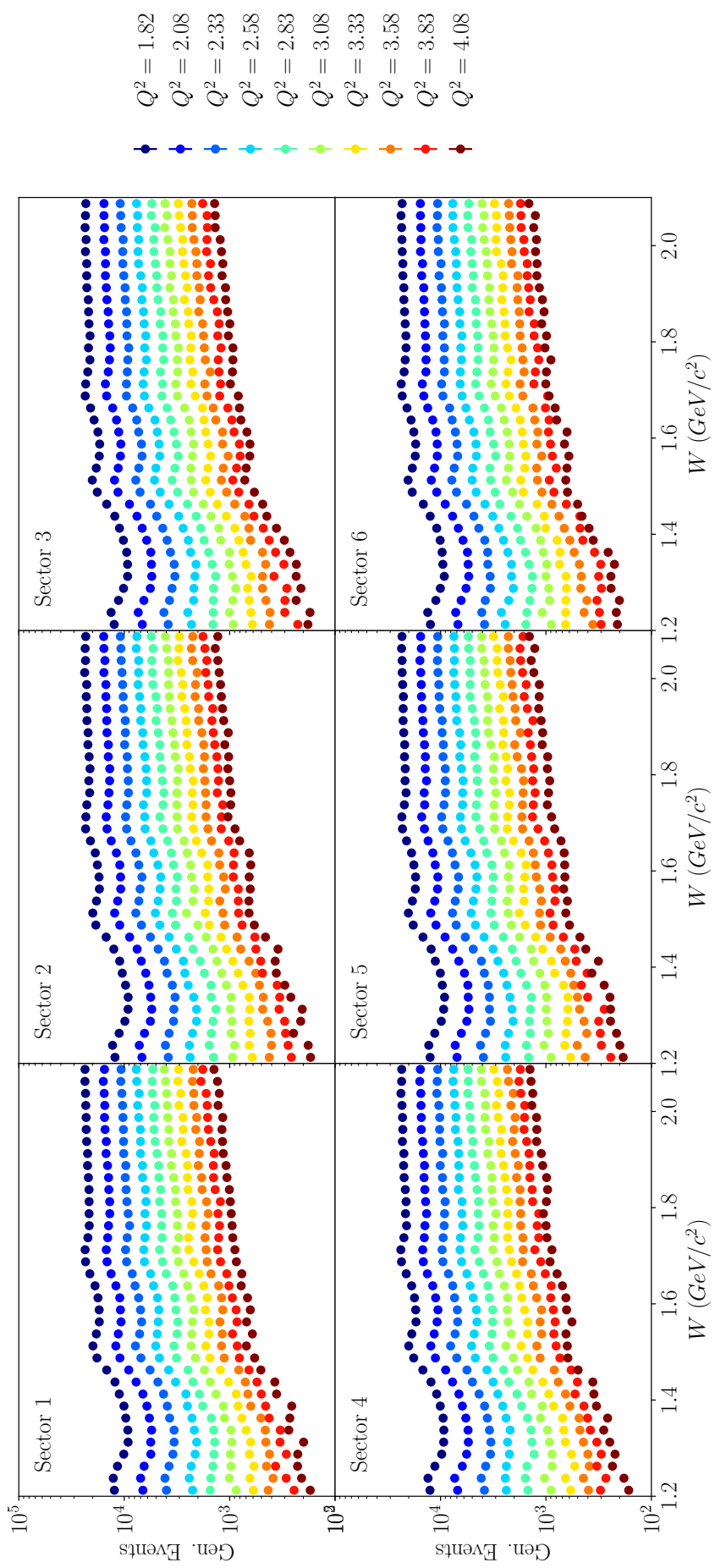


Figure 6.4: Generated Monte Carlo events displayed for different sectors (by panel) and different  $Q^2$  bins represented by different colors. These events were generated with radiative effects.

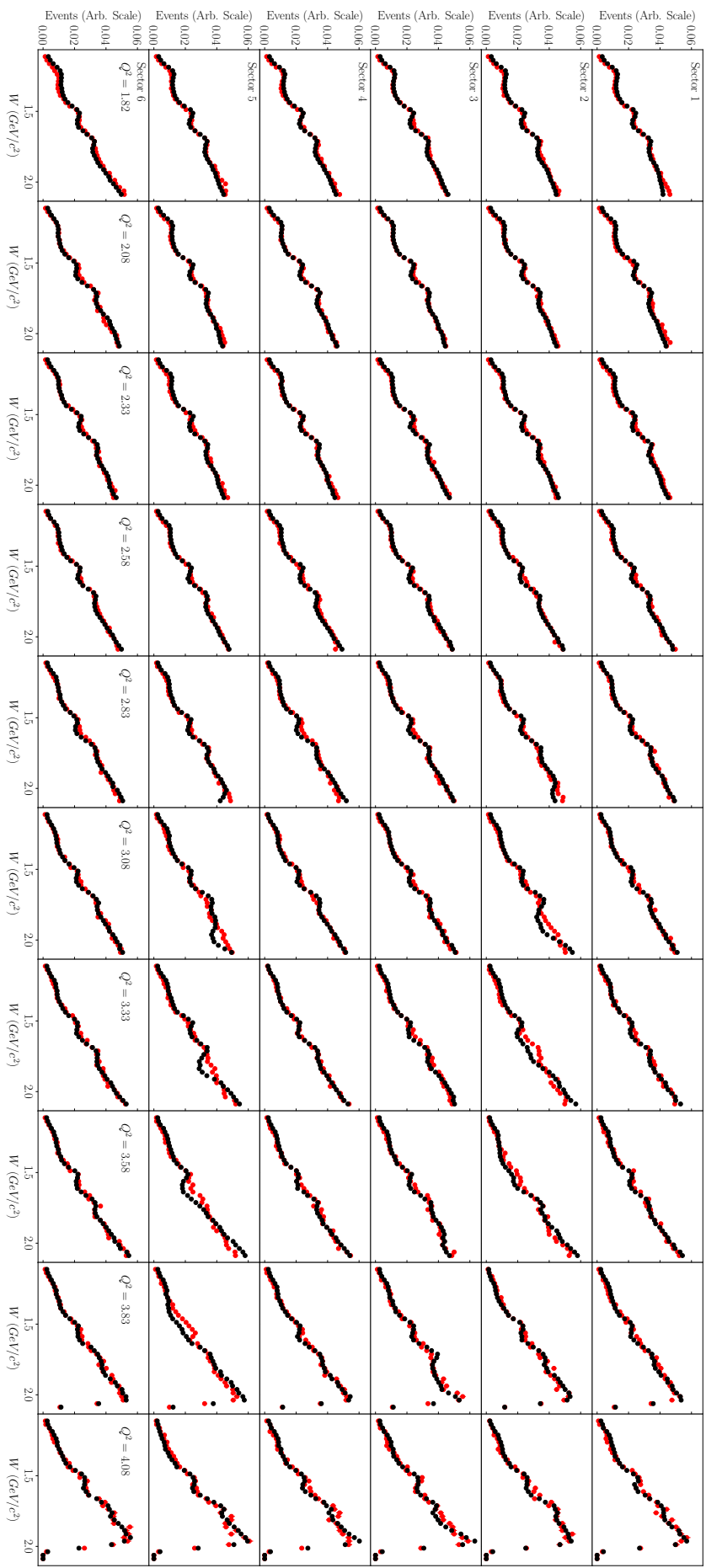


Figure 6.5: Reconstructed events from data (black) and Monte Carlo (red) are superimposed to show that the simulation is a good approximation to the physics, a fact important for the accurate calculation of acceptance.

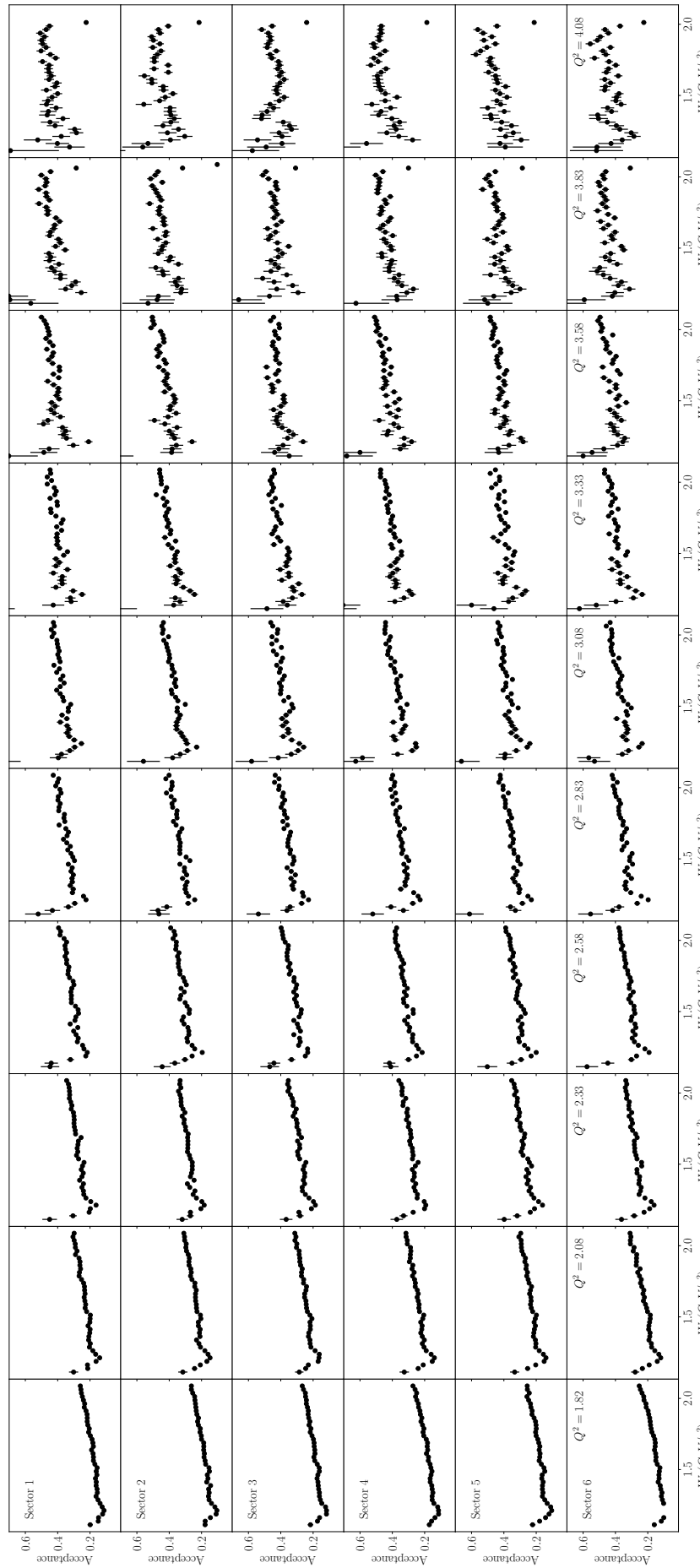


Figure 6.6: Acceptance corrections applied to the inclusive cross section are shown above in sixty panels that correspond to increasing  $Q^2$  from left to right, and increasing sector number from top to bottom.

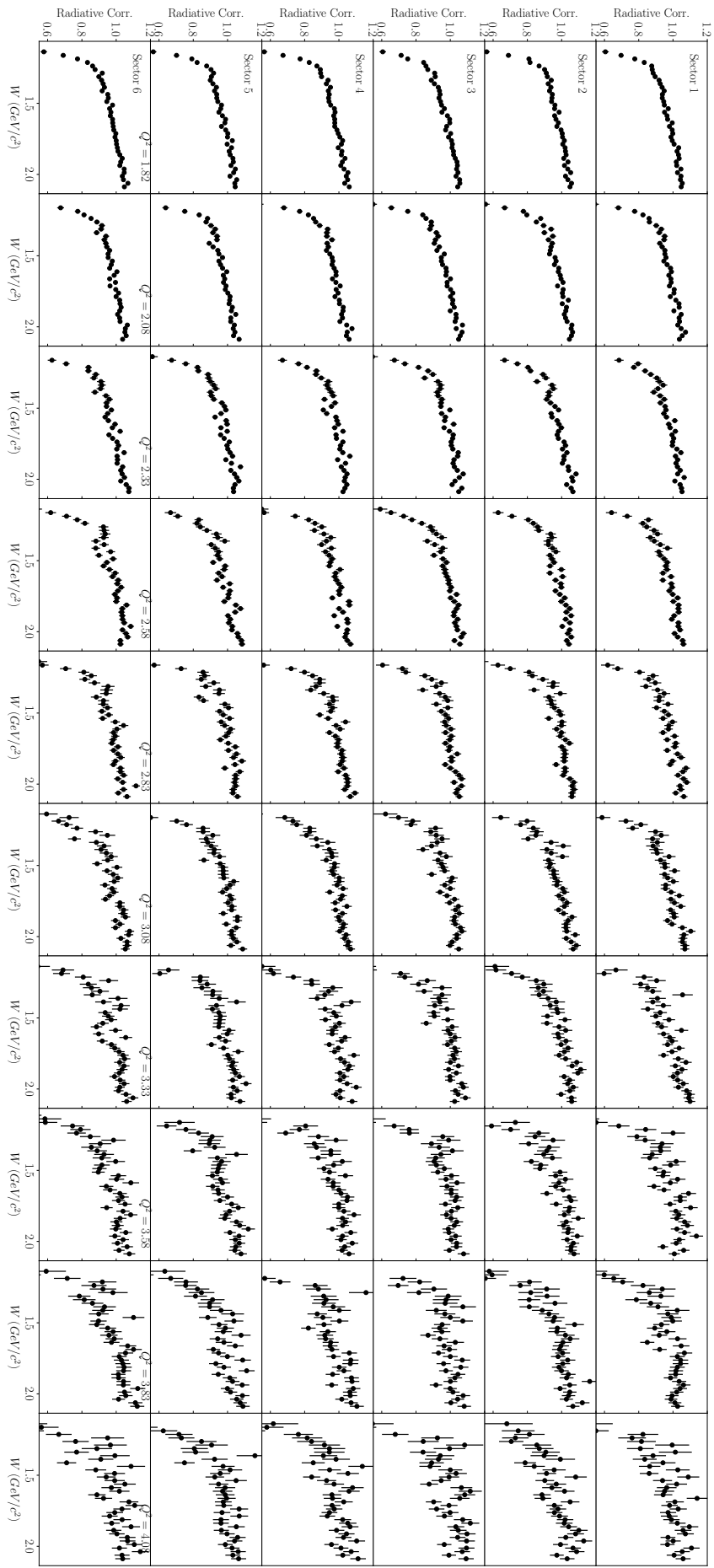


Figure 6.7: Radiative corrections applied to the inclusive cross section are shown above in sixty panels that correspond to increasing  $Q^2$  from left to right, and increasing sector number from top to bottom.

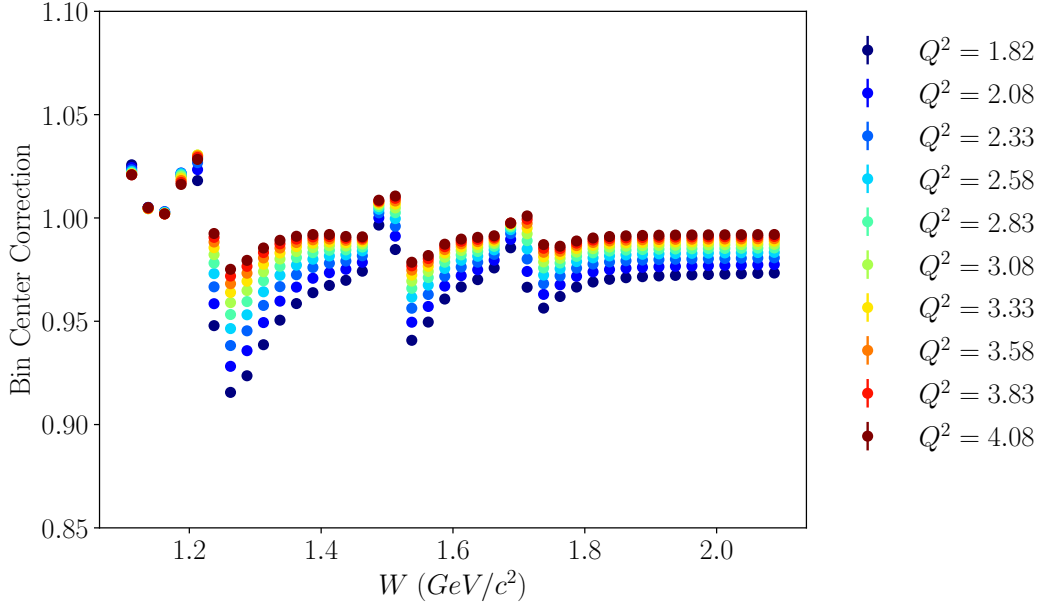


Figure 6.8: The bin center correction applied to the inclusive cross section is shown for different values of  $Q^2$  (indicated by color) as a function of  $W$  on the horizontal axis. This correction is the same for all sectors.

$$B_i = \frac{\sigma_{center}}{\sigma_{avg}} \quad (6.11)$$

$B_i$  is calculated from the model for each bin  $i$  and applied to the measured cross section. This factor is calculated once for each bin, and does not depend on the sector. We observe that the correction factor depends more strongly on  $Q^2$  than  $W$  which is sensible because the cross section varies more rapidly over  $Q^2$ . Additionally, the correction factor is larger near the resonances in  $W$ .

### 6.3.6 Model Comparison

The cross section extracted in this study is in agreement with the predictions from the model, shown in figure ??.

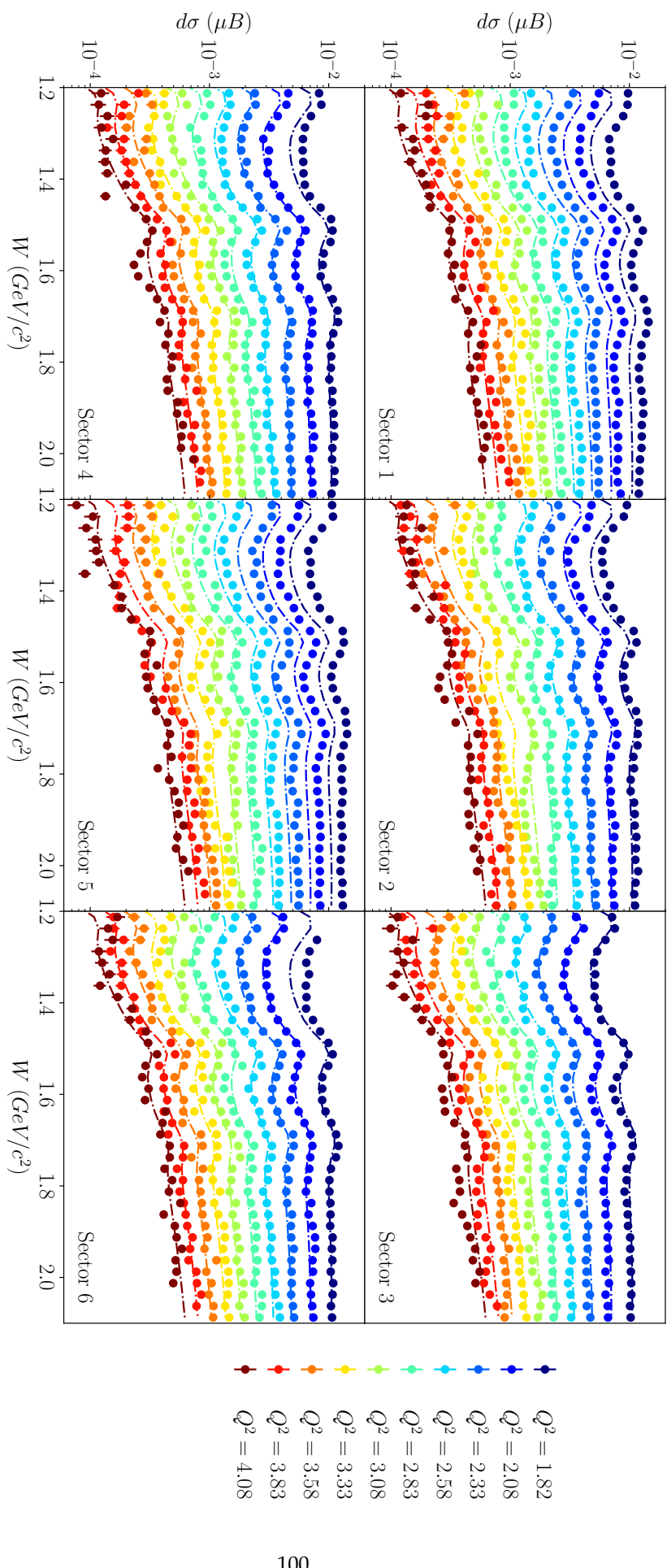


Figure 6.9: Each panel above shows one of the six sectors of CLAS, the horizontal axis shows  $W$  and superimposed on the figure are the cross sections for different bins of  $Q^2$ . For simplicity of the visualization each reported value of  $Q^2$  is the bin center.

# Chapter 7

## SIDIS Cross Section

This chapter discusses the analysis of semi-inclusive deeply inelastic electro-production of  $\pi^+$  and  $\pi^-$ .

After a brief motivation, the analysis details are described.

### 7.1 Introduction

The SIDIS cross section for scattering of unpolarized electrons on an unpolarized proton target can be written in terms of three coefficients  $A_0$ ,  $A_{UU}^{\cos(\phi_h)}$ , and  $A_{UU}^{\cos(2\phi_h)}$  as shown below. Each of these coefficients depends on the electron and hadron kinematic variables  $A \rightarrow A(x, Q^2, z, P_T^2)$  which have been omitted for readability.

$$\frac{d^5\sigma}{dx dQ^2 dz dP_T^2 d\phi_h} = A_0 \left[ 1 + A_{UU}^{\cos \phi_h} \cos \phi_h + A_{UU}^{\cos(2\phi_h)} \cos(2\phi_h) \right] \quad (7.1)$$

The  $A$  coefficients are defined in terms of structure functions  $F$ , and were measured from the E1-F dataset by N. Harrison as reported in [? ].

$$A_0 = \frac{\pi\alpha^2 y(1+\gamma^2/2x)}{2EM_p x^2 Q^2 (1-\varepsilon)} \left( F_{UU,T} + \varepsilon F_{UU,L} \right) \quad (7.2)$$

$$A_{UU}^{\cos \phi_h} = \sqrt{2\varepsilon(1+\varepsilon)} \frac{F_{UU}^{\cos \phi_h}}{F_{UU,T} + \varepsilon F_{UU,L}} \quad (7.3)$$

$$A_{UU}^{\cos(2\phi_h)} = \varepsilon \frac{F_{UU}^{\cos(2\phi_h)}}{F_{UU,T} + \varepsilon F_{UU,L}} \quad (7.4)$$

To measure the structure functions, the five dimensional differential cross section is measured 7.5. The  $\phi_h$  measurements in each kinematic bin  $(x, Q^2, z, P_T^2)$  are used to perform parameter estimation of the terms  $A_0$ ,  $A_{UU}^{\cos(\phi_h)}$ , and  $A_{UU}^{\cos(2\phi_h)}$ . The structure functions can then be measured by rearranging equation 7.4 as shown in 7.6.

$$\frac{d^5\sigma}{dx dQ^2 dz dP_T^2 d\phi_h} = \frac{1}{\Delta x \Delta Q^2 \Delta z \Delta P_T^2 \Delta \phi_h} \frac{N_{obs}^{(i)}}{\mathcal{L} A^{(i)} R^{(i)}} \quad (7.5)$$

$$F_{UU,T} + \varepsilon F_{UU,L} = A_0 \frac{2(1-\varepsilon) E_B M_p x^2 Q^2}{\pi \alpha^2 y (1 + \gamma^2 / 2x)} \quad (7.6)$$

$$F_{UU}^{\cos \phi_h} = A_{UU}^{\cos \phi_h} \frac{F_{UU,T} + \varepsilon F_{UU,L}}{\sqrt{2\varepsilon(1+\varepsilon)}} \quad (7.7)$$

$$F_{UU}^{\cos(2\phi_h)} = A_{UU}^{\cos(2\phi_h)} \frac{F_{UU,T} + \varepsilon F_{UU,L}}{\varepsilon} \quad (7.8)$$

Results for the extracted structure functions as well as the five dimensional differential cross section are presented at the conclusion of this chapter.

## 7.2 Hadron Identification

Classification of hadrons in CLAS is done by using momentum measurements as well as time of flight measurements, as was described in detail in chapter 4. The velocity (in units of  $c$ )  $\beta = v/c$  is calculated for candidates by using the events good electron to calculate a start time and by using the distance along the fit candidate track to the time of flight paddle. Hadrons with mass  $m$  and momentum  $p$  are theoretically expected to have a  $\beta_{exp}$  value given in equation 7.9. This equation has the important feature that for a fixed momentum value, hadrons with different masses are separated in their  $\beta$  values.

$$\beta_{exp}(p) = \frac{1}{\sqrt{1 + (m/p)^2}} \quad (7.9)$$

In chapter 4, the hadronic identification methods described used a probabilistic interpretation of the difference between the observed values of  $\beta$  and the expected values given by 7.9 (or determined by fitting small deviations from the theoretical case). This study was performed before that identification routine was developed, and therefore uses a slightly different boundary and interpretation (described first by N. Harrison in his thesis work [?]). Fiducial cuts used for positives and negatives are those described in chapter 4, and will not be discussed here.

In order to determine the cut boundaries, the events are fit with an unnormalized Gaussian distribution in each of 70 momentum bins and the mean  $\mu$  and standard deviation  $\sigma$  are recorded. Pions which fall between  $\mu - 3\sigma \leq \beta \leq \mu + 3\sigma$  are kept for analysis. At higher momentum positive pi-mesons are difficult to separate from protons than at lower momentum values. To accommodate this, the  $\sigma$  value is reduced after 2 GeV.

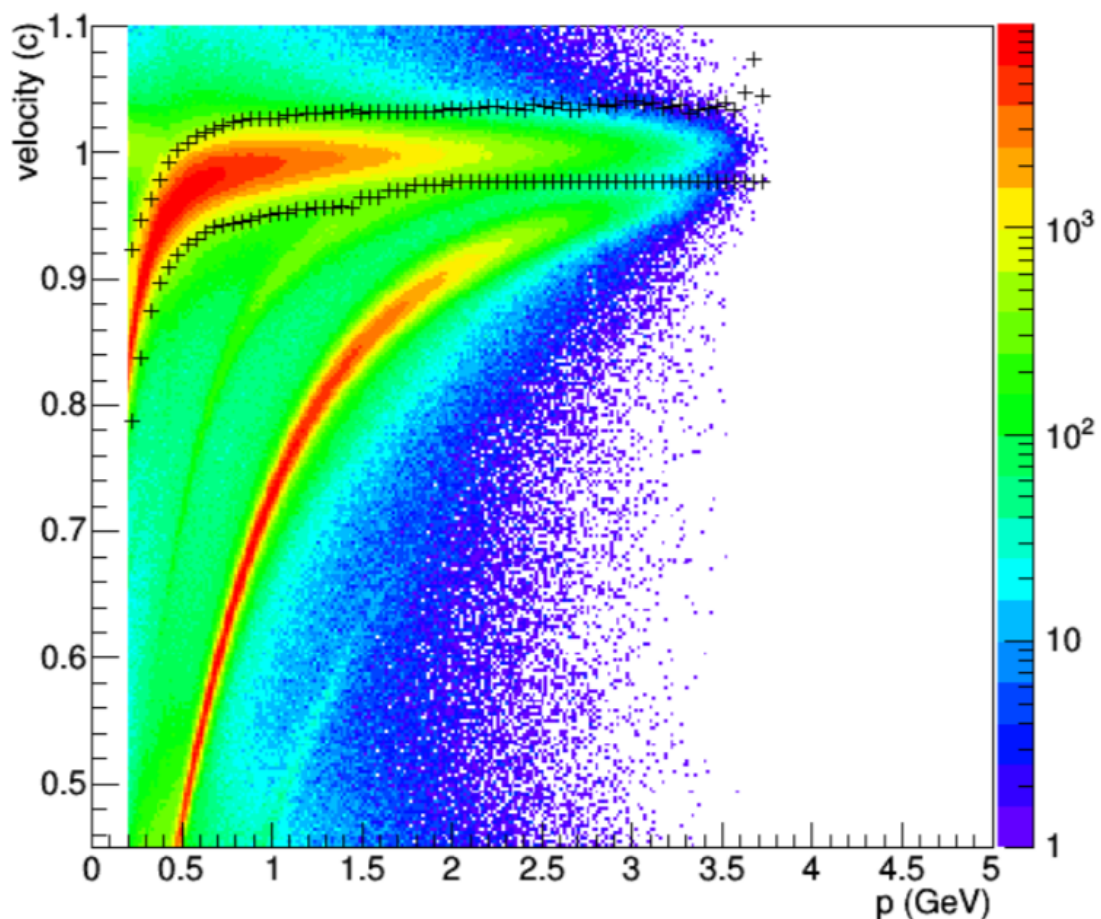


Figure 7.1: Positively charged  $\pi$  mesons are identified by applying cuts to the momentum dependent  $\beta$ .

Hadron	$p_{min}$ (GeV)	$p_{max}$ (GeV)
$\pi^+$	0.2	3.75
$\pi^-$	0.2	3.25

Table 7.1: The limits used for pion momentum used in the fitting of  $\beta$  for both charged pi-mesons.

### 7.3 Event Selection

The identification of an event which contains a good electron and a good pion ( $\pi^\pm$ ) is the first step in selecting SIDIS events from the dataset. Next, events that meet the working assumption for what constitutes the DIS region ( $Q^2 > 1.0 \text{ GeV}^2$  and  $W > 2.0 \text{ GeV}$ ) are selected. A missing mass cut is used in this analysis to remove low lying exclusive resonances which are not produced by the SIDIS mechanism. Accordingly it is required that the missing mass  $M_X(ep \rightarrow ehX)$  be greater than 1.35 GeV (in the positive channel this excludes the delta resonance).

One additional kinematic restriction is applied at the event selection stage, a cut on the maximum allowable inelasticity  $y_{max}$ . Full radiative corrections will be discussed in detail, but this kinematic restriction excludes events which have extremely high values of  $Q^2$  and are much more likely to have radiated a photon in the initial or final state. In this analysis  $y_{max} = 0.85$  is used.

### 7.4 Binning

Both  $\pi^+$  and  $\pi^-$  are binned using the same scheme. The momentum fraction  $x$  is divided into five equally sized bins from 0.1 - 0.6. With the exception of the highest  $x$  bin, each is split into two  $Q^2$  bins. This binning scheme for  $x - Q^2$  is displayed in figure 7.2.

The hadronic variables are binned finer, the  $z$  axis is divided into 18 equal sized bins between 0-0.9, and the transverse momentum squared  $P_T^2$  is binned in 20 equally sized bins from 0-1  $\text{GeV}^2$ . This simple grid is shown on figure 7.3. The average value of the kinematic variables in each bin is calculated from the event sample and displayed in the results table at the end of this thesis.

### 7.5 MC Simulation

Acceptance corrections based on Monte Carlo simulation of the CLAS detector are vital in the accurate calculation of cross sections, and are performed in this work by using a modified version of **PYTHIA** called **clasDIS**, the detector simulation **GSIM**, and the resolution smearing program called **GPP**. Two main challenges existed in calculating acceptance corrections for this cross section measurement. The first challenge, which is common to all acceptance calculations, is that the acceptance depends weakly on the model input used. The second challenge facing this calculation is that at present the values of the coefficients  $A$  which shape the  $\phi_h$  distributions are not known, and therefore the events are simulated flat.

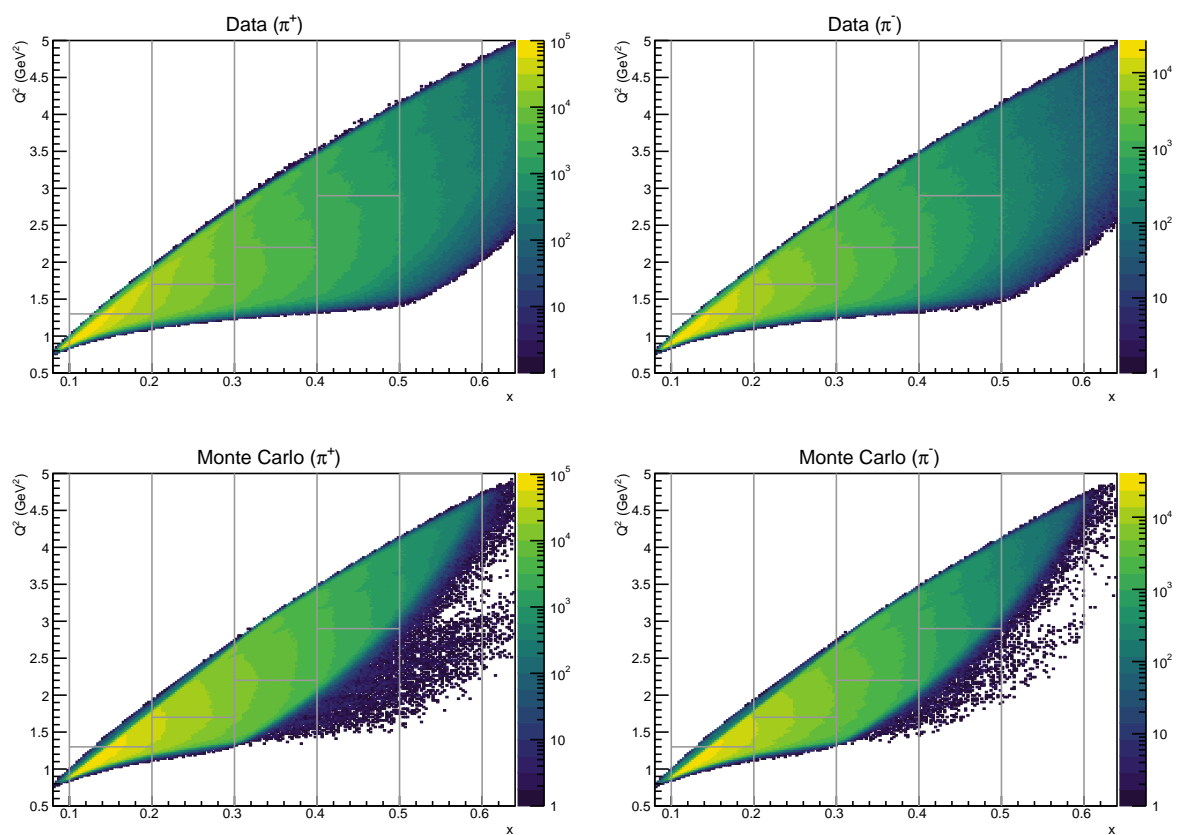


Figure 7.2: The kinematic distributions for  $\pi^\pm$  electron variables shown with binning overlaid.

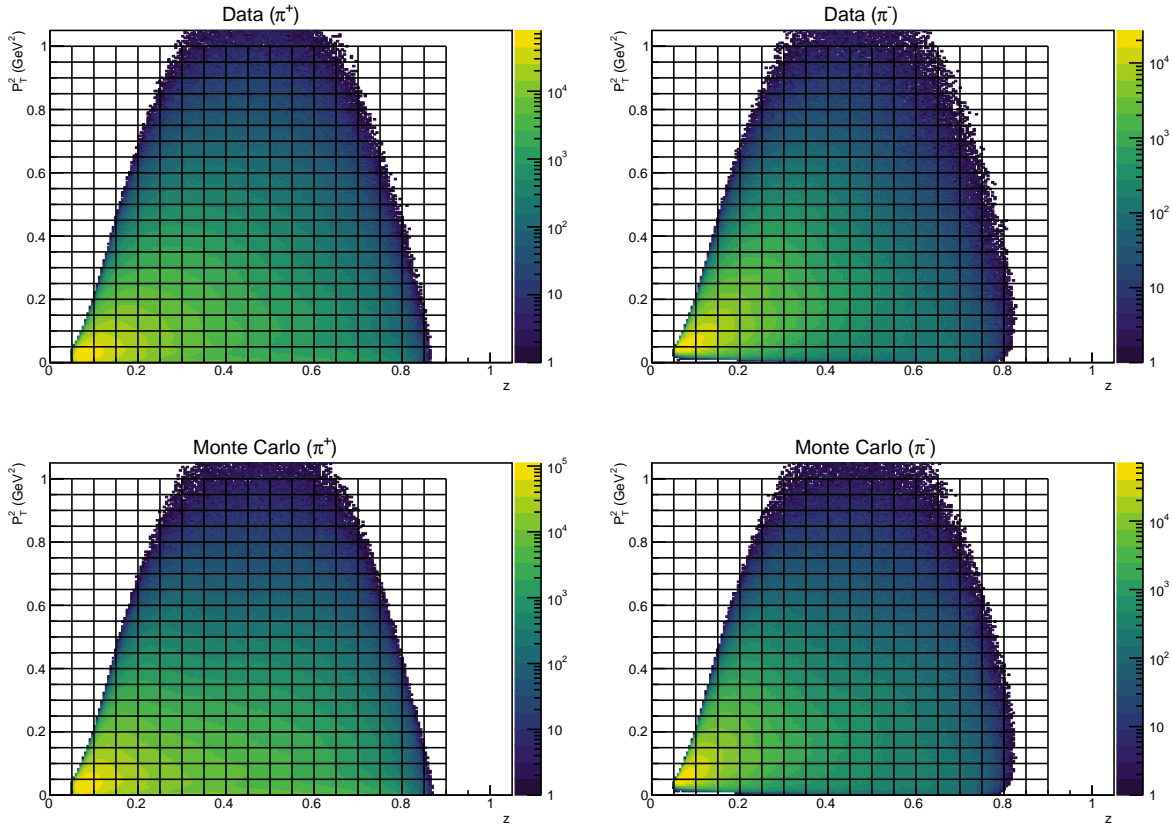


Figure 7.3: The kinematic distributions for  $\pi^\pm$  hadron variables shown with binning overlaid.

In order to resolve the first challenge, the acceptance model used is included as a source of systematic uncertainty. This quantifies the amount to which the answer changes based on different input physics models. In answering the second challenge posed, the model is made more realistic by an iterative procedure of using the extracted  $A^{(0)}$  coefficients to weight the generated events and then produce the coefficients  $A^{(1)}$ , where the superscript denotes the iteration. After two iterations, the extracted values of  $A$  no longer vary outside of parameter estimation errors. The last ( $2^{nd}$ ) iteration is used for the simulation of events in this analysis, and the subsequent iteration ( $1^{st}$ ) is used to study systematic uncertainties associated with the difference between both models.

### 7.5.1 Acceptance Corrections

The generator `clasDIS` is used with the modified  $\phi_h$  dependence and more than 800 million  $\pi^+$  events are simulated, as well as more than 600 million  $\pi^-$  events. The acceptance is calculated over the phase space and used to correct the cross section. A sample of the acceptance is shown in figure 7.4. Two main features are evident, first, the segmented nature of the CLAS detector in the azimuthal direction correlates to the center of mass hadron-electron angle  $\phi_h$  and cause a periodic modulation of acceptance.

Additionally, the central region of  $\phi_h$  has the lowest acceptance of any value. For this reason, bins in the central region are excluded if they have large statistical errors from acceptance or have extremely low acceptance values. The resulting lack of points in the central region impacts the parameter estimation, and is discussed later in the section on parameter estimation.

## 7.6 Radiative Corrections

The Born cross section, in which no radiation takes place during the scattering, is the cross section that we intend to measure. However, the incoming and scattered electron can emit photons, and therefore the cross section measured in the lab is not the Born cross section but the *radiated* cross section. In addition to initial and final state radiation, radiated exclusive events can have long tails and enter into the SIDIS kinematics. These effects are calculable by using the software package called `HAPRAD`, which takes as an input a Born cross section model  $\sigma_{Born}$  and produces the radiated version of the cross section. This calculation is performed at each kinematic point that is measured.

$$R = \frac{\sigma_{rad}(x, Q^2, z, P_T^2, \phi_h)}{\sigma_{Born}(x, Q^2, z, P_T^2, \phi_h)} \quad (7.10)$$

This software package is used to correct our measured cross section by calculating the ratio  $R_i$  for each bin i (as shown in equation 7.10). Because the correction depends on the model used, two different models are used and the difference in the extracted structure functions is assigned as a systematic uncertainty in our final analysis.

## 7.7 Parameter Estimation (Fitting)

Once measurements of the 5-differential corrected yield are made,  $\chi^2$  minimization is used to estimate the value of the  $A$  coefficients in every bin of  $(x, Q^2, z, P_T^2)$ . The difference between the data points and the model prediction is called the *residual*, and the square sum of these residuals is known as the mean squared error. The  $\chi^2$  is simply extends this by the addition of an error term in the denominator as shown in equation ??.

$$\chi^2 = \sum_{i=1}^n \frac{(d_i - t_i)^2}{\sigma_i^2} \quad (7.11)$$

Here  $n$  refers to the degrees of freedom, or the number of data points used in fitting the model parameters. The `Minuit` minimization package which is included in CERN's ROOT is used to minimize the  $\chi^2$  function for each bin and provides the parameters and their associated errors.

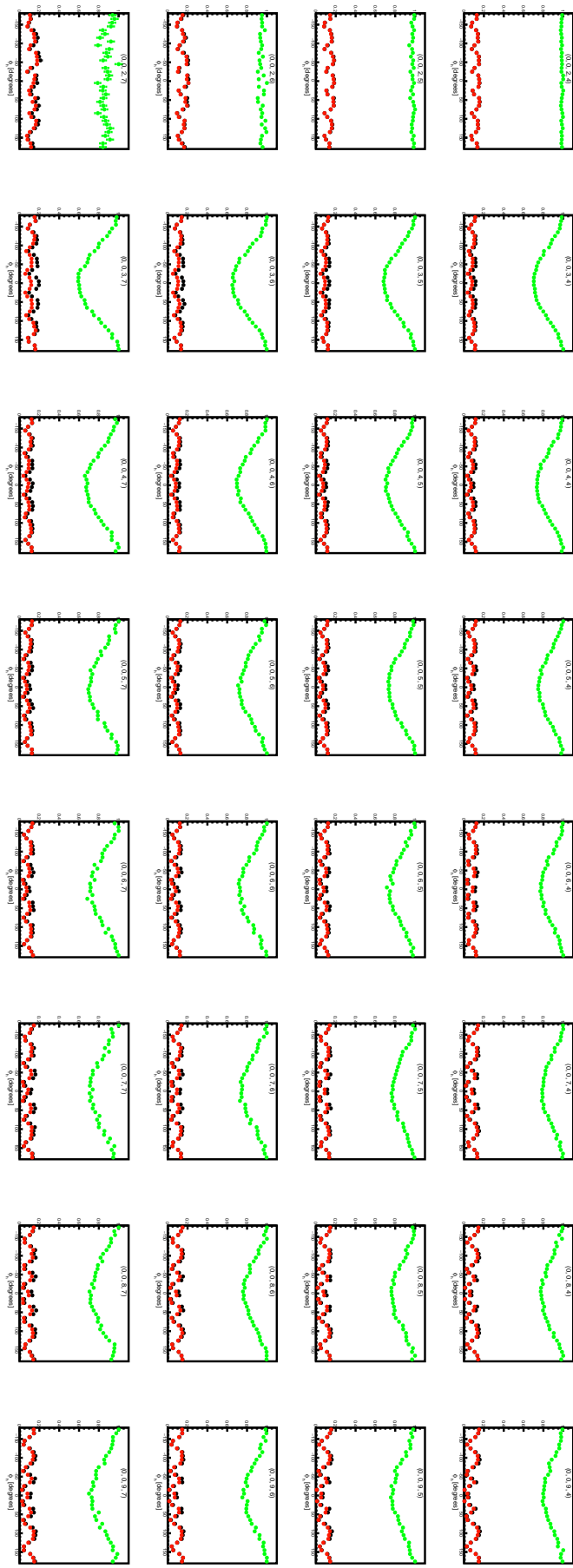


Figure 7.4: Acceptance corrections shown for different  $z$  bins (increasing over the horizontal axis) and  $P_T^2$  bins (increasing down the vertical axis) are displayed in red. Generated events are displayed in green, and in red the reconstructed events are shown normalized by the maximum number of generated events in any bin. On each figure the complete bin index is given in the format  $(x, Q^2, z, P_T^2)$ .

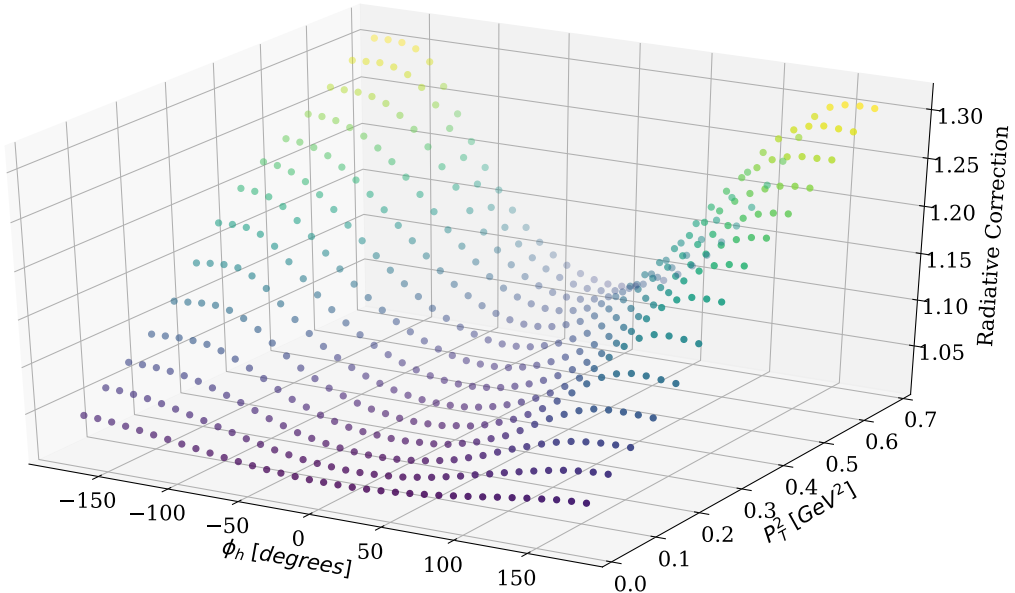


Figure 7.5: Radiative corrections are displayed as a 3-dimensional scatter plot for the bin with indices  $(x = 0, Q^2 = 1, z = 4)$  for  $\pi^+$ . This correction includes exclusive contributions  $\sigma_{tail}$ .

### 7.7.1 Minimal Coverage in $\phi_h$ for Fitting

As points are removed from the central  $\phi_h$  region, fitting becomes less stable. This is particularly problematic as the periodicity of the function increases. Because the central region of  $\phi_h$  has been removed in some cases due to low acceptance, this problem needs to be addressed before the fitting algorithm is applied to all the kinematic bins.

In order to alleviate this concern, the bins of  $(x, Q^2, z, P_T^2)$  that have a gap from  $\Delta\phi_h > 60^\circ$  are not fit (-30 to 30 or larger). This value was set by generating psuedo-data with a known  $\phi_h$  dependence given in terms of the three  $A$  coefficients. The distribution was fit, and then points were removed and the distribution was fit again. This was repeated for several different values of  $A$ , particularly the cosinusoidal terms. This study is described in detail in [? ].

## 7.8 Systematic Uncertainties

Thirteen possible sources of systematic effect have been identified 7.8, and the values for each are varied slightly from the nominal values in order to observe the affect that each has on the final results. Each of the values is increased and decreased slightly in accordance with the amount of uncertainty that exists around its ideal value. The uncertainty due to source  $i$  is calculated from these variations by calculating the RMS of the deviations, as shown in equation 7.8.

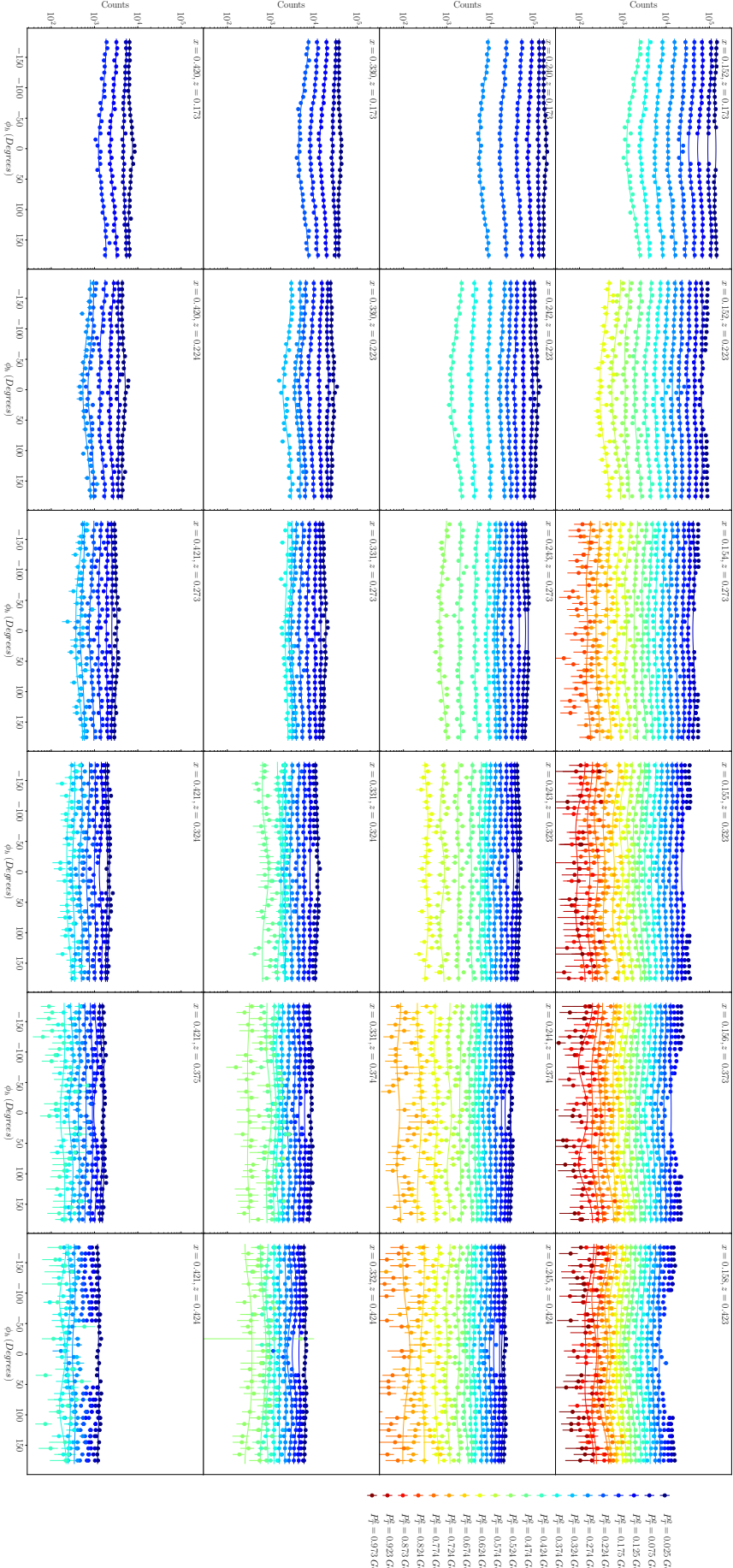


Figure 7.6: Corrected  $\pi^+$  yields are fit and the coefficients  $A_0$ ,  $A_{UU}^{\cos(\phi_h)}$ , and  $A_{UU}^{\cos(2\phi_h)}$  are estimated for each kinematic bin. In this figure bins of  $P_T^2$  are superimposed. Rows in the figure indicate increasing  $x$ , while  $z$  increases with the column.

image/plots/sidis/pim\_counts\_with\_fit\_x\_z.pdf

Label	Source	Description
0	electron z-vertex cut	Varied by $\pm 0.2$ cm on each side
1	electron sampling fraction cut	shown in figure 7.10
2	electron EC $E_{dep}$ cut	$\pm 5$ MeV
3	electron EC U, V, W cut	shown in figure 7.13
4	electron $\theta_{CC}$ matching cut	Varied by $\pm 0.2$ cm on each side
5	electron region 1 fid. cut	shown in figure 7.8
6	electron region 3 fid. cut	shown in figure 7.9
7	electron CC fid. cut	shown in figure 7.12
8	pion $\beta$ cut	$\pm 0.25 \sigma$
9	pion region 1 fid. cut	-
10	$\phi_h$ fid. cut	$\pm 10^\circ$ on each side
11	acceptance model	second to last iteration used
12	radiative correction model	second to last iteration used

$$\Delta^{(i)} = \sqrt{\frac{1}{N_{vars}} \sum_{j=1}^{N_{vars}} (r^{(0)} - r^{(j)})^2}$$

(7.12)

Here  $N_{vars}$  is the number of variations performed for source  $i$ , and  $r^{(0)}$  is the measured result with the nominal set of parameters and  $j$  is a an index for the sum over variations of this parameter. For the acceptance and radiative corrections model dependence instead of increasing and decreasing a value the model is changed and these are treated as variations.

## 7.9 Results

Section that makes general remarks about the extracted results and shows figures that summarize the results.

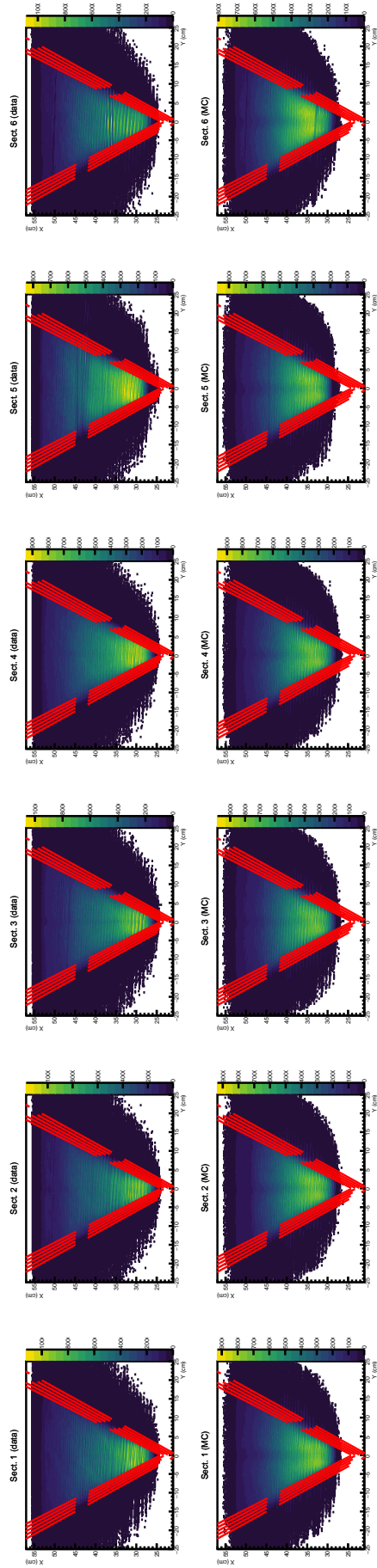


Figure 7.8: Boundaries for electron identification cuts placed on the region 1 drift chambers are shown for data (top row) and Monte Carlo (bottom row).

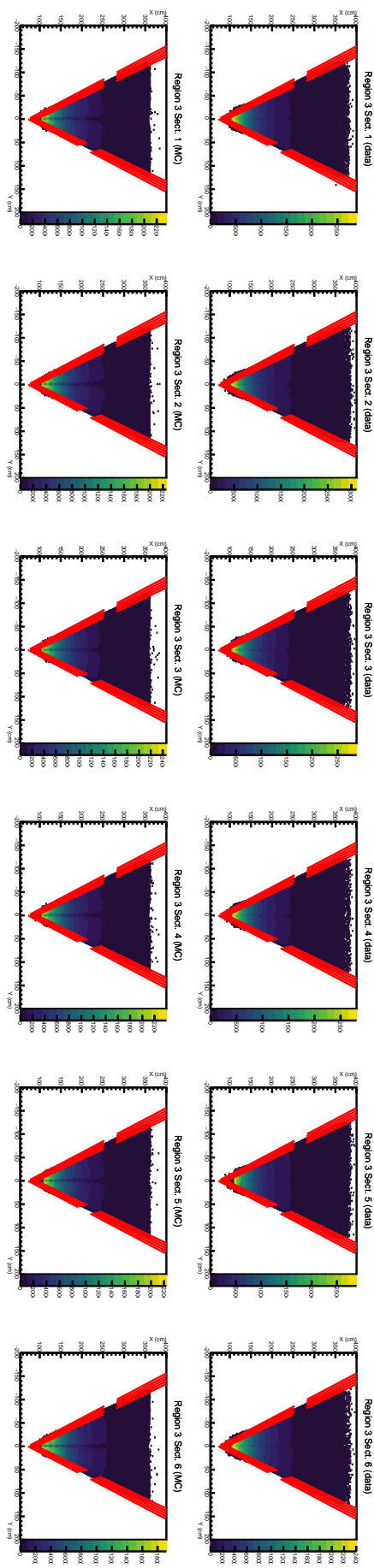


Figure 7.9: Boundaries for electron identification cuts placed on the region 3 drift chambers are shown for data (top row) and Monte Carlo (bottom row).

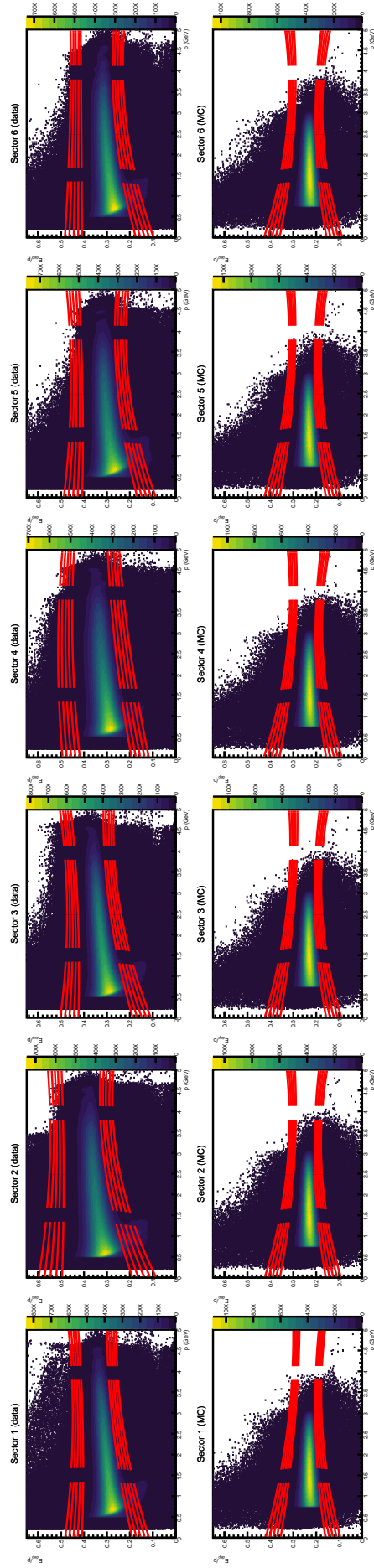


Figure 7.10: The sampling fraction boundaries used to identify electrons in data (top) and Monte Carlo (bottom) are shown over the distributions.

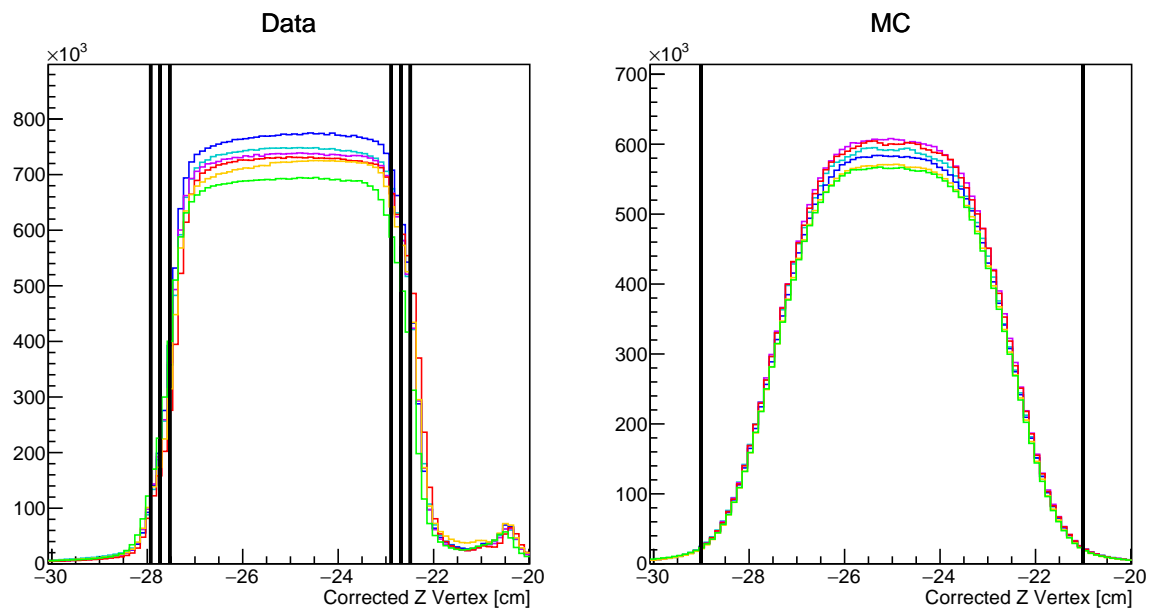


Figure 7.11: The cut boundaries for z-vertex used to identify electrons in data (left) and Monte Carlo (right). This histograms shown for data have been corrected before being filled.

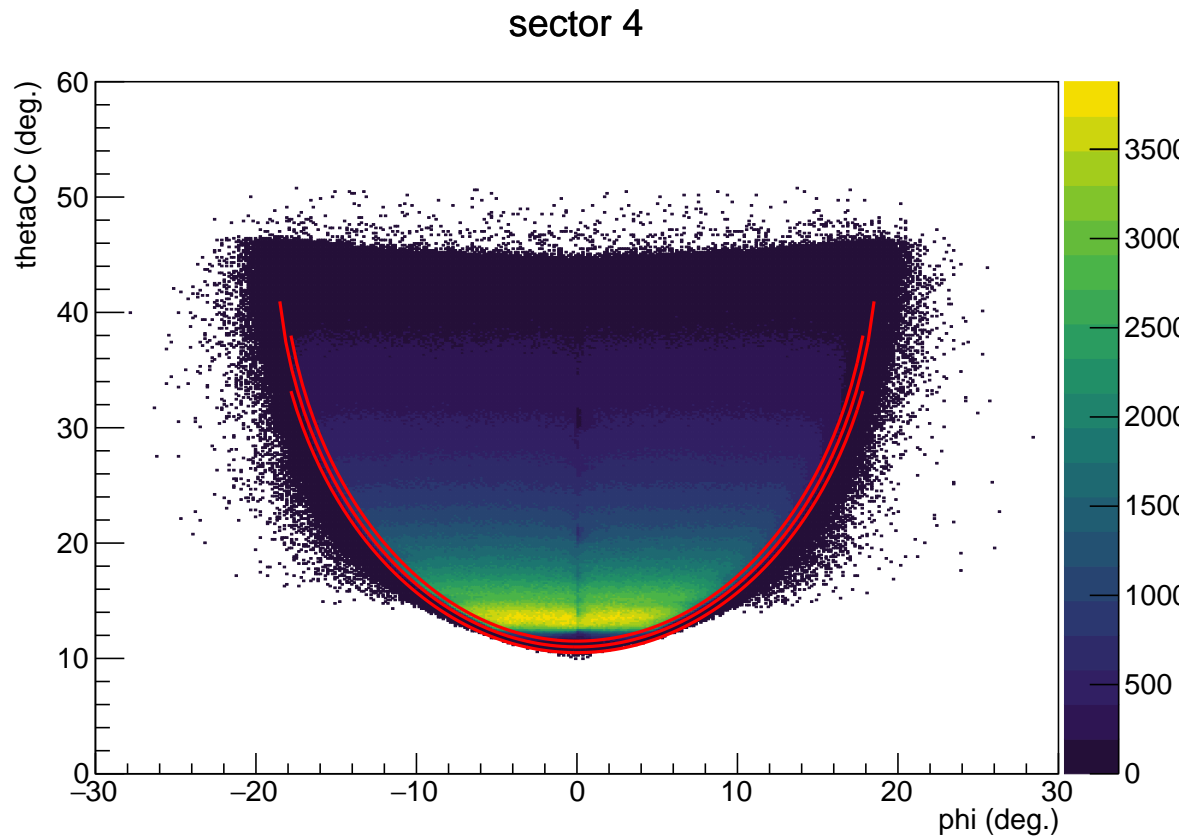


Figure 7.12: The loose, nominal, and tight boundaries applied to data for the fiducial cuts on the Cherenkov Counter.

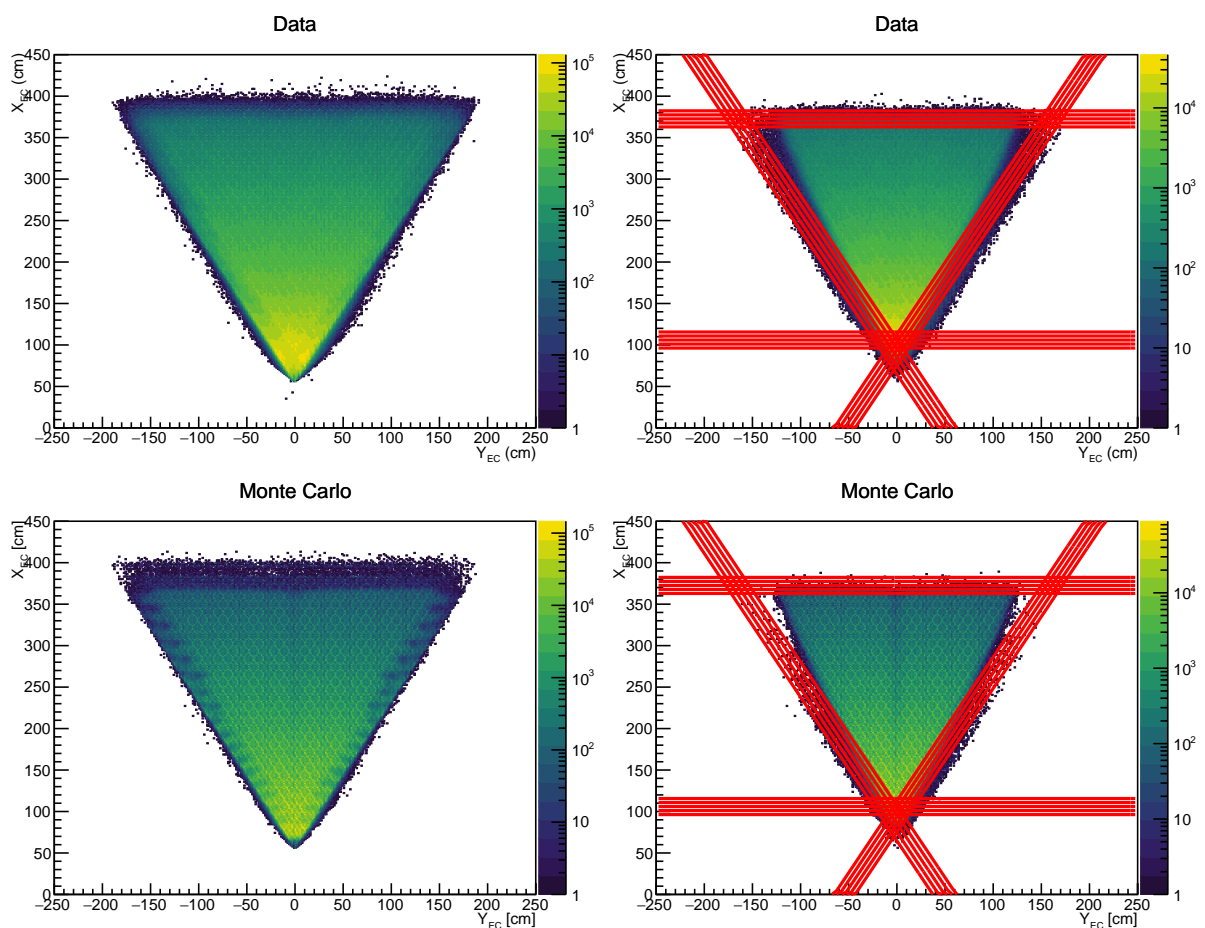


Figure 7.13: Electron identification cuts on U, V, and W coordinates are shown in x-y space.

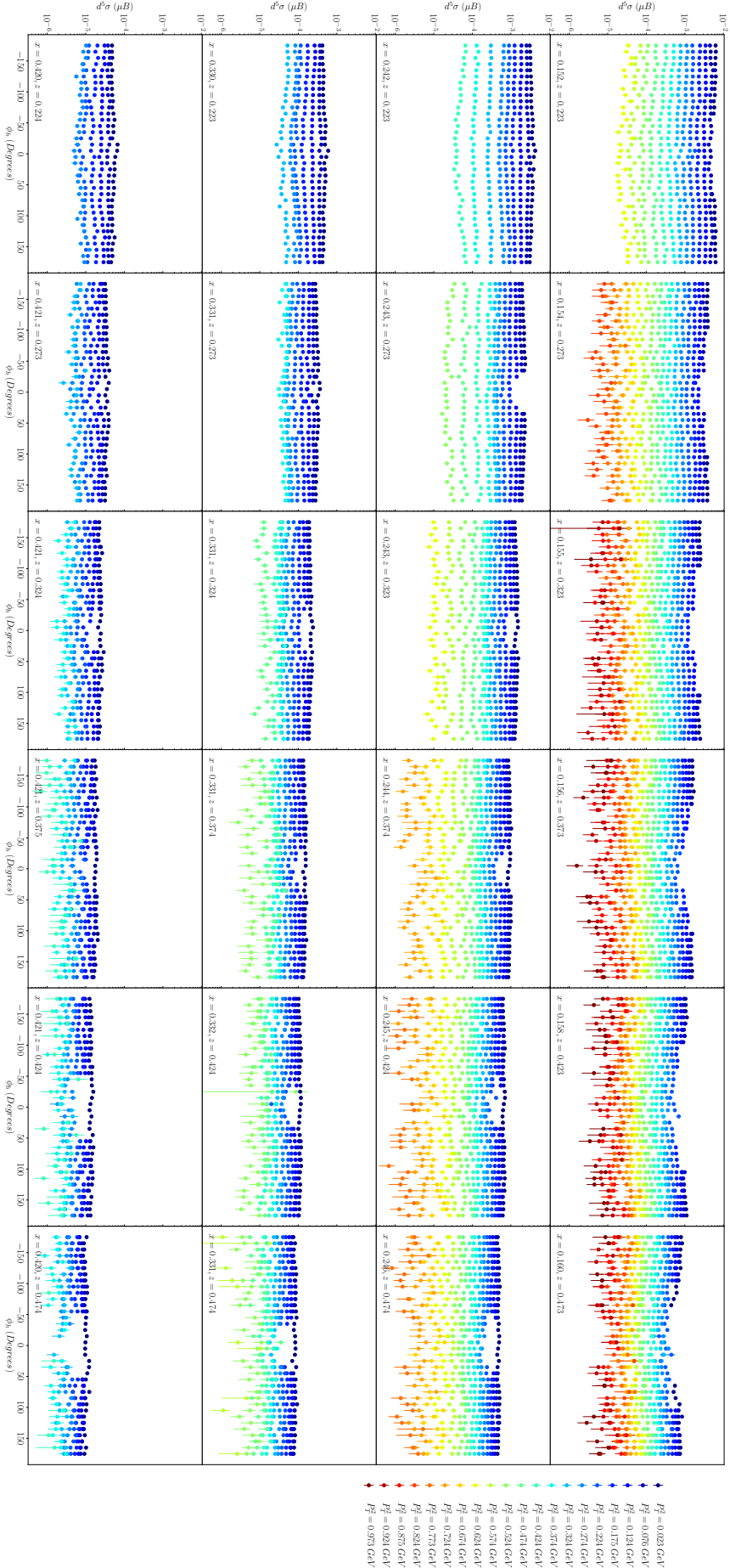


Figure 7.14: The 5-differential cross section for  $\pi^+$  shown for different values of  $x$  and  $z$  in different panels of the figure. In each panel, the  $P_T^2$  dependence of the cross section is shown by superimposing different bins in different colors. The legend at the right of the figure contains information about the colors and their corresponding  $P_T^2$  value.

## Appendix A: Derivation of formulas related to errors

### Propagation of errors

Let  $\vec{x}$  be a set of  $n$  random variables  $\vec{x} = (x_1, x_2, \dots, x_n)$  and known mean  $\mu_i = \langle x_i \rangle$  and covariance  $V_{ij} = \langle x_i x_j \rangle - \langle x_i \rangle \langle x_j \rangle$ . Suppose that we measure a function  $f(\vec{x})$  that depends on the variables  $\vec{x}$  and we want to understand how the covariances  $V_{ij}$  on  $\vec{x}$  will show up manifest themselves as errors on our measurement of  $f(\vec{x})$ . We can start by expanding our function around the expected value of  $x_i$ .

$$f(\vec{x}) \approx f(\vec{\mu}) + \sum_{i=1}^n \frac{\partial f}{\partial x_i} \Big|_{x_i=\mu_i} (x_i - \mu_i) \quad (13)$$

We can then take the expectation value of our function.

$$\langle f(\vec{x}) \rangle = \langle f(\vec{\mu}) \rangle + \sum_{i=1}^n \frac{\partial f}{\partial x_i} \Big|_{x_i=\mu_i} \langle x_i - \mu_i \rangle \quad (14)$$

Where here the term  $\langle x_i - \mu_i \rangle$  is zero.

$$\langle x_i - \mu_i \rangle = \langle x_i \rangle - \mu_i = \mu_i - \mu_i = 0 \quad (15)$$

It is apparent then that the expectation value of our function  $f$  evaluated close to the expected values of our variables  $\vec{x}$  is just the function evaluated at the expectation value of the random variables  $\vec{x}$ .

$$\langle f(\vec{x}) \rangle = \langle f(\mu) \rangle = f(\mu) \quad (16)$$

We can also consider the second moment  $\langle f^2(\vec{x}) \rangle$ ,

$$\langle f^2(\vec{x}) \rangle \approx \left\langle \left( f(\vec{\mu}) + \sum_{i=1}^n \frac{\partial f}{\partial x_i} \Big|_{x_i=\mu_i} (x_i - \mu_i) \right)^2 \right\rangle \quad (17)$$

which is,

$$= \langle f^2(\mu) \rangle + \sum_{i=1}^n \sum_{j=1}^n \frac{\partial f}{\partial x_i} \Big|_{x_i=\mu_i} \frac{\partial f}{\partial x_j} \Big|_{x_j=\mu_j} \langle (x_i - \mu_i)(x_j - \mu_j) \rangle + 2 \left\langle f(\mu) \sum_{i=1}^n \frac{\partial f}{\partial x_i} \Big|_{x_i=\mu_i} (x_i - \mu_i) \right\rangle \quad (18)$$

and the last expectation value vanishes due to the same logic used when calculating the first moment. We recognize the term  $\langle (x_i - \mu_i)(x_j - \mu_j) \rangle$  as the element of the covariance matrix  $V_{ij}$ . Our second moment is then complete as follows.

$$\langle f^2(\vec{x}) \rangle = f^2(\mu) + \sum_{i=1}^n \sum_{j=1}^n \frac{\partial f}{\partial x_i} \Big|_{x_i=\mu_i} \frac{\partial f}{\partial x_j} \Big|_{x_j=\mu_i} V_{ij} \quad (19)$$

We can then calculate the variance of the function.

$$\sigma_f^2 = \langle f^2(\vec{x}) \rangle - \langle f(\vec{x}) \rangle^2 \quad (20)$$

$$= (f^2(\vec{\mu}) - f^2(\vec{\mu})) + \sum_{i=1}^n \sum_{j=1}^n \frac{\partial f}{\partial x_i} \Big|_{x_i=\mu_i} \frac{\partial f}{\partial x_j} \Big|_{x_j=\mu_i} V_{ij} \quad (21)$$

$$= \sum_{i=1}^n \sum_{j=1}^n \frac{\partial f}{\partial x_i} \Big|_{x_i=\mu_i} \frac{\partial f}{\partial x_j} \Big|_{x_j=\mu_i} V_{ij} \quad (22)$$

This is the standard error propagation formula which is widely used. These correlations  $\sigma_{ij}$  can arise from several sources.

- Common measurement uncertainties.
- Correlations in  $x_i x_j$  leading to correlations in  $\sigma_i \sigma_j$ .

# References

- [] A. Bacchetta, M. Diehl, K. Goeke, A. Metz, P. J. Mulders, and M. Schlegel, JHEP **02**, 093 (2007), arXiv:hep-ph/0611265 [hep-ph].
- [] C. W. Leemann *et al.*, Ann. Rev. Nucl. Part. Sci. **51**, 413 (2001).
- [] Y. C. Chao *et al.*, J. Phys. Conf. Ser. **299**, 012015 (2011).
- [] G. Adams *et al.*, Nucl. Instrum. Meth. **A465**, 414 (2001).
- [] M. D. Mestayer *et al.*, Nucl. Instrum. Meth. **A449**, 81 (2000).
- [] E. S. Smith *et al.*, Nucl. Instrum. Meth. **A432**, 265 (1999).
- [] M. Amarian *et al.*, Nucl. Instrum. Meth. **A460**, 239 (2001).
- [] N. A. Harrison, *Exploring the Structure of the Proton via Semi-Inclusive Pion Electroproduction*, Ph.D. thesis, Connecticut U. (2010).
- [] M. Mirazita, “Kinematic corrections for e1-f,” .
- [] R.-G. Ping *et al.*, Int. J. Mod. Phys. **A24S1**, 23 (2009).
- [] R. Barlow, in *Advanced Statistical Techniques in Particle Physics. Proceedings, Conference, Durham, UK, March 18-22, 2002* (2002) pp. 134–144, arXiv:hep-ex/0207026 [hep-ex] .
- [] G. Watt and R. S. Thorne, JHEP **08**, 052 (2012), arXiv:1205.4024 [hep-ph] .
- [] W. Gohn *et al.* (CLAS), Phys. Rev. **D89**, 072011 (2014), arXiv:1402.4097 [hep-ex] .
- [] C. Keppel, *Inclusive nucleon resonance electroproduction at large momentum transfer*, Ph.D. thesis, American U. (1994).
- [] L. W. Mo and Y.-S. Tsai, Rev. Mod. Phys. **41**, 205 (1969).